Unraveling Ocular Tissue Biomechanics: Characterizing Collagen Microstructural Features And Introducing Direct Fiber Modeling

by

Fengting Ji

Bachelor of Science in Aeronautical Engineering, Northwestern Polytechnical University, 2016

Master of Science in Mechanical Engineering, Columbia University, 2018

Submitted to the Graduate Faculty of the

Swanson School of Engineering in partial fulfillment

of the requirements for the degree of

Doctor of Philosophy

University of Pittsburgh

2023

UNIVERSITY OF PITTSBURGH

SWANSON SCHOOL OF ENGINEERING

This dissertation was presented

by

Fengting Ji

It was defended on

August 24, 2023

and approved by

Steven D. Abramowitch, PhD, Professor, Department of Bioengineering

Morgan V. DiLeo, PhD, Assistant Professor, Department of Ophthalmology, Bioengineering and Clinical & Translational Sciences

Kira L. Lathrop, Assistant Professor, Department of Ophthalmology

Anne M. Robertson, PhD, Professor, Department of Mechanical Engineering and Materials Science

Dissertation Director: Ian A. Sigal, PhD, Associate Professor, Department of Ophthalmology and Bioengineering

Unraveling Ocular Tissue Biomechanics: Characterizing Collagen Microstructural Features And Introducing Direct Fiber Modeling

Fengting Ji, PhD

University of Pittsburgh, 2023

Glaucoma, a progressive optic neuropathy, is primarily associated with elevated intraocular pressure (IOP) and mechanical insult on ocular tissues. The optic nerve head (ONH) and lamina cribrosa (LC) are particularly vulnerable to early nerve damage, while the sclera surrounding the ONH, provides essential mechanical support and stability. Understanding the biomechanics of these ocular structures is crucial for unraveling the mechanisms of glaucoma.

The biomechanics of ONH, LC and sclera are intricately connected to their collagen microstructure, necessitating a comprehensive understanding of tissue microstructures and their associated biomechanical properties. However, despite extensive work, several microstructural characteristics have not been considered carefully, largely due to limitations in visualization tools. Furthermore, current modeling approaches in ocular biomechanics often neglect potentially critical fiber characteristics, limiting their ability to describe tissue structure and mechanics, particularly at fiber-level scales.

Using advanced imaging techniques like polarized light microscopy, this dissertation characterizes two critical microstructural features that have been ignored: LC insertions and the in-depth collagen fiber organization of corneoscleral shell. We characterized the spatial variations of LC insertions and variations of insertions among species. The discrete insertions of the LC beam indicate that the interaction between LC and the surrounding load-bearing tissue is discontinuous, leading to localized force concentrations. Diverse insertion shapes suggest varying robustness in

the LC periphery, potentially influencing susceptibility to glaucomatous damage. We also present a detailed analysis of the in-depth organization of collagen fibers within the corneoscleral shell for a better characterization of the complex three-dimensional collagen architecture. This, in turn, will enhance the understanding of the out-of-plane tissue mechanical properties.

Leveraging detailed information available from the imaging, this project proposes and validates a novel direct fiber modeling approach that represents fibrous microstructure, accounting for fiber interweaving, interactions, and specimen-specific collagen architecture. The proposed model replicates anisotropic mechanical behavior observed in different loading protocols and across different samples, providing unprecedented details on fiber-level tissue behavior.

In conclusion, this dissertation uncovers crucial microstructural features of ocular tissue and introduces an innovative direct fiber modeling technique. The findings contribute to a deeper understanding of ocular tissue microstructure and biomechanics, advancing our knowledge of glaucoma pathogenesis.

Table of Contents

List of Tables

List of Figures

Preface

Acknowledgement

I am profoundly grateful to Dr. Ian Sigal for his exceptional guidance and mentorship throughout my tenure in the Ocular Biomechanics Laboratory. His invaluable support and insightful supervision have left an indelible mark on my academic and professional journey. I extend my heartfelt appreciation for his unwavering patience and dedication as my PhD advisor.

I would like to express my sincere gratitude to the members of my dissertation committee, Dr. Steven Abramowitch, Dr. Morgan DiLeo, Professor Kira Lathrop, and Dr. Anne Robertson, for their invaluable contributions to this dissertation.

I am also indebted to the current and former members of the Ocular Biomechanics Laboratory who have generously assisted me in data collection and analysis during their tenure in our lab. I want to extend special recognition to Manik Bansal, Mohammad Islam, Po-Yi Lee, Po Lam, Marissa Quinn, Hannah Schilpp, Yi Hua, and Bingrui Wang. Your willingness to collaborate and lend support, even with the most intricate tasks, has been truly appreciated. I am also grateful for the assistance provided by our collaborators outside the University of Pittsburgh, particularly Frederick Sebastian and Felix Matuschke.

Lastly, I would like to express my deepest appreciation to my family and friends. To my husband, your encouragement and timely words have been my guiding light throughout this journey, keeping me focused on completing my PhD. I have always believed that finding a true confidant in life is a rare blessing. Being able to meet you during this journey, forming a family with you, and now welcoming our daughter, I consider it an incredible stroke of luck. To my parents and in-laws, thank you for your steadfast support, especially during the challenges posed

by the COVID-19 pandemic. To all the friends I have made along the way, I eagerly look forward to nurturing our friendships as I embark on new endeavors.

Abbreviations

Adjusted R^2 - Adjusted R squared

CV - Coefficient of variation

HWHM - Half width at half maximum

IOP - Intraocular pressure

IPOL - Instant polarized light microscopy

LC - lamina cribrosa

LME - linear mixed effect

ONH - Optic nerve head

PLM - Polarized light microscopy

PPS - Peripapillary sclera

RSS - Residual sum of squared

SD - Standard deviation

VF - Volume fraction

1.0 Introduction

1.1 Glaucoma And Ocular Biomechanics

Glaucoma, a complex and progressive optic neuropathy, is one of the leading causes of irreversible blindness worldwide (Quigley and Broman 2006, Weinreb, Aung et al. 2014). It is characterized by the degeneration of retinal ganglion cells (RGCs) and their axons, leading to vision impairment and irreversible vision loss (Jonas and Budde 2000, Weinreb, Aung et al. 2014). Elevated intraocular pressure (IOP) has long been recognized as a primary risk factor in the development and progression of glaucoma, exerting mechanical insult on ocular tissues (Flammer, Orgül et al. 2002, Girard, Suh et al. 2011). As such, understanding the interplay between ocular biomechanics and glaucomatous optic neuropathy is crucial for unraveling the underlying mechanisms and developing effective diagnostic and therapeutic strategies (Sigal and Ethier 2009).

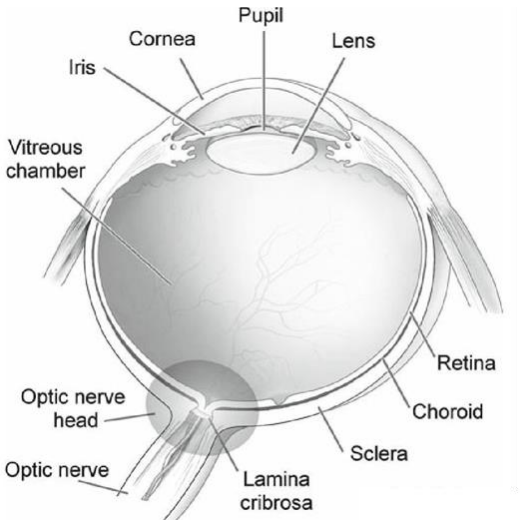

Figure 1. Schematic cross-section of the human eye illustrating key structures.The figure is adapted from nei.nih.gov. Light enters through the cornea, passes through the pupil, lens, and vitreous humor to reach the

retina (neural tissue lining the back of the eye). The ONH region, comprising the LC, is highlighted. The LC is a porous structure within the ONH, through which retinal nerve fibers converge and exit the eye via the scleral canal within the corneoscleral shell (outer protective layer).

The optic nerve head (ONH) and lamina cribrosa (LC) (Figure 1) take center stage in glaucoma research due to their intimate association with the disease's onset and progression (Roberts, Liang et al. 2010, Oikawa, Ver Hoeve et al. 2020). The LC, located within the ONH, forms a three-dimensional network of load-bearing trabeculae supporting RGC axons as they exit the eye to the brain (Downs and Girkin 2017, Liu, McNally et al. 2018). Biomechanically, the ONH, and especially the LC within, are thought of as a weak spot within the otherwise robust corneoscleral envelope (Sigal and Ethier 2009, Voorhees, Jan et al. 2018), rendering them highly susceptible to mechanical strain induced by elevated IOP (Strouthidis and Girard 2013, Tan, Koh et al. 2018). Understanding the biomechanics of the LC and ONH provides insights into the delicate balance between structural support and axonal passage, significantly contributing to our comprehension of glaucoma development and progression (Stowell, Burgoyne et al. 2017, Tamm and Ethier 2017).

The ONH is not an isolated entity but is connected to the surrounding sclera, a crucial component of the corneoscleral shell. As the primary load-bearing tissue of the eye, the sclera provides essential mechanical support and resistance to deformation (Grytz, Fazio et al. 2014, Boote, Sigal et al. 2020). Recent investigations highlight the significant involvement of scleral biomechanical properties in glaucoma, with changes in stiffness, thickness, and remodeling linked to elevated IOP and optic nerve damage (Norman, Flanagan et al. 2011, Coudrillier, Pijanka et al. 2015, Boote, Sigal et al. 2020). Additionally, the biomechanical interplay between the sclera and the ONH is critical, as mechanical strains experienced by the sclera can directly impact the LC and

the vulnerability of RGCs (Sigal, Flanagan et al. 2005, Girard, Downs et al. 2009, Sigal and Ethier 2009). Therefore, studying the biomechanics of the sclera and the corneoscleral shell holds great promise in deepening our understanding of glaucoma pathophysiology.

1.2 Ocular Tissue Collagen Microstructure

The collagen microstructure of ONH, LC, and corneoscleral shell holds significant importance in glaucoma research. Collagen fibers serve as the primary determinants of the mechanical properties and load-bearing capacity of these ocular structures (Coudrillier, Pijanka et al. 2015, Jan and Sigal 2018). Understanding factors such as the arrangement and organization of collagen within the ONH, LC, and corneoscleral shell provides crucial insights into how they respond to mechanical stresses, particularly elevated IOP (Campbell, Coudrillier et al. 2014, Zhang, Albon et al. 2015). While recent studies have made substantial progress in investigating ocular tissue collagen microstructural features (Girard, Dahlmann-Noor et al. 2011, Gogola, Jan et al. 2018), critical microstructural details have remained overlooked, partly due to limitations in available imaging techniques.

Leveraging the advancements in polarized light microscopy (PLM) (Jan, Grimm et al. 2015, Lee, Yang et al. 2022), a novel imaging technique, we can now explore previously unobservable microstructural features. PLM provides higher spatial resolution and faster imaging time compared to conventional light scattering-based imaging techniques that are commonly applied to ocular tissues like small-angle light scattering (SALS) (Girard, Dahlmann-Noor et al. 2011, Yan, McPheeters et al. 2011), small-angle x-ray scattering (Boote, Dennis et al. 2003, Girard, Dahlmann-Noor et al. 2011), and wide-angle x-ray scattering (WAXS) (Pijanka,

Coudrillier et al. 2012, Pijanka, Abass et al. 2013). In addition, PLM is faster and simpler to integrate with microscopy systems than scanning techniques, such as confocal microscopy (Masters 1998, Kang and Yu 2015) and second-harmonic generated (SHG) imaging (Girard, Dahlmann-Noor et al. 2011, Mikula, Winkler et al. 2018). By capitalizing on the benefits of PLM, we have identified two microstructural features that are not yet characterized, LC insertions and in-depth collagen organization in the corneoscleral shell.

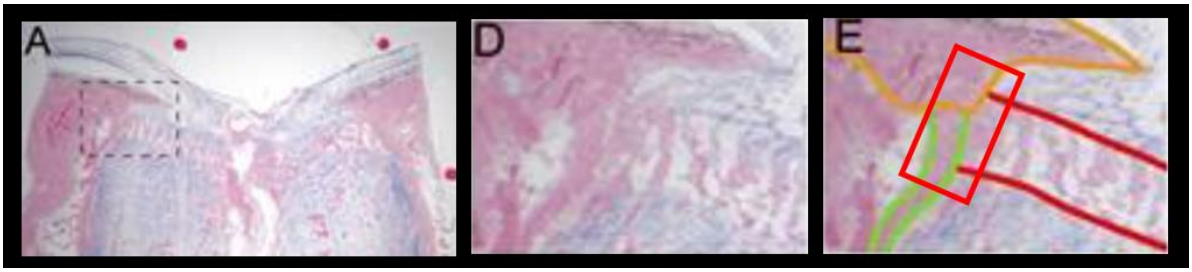

Figure 2. Simplified LC (red lines) inserting into the sclera (yellow lines) and the pia mater (green lines).The images are bright field images of human ONH sections stained with picrisirius red and solochrome cyanine to label collagen in pink and neural tissues in blue, respectively, adapted from Sigal et al., 2012. Panels D and E are close-ups of the region marked with a dashed rectangle in Panel A. The region of the LC insertion into the sclera and pia is marked with the red box in Panel E.

The LC's ability to support neural tissue is contingent upon its connection to the much stronger peripapillary sclera (Burgoyne, Downs et al. 2005, Sigal 2009, Sigal and Ethier 2009, Jonas, Jonas et al. 2011), making the LC insertions a critical site for understanding glaucoma biomechanics. Previous studies have often oversimplified this interface, considering it as a smooth continuum surface (Figure 2) (Sigal, Flanagan et al. 2010, Yang, Williams et al. 2010, Wang, Rumpel et al. 2016). However, a closer examination reveals that LC beam insertions display complex and variable features, including curved or straight shapes, broad or narrow widths, and shallow or deep penetration depths (Ji, Yang et al. 2020) (Figure 3). These variations suggest that

the mechanical demands at the LC-sclera interface, or the ability of the LC to bear them, may vary across different regions. Understanding the microstructural features of LC insertions and their impact on the biomechanical environment is crucial for comprehending the vulnerability of RGC axons to mechanical stress and strain. Although the patterns of neural tissue damage and their progression are complex and vary between patients and species, it is often considered that some of the earliest tissue damage in glaucoma occurs at the LC periphery, very much in the pores between the LC insertions (Quigley 2005, Stowell, Burgoyne et al. 2017).

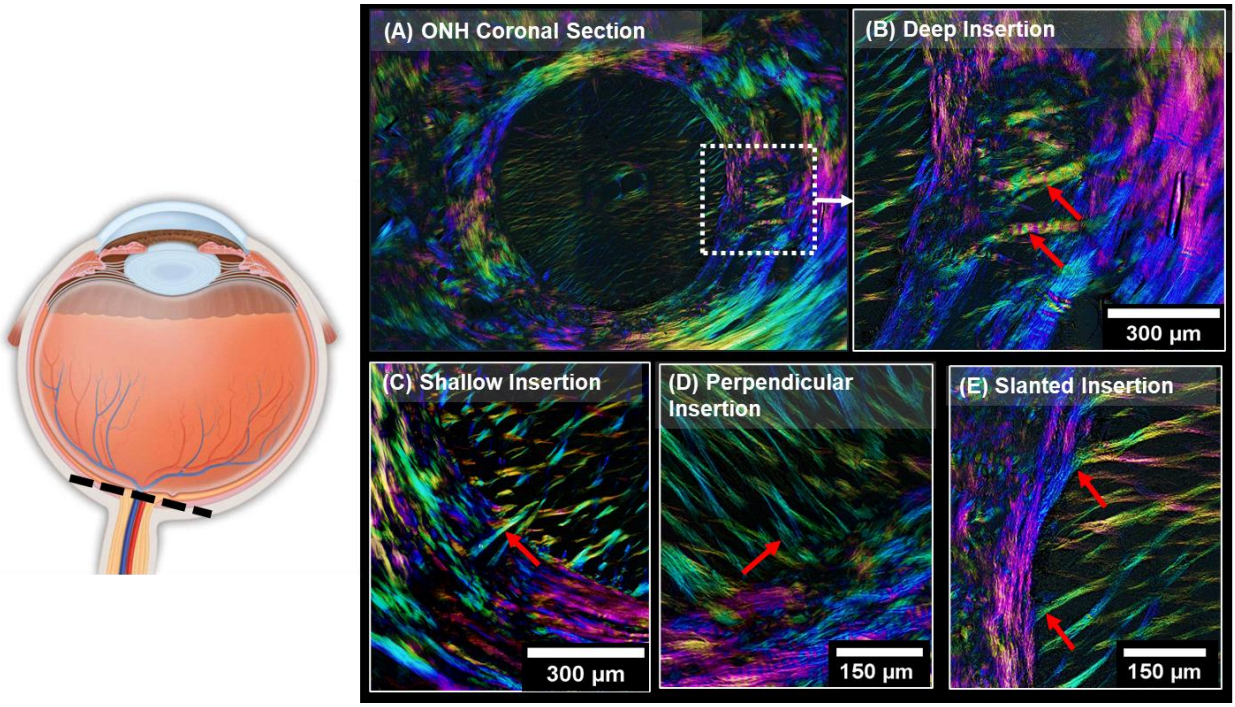

Figure 3. Variations in LC insertions.(A-E) Example PLM image of LC insertions in human ONH coronal cryosections at the location indicated by the black dashed line on the left eye diagram. LC insertions with varying depth are observed in (A, B, C). Specifically, very deep insertions are observed in (B). (D) exhibits narrow, straight perpendicular insertions that penetrate past the circumferential ring. (E) shows insertions with curved fibers that seem to integrate into the circumferential ring. PLM images were obtained using the technique variation known as IPOL, as described in (Yang, Lee et al. 2021).

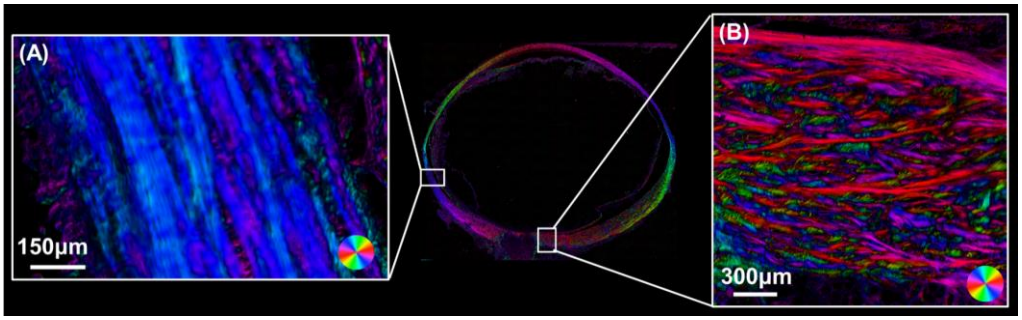

Figure 4. Example PLM image showing the collagen microstructure of a sheep eye.The colors indicate the in-plane collagen fiber orientation in each pixel, ranging from 0 to 180 degrees. Additionally, the image pixel intensity corresponds, roughly, to collagen density for the in-plane collagen. (A) A close up look of a sclera region near the equator, where fibers exhibit a more uniform alignment parallel to the sclera surface. (B) Region near the sclera canal, showing fibers with a more complex alignment in many directions.

Similarly, the microstructural architecture of the corneoscleral shell's collagen fibers has garnered increasing interest. Previous studies have revealed an anisotropic, interwoven, and inhomogeneous structure of these fibers (Figure 4) (Boote, Hayes et al. 2006, Girard, Dahlmann-Noor et al. 2011, Pijanka, Coudrillier et al. 2012, Coudrillier, Boote et al. 2013, Abass, Hayes et al. 2015, Jan, Lathrop et al. 2017, Yang, Jan et al. 2018). However, the focus has predominantly been on characterizing the collagen fiber architecture in-plane of the tissue. Sometimes this has been extended to analyze the depth-dependence of the in-plane fiber orientations (Pijanka, Spang et al. 2015, Jan, Lathrop et al. 2017, Gogola, Jan et al. 2018). Variations in orientation distributions and anisotropies may imply varying out-of-plane tissue mechanical properties around the eye globe. The studies, however, have not actually characterized the in-depth orientation of the fibers. The in-depth fiber features of the sclera likely also contributes to tissue stiffness and stability, as it has been shown for the cornea (Morishige, Wahlert et al. 2007, Winkler, Chai et al. 2011, Petsche and Pinsky 2013). Understanding the 3D distribution and arrangement of collagen fibers within the corneoscleral shell, especially the in-depth collagen fiber organization, is vital for developing

more accurate fiber-based microstructure models of the eye and comprehending the role of collagen microstructure in eye biomechanics.

In Chapter 2, 3 and 4, we aim to address the gaps in knowledge regarding the microstructural features of LC insertions and the in-depth collagen fiber organization within the corneoscleral shell. By characterizing these overlooked collagen microstructural details, we strive to advance our understanding of the intricate 3D collagen architecture in ocular tissues. This endeavor will significantly contribute to our comprehension of how mechanical forces are distributed and transmitted within the eye, thereby elevating our knowledge of ocular biomechanics and its implications in various ocular conditions, particularly glaucoma.

1.3 The Need For Developing Direct Fiber Modeling Technique

The investigation of ocular tissue collagen microstructure plays a vital role in comprehending their biomechanical behaviors. However, the complexity of the tissue collagen microstructure and the limitations of available experimental techniques present significant challenges for studying the microstructural features and relating them to the micro and macroscopic behavior of the tissue through empirical methods alone. Consequently, there is a growing reliance on numerical modeling techniques for analysis (Sigal, Flanagan et al. 2004, Girard, Downs et al. 2009, Girard, Downs et al. 2009, Grytz, Meschke et al. 2011, Grytz, Girkin et al. 2012, Coudrillier, Boote et al. 2013, Coudrillier, Pijanka et al. 2015, Voorhees, Jan et al. 2017, Voorhees, Jan et al. 2018, Grytz, Krishnan et al. 2020, Hua, Voorhees et al. 2020).

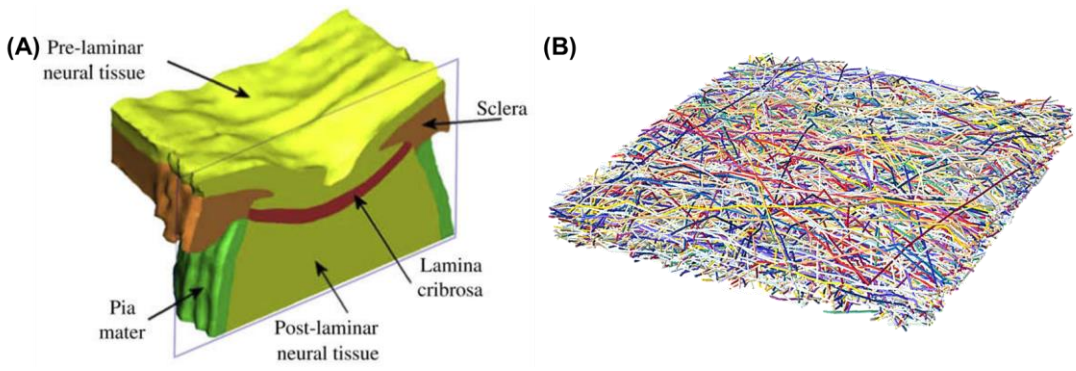

Figure 5. Continnum model and direct fiber model.(A) Continuum model of human LC, adapted from Sigal et al., 2009. (B) Direct fiber model of sclera, utilizing explicit, individual collagen fibers for simulation. Modeled fibers were assigned random colors to simplify visualization.

Nevertheless, accurately representing the intricate 3D nature of the collagen microstructural features proves difficult using conventional modeling approaches. Conventional techniques often adopt continuum mechanics frameworks (Figure 5 A) and statistical approximations to describe tissue collagen microstructural properties. While these methods provide insights into the tissue mechanical behaviors, it remains a major challenge to accurately capture critical features of collagen fibers (i.e., long fibers, fiber interweaving, fiber-fiber interactions) (Jan, Lathrop et al. 2017, Boote, Sigal et al. 2020, Lee, Yang et al. 2022). This limitation can introduce substantial errors when estimating fiber mechanical properties using inverse fitting (Wang, Hua et al. 2020). Therefore, the development of a direct fiber modeling approach becomes imperative for understanding how collagen microstructural features contribute to the mechanical responses.

In Chapter 5 and 6, we describe the development of a direct fiber modeling technique to enable a more accurate representation of the 3D collagen microstructure while still being able to capturing the tissue macroscale mechanical behaviors. The direct fiber modeling approach allows us to explicitly simulate individual collagen fibers, capturing their spatial arrangement, orientation,

and fiber interactions within the tissue (Figure 5 B). By employing this new technique, we can gain unique insights into fiber architecture and mechanics, and address questions that are beyond the reach of conventional modeling methods. This technique is not intended to supersede conventional methods, which have been extraordinarily successful in modeling the mechanics of eyes and other organs (Baillargeon, Rebelo et al. 2014, Pellicer-Valero, Rupérez et al. 2020). Direct fiber modeling is intended to work alongside conventional continuum modeling in cases where the specific interest involves soft fibrous tissues and questions about behavior at the fiber level, for example.

1.4 Specific Aims

The long-term goal of this project is to investigate the collagen microstructure and biomechanics of ocular tissues that could contribute to the understanding of glaucoma development. Specifically, our aims are to characterize the microstructures of LC insertions and the in-depth collagen organization within the corneoscleral shell. To achieve a comprehensive understanding of collagen microstructural biomechanics, the development of a direct fiber modeling approach is essential, enabling us to simulate specimen-specific collagen architecture and macroscale mechanical behaviors. This modeling technique can account for critical fiber characteristics, including long fibers, fiber interweaving, and interactions. The project is organized into three specific aims:

1.4.1 Specific Aim 1

Characterize variations of LC insertions.

1a. Characterize the variations in insertion widths and insertion angles among four different species (sheep, pig, monkey, and human).

1b. Characterize the spatial distribution of LC insertions from the anterior to posterior LC and across the four quadrants of monkey eyes. Quantify variations in insertion width, insertion angle, number of insertions, and insertion ratio.

1.4.2 Specific Aim 2

Characterize in-depth collagen organization in the corneoscleral shell.

2a. Quantify in-depth fiber orientation distributions and anisotropy around the corneoscleral shell. Test if the orientation distributions could be accurately summarized with a combination of a uniform distribution and a sum of π-periodic von Mises distributions.

2b. Quantify fiber inclination in the corneoscleral shell, characterized by the percentage of fibers that are inclined-not parallel to sclera surface, and the range of inclination angles (half width at half maximum of inclination angle distribution).

1.4.3 Specific Aim 3

Develop and validate the direct fiber modeling technique for posterior sclera.

3a. Develop the methodology of direct fiber modeling capable of simulating the specimen-specific 3D collagen fiber architecture of sclera. Utilize an inverse fitting approach to estimate the model's fiber mechanical properties.

3b. Validate the direct fiber modeling approach by simulating collagen microstructures of multiple sclera samples. Determine, by inverse fitting, the fiber material properties that allow the models to accurately replicate the anisotropic mechanical behaviors observed in multiple biaxial loading schemes.

1.4.4 Dissertation Outline

The dissertation has been organized into 6 chapters:

Chapter 1: Introduction.

This chapter provides an overview of the significance of studying collagen microstructure in ocular tissues and its crucial role in glaucoma pathogenesis. It also emphasizes the need for developing the direct fiber modeling approach to understand the biomechanics of ocular tissue collagen microstructure.

Chapter 2: Characterization of LC insertions variations between sheep, pig, monkey and human.

This chapter explores the variations in LC insertions among different species, including sheep, pig, monkey, and humans. Specifically, it addresses Specific Aim 1a.

Chapter 3: Characterization of spatial variations of monkey LC insertions.

Focusing on Specific Aim 1b, this chapter characterizes spatial variations in monkey LC insertions, considering both posterior to anterior LC variations and variations among the four quadrants.

Chapter 4: Characterization of in-depth collagen fiber organization across the corneoscleral shell.

In this chapter, we quantitatively analyze the in-depth fiber orientation distributions and fiber inclination across the corneoscleral shell. This investigation pertains to Specific Aim 2a and 2b.

Chapter 5: Introduction of direct fiber modeling approach for simulating sclera collagen architecture and biomechanics.

This chapter introduces the novel approach of direct fiber modeling, designed to capture closely the collagen architecture and biomechanics of the sclera. Using microscopy images, we constructed a direct fiber model of a sample of posterior pole sclera. To validate the model's fiber mechanical properties, we fitted data from an equi-biaxial experiment sourced from the literature. This chapter addresses Specific Aim 3a.

Chapter 6: Validation of the direct fiber modeling approach to simulate sclera collagen fiber architecture and anisotropic mechanical behaviors.

Specific Aim 3b is the focal point of this chapter, where we extensively validate the effectiveness and accuracy of the direct fiber modeling approach. By simulating the sclera collagen fiber architecture and analyzing its anisotropic mechanical behaviors, we demonstrate the robustness of the model. The validation process goes beyond the single sample and experiment of Chapter 5, and involves the creation of several specimen-specific models based on multiple sclera samples. Importantly, we establish the reliability of each model by identifying its mechanical properties from experimental data obtained from the same sample in multiple tests.

2.0 Characterization Of LC Insertions Variations Between Sheep, Pig, Monkey And Human

The content of this section was adapted from abstracts presented at the 2020 Association for Research in Vision and Ophthalmology (ARVO) annual meeting and the 2023 Summer Biomechanics, Bioengineering, and Biotransport Conference (SB3C) annual meeting.

2.1 Introduction

The lamina cribrosa (LC) is a specialized structure in the posterior pole of the eye that supports the retinal ganglion cell axons as they exit the globe on their way to the brain (Sigal 2009). The LC biomechanical support is necessary to withstand the forces and deformations caused by intraocular pressure or other mechanical challenges. The ability of the LC to support the neural tissues is intrinsically dependent on the much stronger surrounding peripapillary sclera. While much has been learned about the LC, the peripapillary sclera and the crucial interplay between them (Downs, Roberts et al. 2011), far less is known about the LC beam insertions through which these two tissues interact. Studies of the LC-sclera simplify the interface between the tissues as a smooth continuum surface, ignoring that the LC beam insertions are discrete with complex shapes (Lee, Kim et al. 2014).

Using recently developed microscopy tools we obtained detailed information on the LC and sclera. Inspecting the LC-sclera interface it is readily visible that the LC insertions are complex, and that they vary greatly in shape. Some insertions resemble the wide roots of old trees,

whereas others look much thinner (Figure 6). These shapes suggest that the LC insertions likely also vary in how well they can satisfy the mechanical demands of the LC-sclera interface. Our goal was to characterize LC beam insertion shape in sheep, pig, monkey and human. We test the hypothesis that the LC insertion width and insertion angle vary between species.

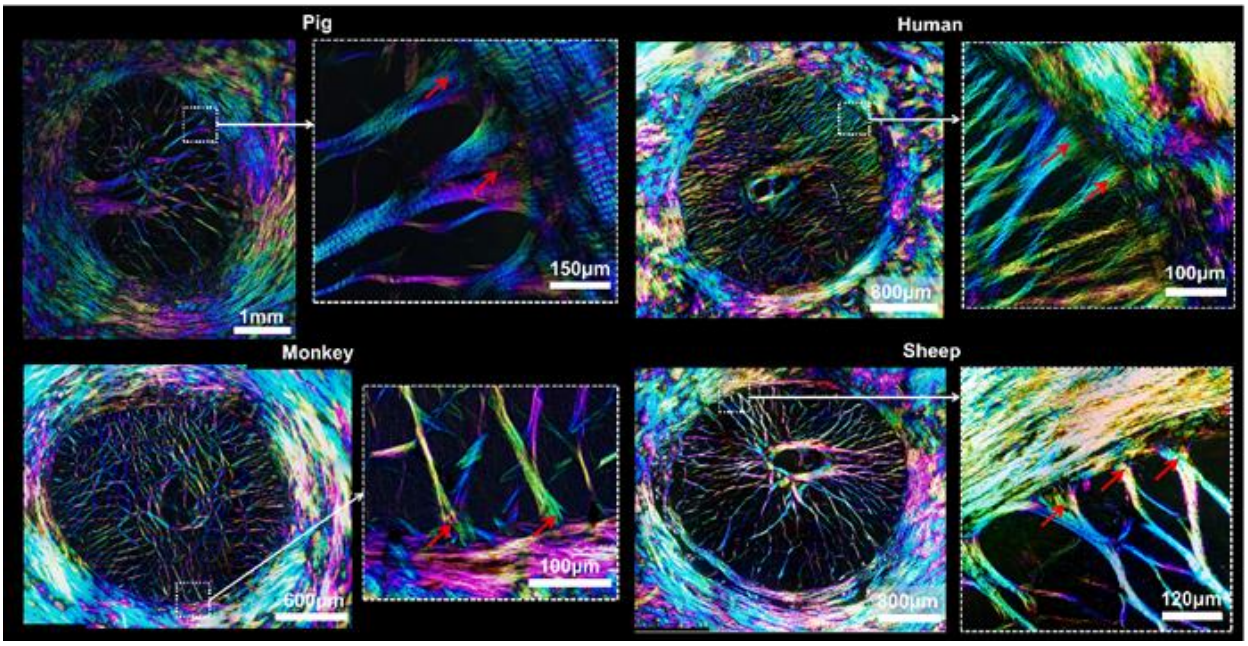

Figure 6. IPOL images of LC and sclera of eyes from the four species.For each species are shown a wide view of the whole scleral canal at the level of the LC, on the left, and a close-up, on the right, to illustrate typical insertions (red arrows).

2.2 Method

Sample preparation: two monkey eyes, three sheep eyes, two human eyes, and three pig eyes without known abnormalities were fixed. The LC and peripapillary sclera were trephined and cryosectioned coronally. From each eye, three sections located close to the LC midplane were selected for analysis.

Imaging: Sections were imaged with instant polarized light microscopy (IPOL) with a 10x strain-free objective (Olympus, Tokyo, Japan, 0.66um/pixel) (Lee, Yang et al. 2022). Because of the lower collagen density, the LC region often appears darker than the sclera. We therefore acquired images with various exposures to allow clear visualization of both tissues. Mosaics with 10% overlap were used to image whole sections. IPOL images reveal local collagen orientation and density in each pixel which helps visualize the LC beam and canal collagen structure.

Insertion quantification: We measured two parameters of each insertion: width and angle (Figure 7). Width was measured at the edge of the scleral canal. Angle was between the LC beam and the tangent of the sclera canal. Insertion angles range from 0 to 90 degrees, with 90 degrees being an LC insertion perpendicular into the canal wall. The parameters were measured from lines drawn manually using Fiji. Calculations were done in MATLAB v2022 (MathWorks, Natick, MA, USA).

Figure 7. Diagrams showing the definition of (left) insertion width and (right) insertion angle.

Statistics: Linear mixed effects (LME) models, accounting for autocorrelations between measurements from the same sections, eyes and species, were used to assess if the parameters of insertions were associated with species.

2.3 Results

Figure 8 shows the distributions of insertion widths and angles of the four species across all eyes. Insertion widths were significantly different between all species (p's<0.001), with widths (mean±SD, μm) in human (55.28±27.07), sheep (95.40±49.09), pig (137.02±79.91) and monkey (27.58±16.11).

Insertion angles of sheep and pig were larger than monkey and human (p's<0.05), with angles (mean±SD, degree) in human (70.74±14.4), sheep (76.43±11.66), pig (74.28±14.17) and monkey (70.88±16.06). No difference was detected in insertion angles between sheep and pig, and monkey and human.

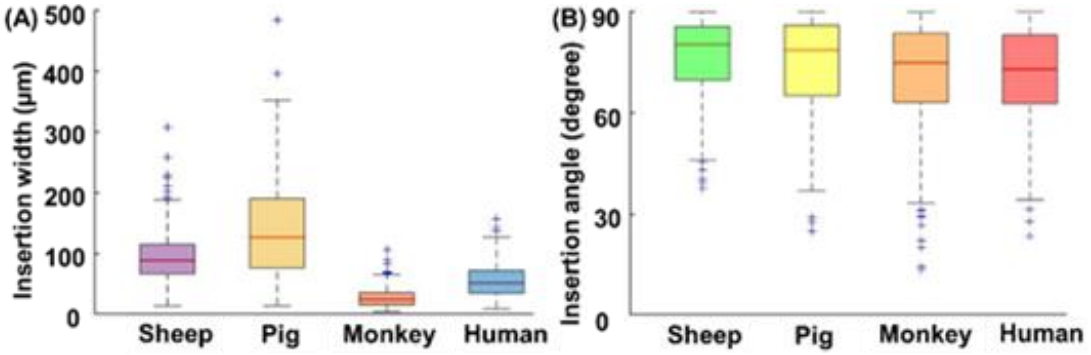

Figure 8. Box plots of insertion widths and insertion angles of each species.(A) There were significant and large differences in insertion widths between species. Pig exhibited the widest insertions, followed by sheep, human, and monkey. Additionally, the coefficient of variation (CV) was calculated for each species to quantify the relative variability in insertion widths. Human and sheep samples exhibited similar CV values of approximately 49.0% and 51.5%, respectively, suggesting in these groups consistent insertion width variations proportional to the absolute width. In contrast, pig and monkey samples demonstrated higher CV values of around 58.3%, indicating greater variability in insertion width proportionally to their widths. (B) Insertion angles of sheep and pig were larger than those of monkey and human samples. Sheep samples demonstrated a relatively low CV value of approximately 15.3%, indicating a more consistent pattern of insertion angles. In contrast, the pig, human, and monkey samples exhibited slightly higher CV values of

around 19.1%, 20.4%, and 22.7%, respectively, suggesting a broader range of insertion angles relative to their insertion angles within their respective groups.

2.4 Discussion

We present the first characterization of LC insertion width and angle. The discrete LC beam insertions could mean that the interaction between LC and surrounding load-bearing tissue is nonlinear and discontinuous over the canal. Different shapes of insertions can represent different levels of robustness of the LC periphery. The differences could result in different species susceptibilities to glaucomatous damage. Further work is necessary to understand the potential consequences of differences in angle.

3.0 Characterization Of Spatial Variations Of Monkey LC Insertions

The content of this chapter is in preparation.

3.1 Introduction

Glaucoma is characterized by the loss of retinal ganglion cell axons that are responsible for transmitting vision signals from the retina to the brain (Burgoyne, Downs et al. 2005, Sigal and Ethier 2009). Evidence shows that axon degeneration primarily occurs within a specialized structure in the optic nerve head (ONH), lamina cribrosa (LC) (Quigley, Flower et al. 1980, Hernandez 2000, Sigal and Ethier 2009). The LC biomechanical support is necessary to withstand the forces and deformations caused by intraocular pressure (IOP) or other mechanical challenges (Sigal, Flanagan et al. 2004, Burgoyne, Downs et al. 2005, Sigal and Ethier 2009, Roberts, Sigal et al. 2010, Behkam, Kollech et al. 2019, Ling, Shi et al. 2019). The ability of the LC to support the neural tissue is intrinsically dependent on the much stronger surrounding peripapillary sclera (Burgoyne, Downs et al. 2005, Sigal 2009, Sigal and Ethier 2009, Jonas, Jonas et al. 2011). The place where the LC and the sclera interact, that is LC insertions, serves an important role in connecting the two tissues and transmitting the forces and deformations in between. Therefore, the LC insertions can be crucial in influencing the biomechanical robustness of the LC and sensitivity to elevated IOP.

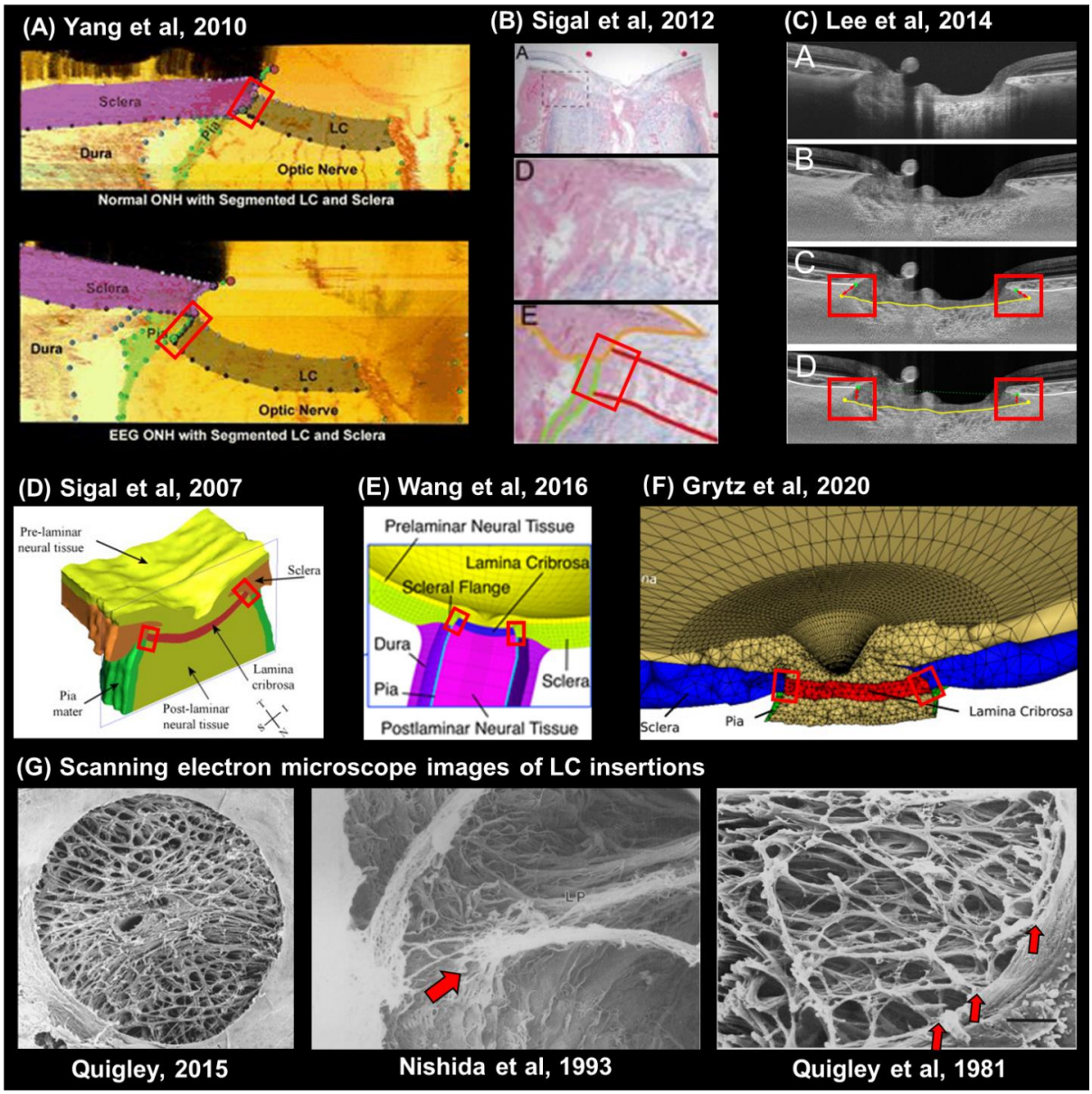

Figure 9. Illustration of conventional characterizations and mechanical models of LC insertions.Despite clear evidence that the LC-sclera interface is discrete (panel G), it is fairly common to think of the LC-sclera as a smooth continuum (panels A to F). (A) Histologic sections of a monkey with one normal eye and one eye affected by early experimental glaucoma (EEG), illustrating segmented LC inserting and interacting with scleral/pia tissues (adapted from Yang et al., 2010). (B) Bright field images of human ONH, highlighting LC inserting into sclera (yellow) and pia mater (green) (adapted from Sigal et al., 2012). (C) Swept-source optical coherence tomography (SS-OCT) images of human ONH, showing LC interactions with the scleral canal wall and quantifying anterior lamina cribrosa insertion distance (ALID) and marginal anterior laminar cribrosa

depth (mALCSD) (adapted from Lee et al., 2014). ALID refers to the distance between the anterior scleral canal opening (green dots, panel C) and the meeting point of the anterior laminar surface and the scleral canal wall (yellow dots, panel C). mALCSD refers to the perpendicular distance from the anterior scleral canal opening plane (green dashed line, panel D) to the anterior lamina cribrosa surface (yellow line, panel D) at the location of the anterior scleral canal opening (green dots, panel D). In this work we used a different definition of LC insertions. (D-F) Mechanical models of the ONH region (adapted from Sigal et al., 2007; Wang et al., 2016; Grytz et al., 2020). The location of LC insertions are highlighted using red boxes. Both the image characterizations and mechanical models assume the LC as a simple continuum structure interacting with the load-bearing surrounding tissue, overlooking its discrete nature. (G) Scanning electron microscopy (SEM) images showing the overview and closeup look of LC beams interacting with the sclera canal (adapted from Quigley, 2015; Quigley et al., 1981; Nishida et al., 1993), revealing the actual non-continuum nature of LC insertions. LC beam insertions are highlighted using red arrows. The left panel shows that LC beam distribution varies around the canal. The superior and inferior regions exhibit lower beam density and larger pores, potentially making them more vulnerable to glaucomatous damage. The overlooked discrete nature of LC insertions and regional anatomical differences drove our motivation for this study.

Many studies have been conducted to characterize LC insertions and learn its structural changes in the development of glaucoma (Yang, Williams et al. 2010, Sigal, Flanagan et al. 2012, Lee, Kim et al. 2014, Girard, Tun et al. 2015, Kim, Kim et al. 2015, Kim, Jeoung et al. 2016, Kim, Jeoung et al. 2016). Among them, a common measurement was the anterior LC insertions, representing the distance from the anterior surface of LC insertions to the reference plane connecting the Bruch's membrane openings (Girard, Tun et al. 2015, Kim, Jeoung et al. 2016, Kim, Jeoung et al. 2016). The results showed that the location of anterior LC insertions appeared to be more posteriorly located in patients with glaucoma compared with healthy ones. Another common measurement was focused on the posterior part of the LC insertions, characterized the posterior and outward migration of LC insertions from the sclera into the pia (Yang, Williams et

al. 2010, Sigal, Flanagan et al. 2012). While those studies were helpful in evaluating the LC insertion structure and changes, most of them characterized the insertions primarily in the sagittal plane and simplified LC insertions as a smooth continuum (Figure 9). Thus, these studies were limited in providing information about the LC insertions around the canal in the coronal plane, especially in anatomically critical regions (i.e., inferior-temporal region) which have been shown to be more susceptible to glaucoma damage. The complex microstructure of the LC insertions was also ignored and only the overall shape and position were examined. This was mainly due to the lack of tools to visualize and analyze the microstructure of LC insertions.

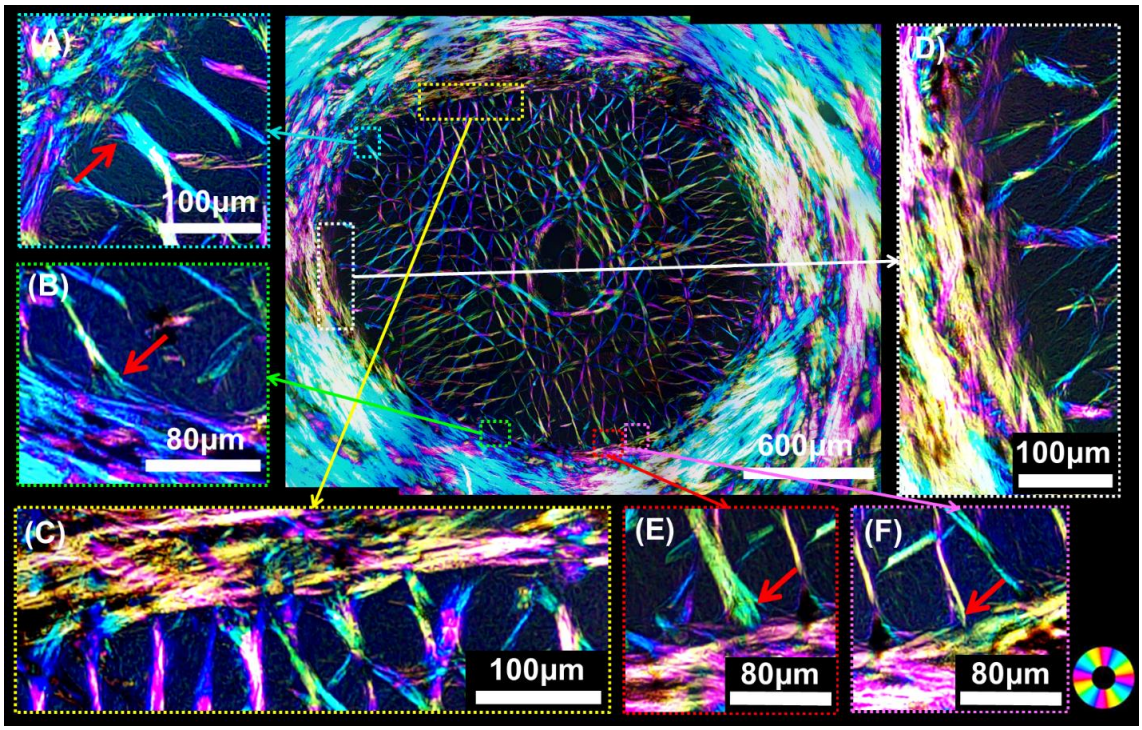

Figure 10. Example IPOL image of a monkey ONH coronal cryosection, showing the variations of LC insertions.The image was acquired with an objective with higher resolution (0.66μm/pixel) than the one used in this study for quantifications, for demonstration only. The sclera canal was over-exposed to highlight the LC beams. The colors represent local collagen fiber orientations which help discern the collagen structure. LC insertions are located at the edge where the LC beams join the sclera canal. We selected six regions to show the variations of LC insertions. (A) contains an LC insertion beam perpendicular to the canal wall,

whereas (B) contains a slanted insertion beam. (C) contains more insertions than (D), meaning that the number and density of insertions vary from location to location. (E) contains a wider insertion beam, whereas (F) contains a narrower insertion beam.

Using recently developed microscopy tools, we obtained detailed information on the LC and sclera (Yang, Jan et al. 2018, Ji, Yang et al. 2020, Yang, Lee et al. 2021, Lee, Yang et al. 2022). Inspecting the LC-sclera interface it is readily visible that the LC insertions consist of discrete LC beams inserted into the canal wall, and they vary greatly in shape and number (Figure 10). Some insertions resemble the wide roots of old trees, whereas others look much narrower. The insertion beams are nonuniformly distributed over the canal. A wider LC insertion may be able to support higher IOP-induced force than a narrower LC insertion, providing stronger support to neural tissues. The region with more LC insertion beams may be more robust than the region with fewer beams. This suggests that the LC insertions with different shapes and beam numbers likely vary in how well they can satisfy the mechanical demands of the LC-sclera interface. However, the LC insertion microstructure was largely ignored. To the best of our understanding, the only LC insertion microstructure characterization was acquired from single sections, with no information about the variations in-depth of LC (Ji, Yang et al. 2020). There was also a lack of characterization of the number or density of LC insertion beams around the sclera canal.

Our goal was to characterize the microstructural variations of the LC insertions in-depth of LC and in the four quadrants (superior, inferior, nasal, temporal). We tested the hypothesis that the shape and number of LC insertions were not uniform in-depth of LC and among quadrants. Specifically, we quantified four parameters of LC insertions (i.e., insertion width, insertion angle, number of insertions and insertion ratio) in monkey LC. The variations of LC insertions may lead to different LC robustness levels. Understanding the variations of LC insertions may help

understand the patterns of neural tissue damage and visual impairment associated with glaucomatous vision loss.

3.2 Methods

3.2.1 Eye Procurement, Preparation, And Sectioning

The study was conducted in accordance with the tenets of the Declaration of Helsinki and the Association of Research in Vision and Ophthalmology's statement for the use of animals in ophthalmic and vision research. We used six eyes of adult female rhesus macaque monkeys (Macaca mulatta), 12 to 16 years of age. These eyes were originally acquired for use in other studies and were obtained from collaborators from animals that had been used for studies not involving the eyes. The eyes were ostensibly healthy, without known abnormalities, and obtained and processed within 24 hours of death. The globes were processed as described previously (Jan, Grimm et al. 2015, Jan, Gomez et al. 2017). Briefly, the episcleral tissues, fat, and muscles were carefully removed. The globes were pressurized and immersion fixed in 10% formalin solution overnight. Due to the different requirements of the other studies, the pressures varied between 5 to 25 mmHg. After fixation, the ONH and posterior pole were excised with a circular trephine. The excised regions were cryosectioned coronally at 16 μm starting from the posterior side. Sections were collected without loss, starting when there was visible sclera and stopping when the canal was no longer visible.

3.2.2 Imaging And Registration

Sections with visible LC insertion beams were selected for imaging. The selected sections, 15 sections from each eye, were imaged with the instant polarized light microscopy (IPOL) reported previously (Yang, Lee et al. 2021, Lee, Yang et al. 2022). Briefly, the IPOL imaging system was developed on an inverted microscope (Olympus IX 83, Olympus, Tokyo, Japan) by retrofitting a polarization encoder in the illumination path and a polarization decoder in the imaging path. Each polarizer group consisted of a linear polarizer and a z-cut quartz plate. Linear polarizers in the polarization encoder and decoder were orientated orthogonally. A 4x strain-free objective (Olympus, Tokyo, Japan) was used for imaging (1.49μm/pixel).

The LC region appeared darker than the sclera canal, mainly due to the lower collagen density in the LC region than in the sclera. Therefore, when necessary, we allowed slight over-exposure of the sclera canal to highlight the LC structure. The IPOL images displayed the collagen orientation and density in each pixel which helped better visualize the LC structure. Because the sections were large, multiple images were captured (10% overlap) and stitched into mosaics to cover the whole section. Images from the same eye were stacked sequentially and registered to the most posterior image. The registration was done manually based on tissue edges.

3.2.3 Insertion Quantification

We quantified four insertion parameters, insertion width, insertion angle, insertion ratio and number of insertions (Figure 11). Insertion width was defined as the width of the LC beam at the edge of the sclera canal. Insertion angle was the angle between the LC insertion beam and the tangent of the sclera canal. Insertion angle ranged from 0 to 90 degrees. 90 degrees meant an LC

insertion was perpendicularly inserted into the canal wall, while 0 degrees meant the LC beam parallelly joined the canal. Insertion ratio was quantified as the ratio between the area of insertions and the area of sclera around the LC. Number of insertions was the number of distinct LC beams inserted into the canal wall. The parameters were measured in each section in-depth of LC and in each quadrant (i.e., superior, inferior, nasal, temporal).

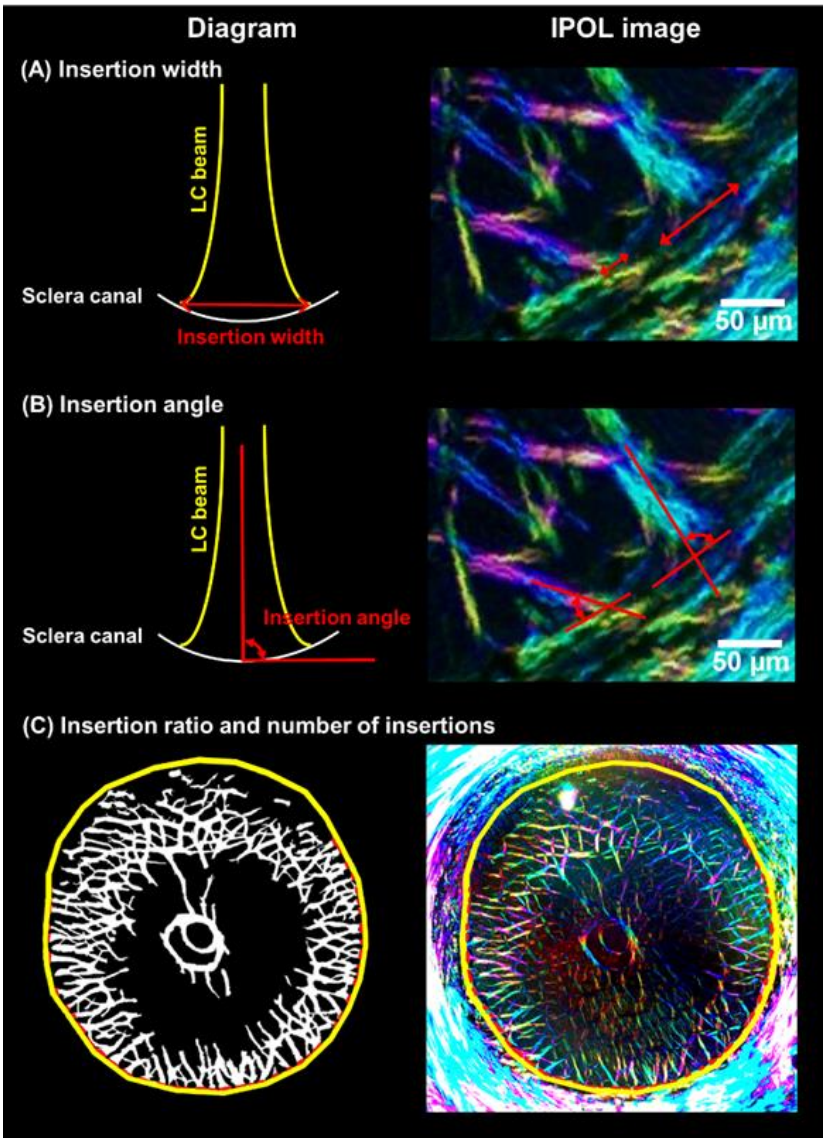

Figure 11. Definitions of insertion parameters.(left column) Schematic diagrams and (right column) IPOL images showing the definition of insertion width, insertion angle and insertion ratio. (A) (left) Insertion width was defined as the LC beam width at the sclera canal. (right) Two LC insertions with different widths. The

insertion width was quantified by marking with a straight line and calculating the length of the line. (B) (left) Insertion angle was defined as the angle between the LC beam and the tangent of sclera canal. (right) Two LC insertions with different insertion angles. For each insertion angle, we marked the direction of the canal tangent and the LC beam with two straight lines. The insertion angle was calculated as the acute angle between the two lines. (C) (left) Insertion ratio was defined as the ratio between the area of insertions and the area of sclera canal. It was calculated as the ratio between the sum of all the insertion lengths (red) and the length of the canal opening at that depth (yellow). Number of insertions is the count of distinct LC insertion beams. (right) Manual markings of the canal wall and the beam widths were overlayed on the IPOL image for demonstration.

The parameters were measured from lines drawn manually. All the manual markings in this section were done using FIJI is Just ImageJ (FIJI) (Preibisch, Saalfeld et al. 2009, Schindelin, Arganda-Carreras et al. 2012). For insertion width, we marked the width using a straight line and calculated the length of the line. For insertion angle, we marked two straight lines, indicating the direction of the LC beam and the direction of the local canal tangent, respectively. We calculated the acute angle between the two lines as the insertion angle. We counted the number of insertion width markings as the number of insertions. Note that when marking to get insertion widths, insertion angles, and counting the number of insertions, we compared the adjacent sections to avoid duplicate counting of the LC insertion beams that appeared in more than one section.

For insertion ratio, we manually marked along the edge of the sclera canal from each section, indicating the in-depth position and the quadrant. We re-marked the insertion widths following a similar procedure described previously. Different from the method we used for quantifying insertion width, we marked the widths of all the LC insertion beams that were visible in a section, even though the same beam may appear in multiple sections. We calculated the

insertion ratio as the sum of all LC beam widths divided by the perimeter of the canal. The calculations were done in MATLAB v2022 (MathWorks, Natick, MA, USA).

3.2.4 Statistics

Linear mixed effects (LME) models, accounting for autocorrelations, or dependent similarities, between measurements from the same section, eye and species, were used to assess if the parameters of insertions were associated with in-depth positions or quadrants.

3.3 Results

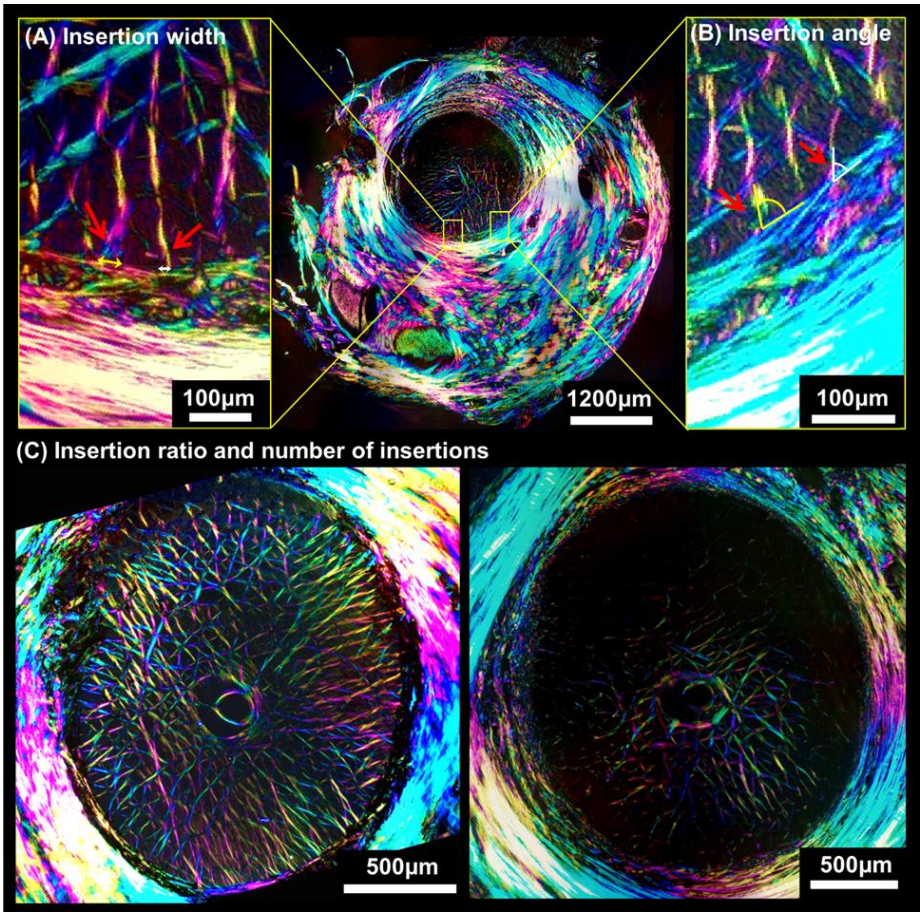

Figure 12. Variations of insertion parameters.(A) showed two insertions with different insertion widths. (B) showed two insertions with different insertion angles. (C) The two sections were selected from the same monkey eye. The left section was located closer to the midplane of LC and the right section was located closer to the posterior LC surface. The left section showed a greater number of insertions and a larger insertion ratio, whereas the right section contained significantly sparse insertions.

Figure 12 shows examples of LC insertions with varying insertion widths, insertion angles, number of insertions and insertion ratios. Even when two insertion beams are close, they can differ significantly in width and angle, where one beam can be twice as wider as the other one, and the

insertion angles can differ by more than 10 degrees. Two sections located at different distances from the LC midplane showed significant differences in the number and density of insertions.

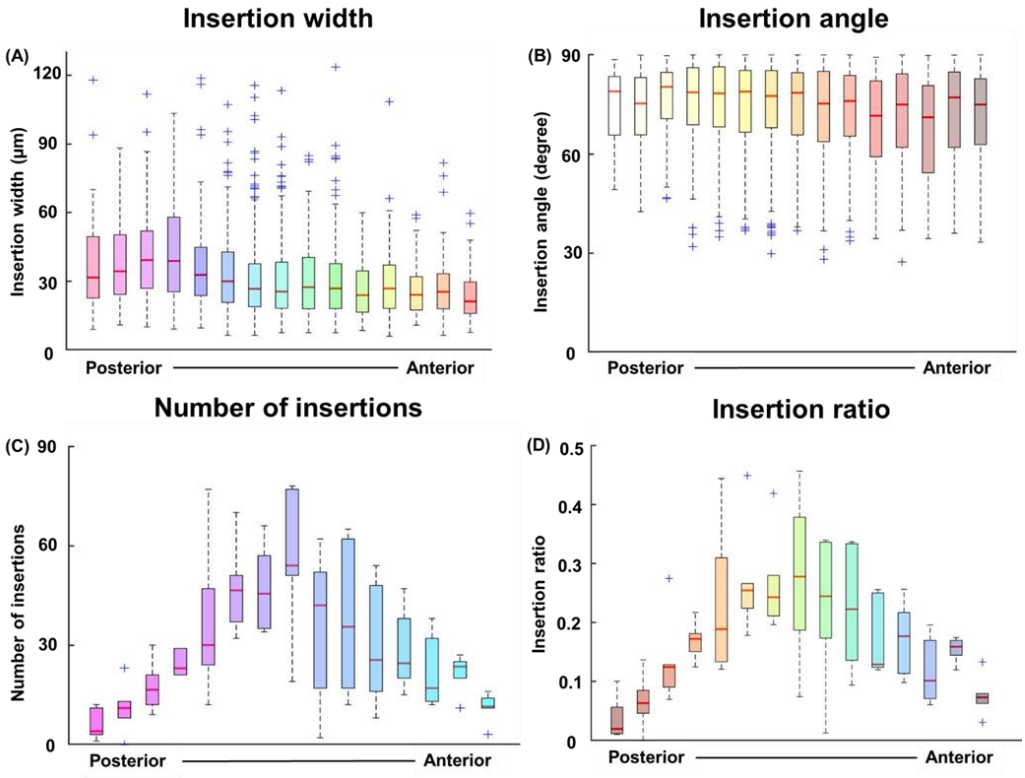

Figure 13. Variations of insertion width, insertion angle, number of insertions, and insertion ratio by depth.(A, B) Insertions in the most anterior LC were more slanted and significantly narrower than in the posterior LC (p's<0.001). (C, D) More insertions covered a larger ratio of the canal wall in the middle LC than in the anterior and posterior LC (p's<0.001).

Figure 13 shows that insertions in the posterior LC were wider and with larger insertion angles than those in the anterior LC (p's<0.001). In the most posterior LC, insertions widths were 38.56±23.52 (mean ± STDEV, μm) and insertion angles were 74.49±11.65 (mean ± STDEV, degree). When going in-depth of LC from posterior to anterior for 16 μm, insertion widths decreased by 1.29 μm (p<0.001), and insertion angles decreased by 0.48 degrees (p<0.001). There were a greater number of insertions and a larger insertion ratio in the middle LC than in the anterior

and posterior LC (p's<0.001). The section contained the maximum number of insertions and the largest insertion ratio was located at the midplane, having an average of 55 insertion beams and a 28% of insertion ratio.

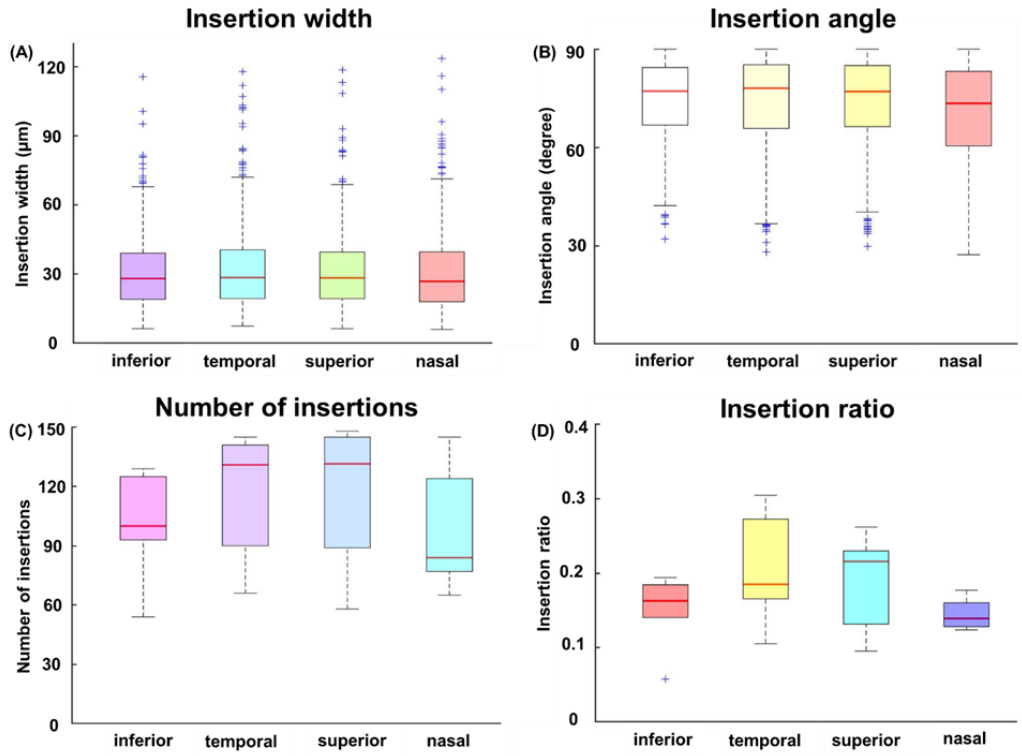

Figure 14. Variations of insertion width, insertion angle, number of insertions, and insertion ratio by quadrants. (B) Insertion angles in the nasal quadrant were significantly smaller than in the other quadrants (p<0.001). (A, C, D) Insertion width, number of insertions and insertion ratio were not significantly different among quadrants.

Figure 14 shows that in the nasal quadrant, insertion angles were 3.5 degrees significantly smaller than the other three quadrants (p<0.001). No significant differences in insertion width, ratio and number were detected among quadrants.

Figure 15 to Figure 20 depict the variations in insertion parameters from posterior LC to anterior LC and among the four quadrants, with data from individual monkey eyes. Each eye

exhibits relatively consistent pattern of insertion widths, number of insertions and insertion ratios. Wider insertions were observed in the posterior LC compared to the anterior LC. Additionally, in every eye, the middle LC exhibited a higher number of insertions and insertion ratios compared to the anterior and posterior LC.

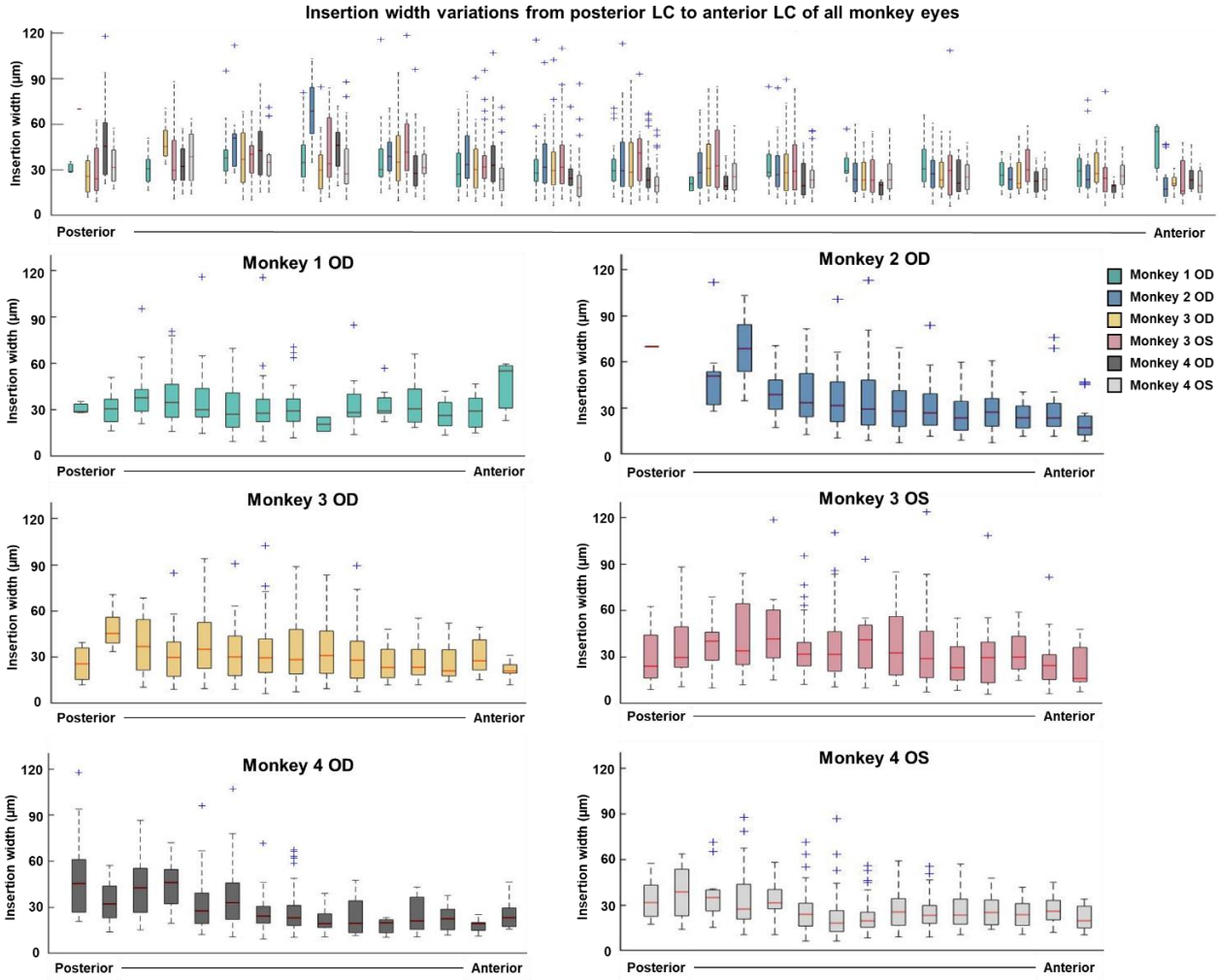

Figure 15. Insertion width variations in individual monkey eyes.The top panel illustrates the posterior-to-anterior insertion width changes across all six monkey eyes. The bottom six panels provide better visualization of the insertion widths for each eye. Notably, except for Monkey 1 OD, the LC insertions in the posterior LC were wider compared to the anterior LC (p's<0.01).

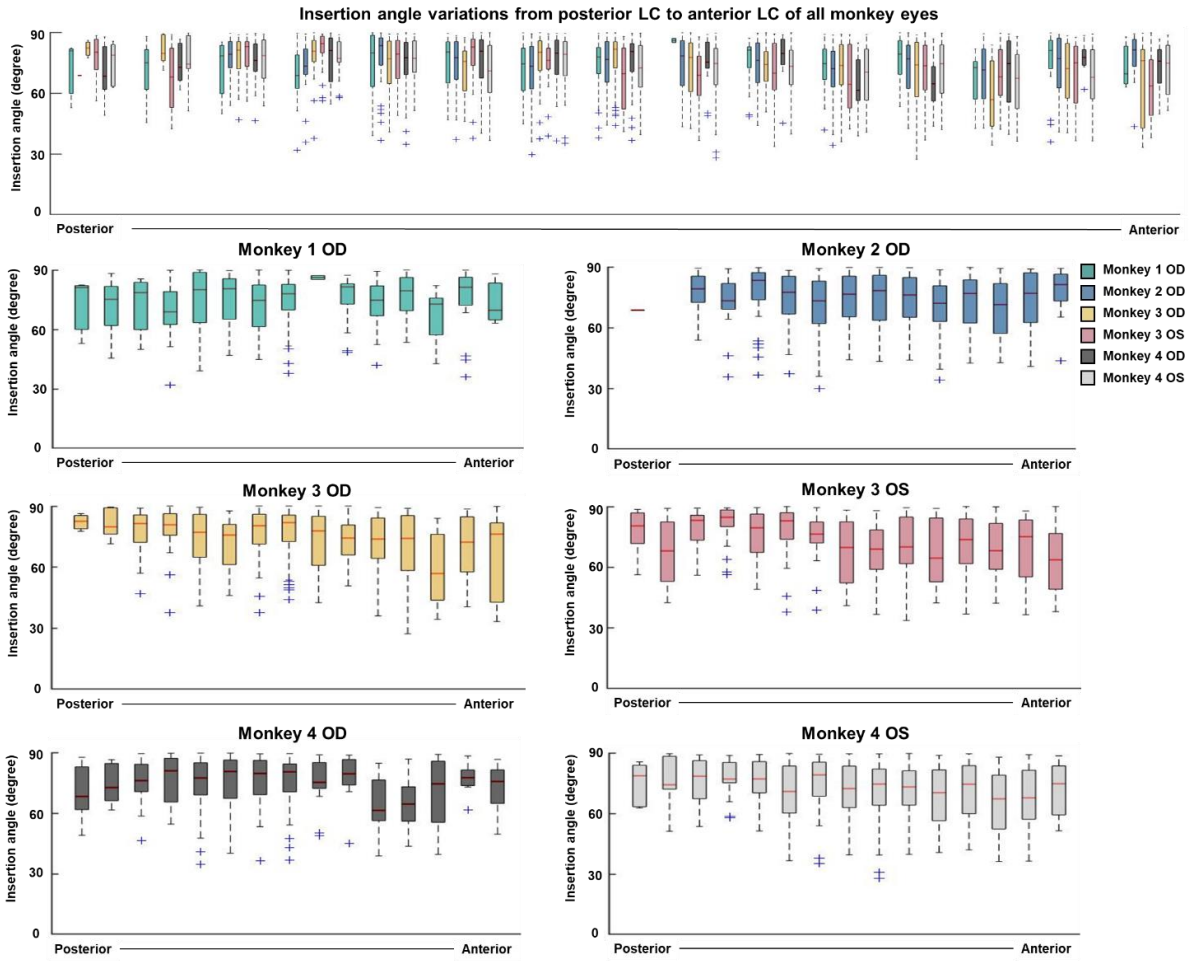

Figure 16. Insertion angle variations in individual monkey eyes.The top panel illustrates the posterior-to-anterior insertion angle changes across all six monkey eyes. The bottom six panels provide better visualization of the insertion angles for each eye. In Monkey 3 OD, Monkey 3 OS, and Monkey 4 OS, the insertion angles were larger in the posterior LC than in anterior LC (p's<0.01).

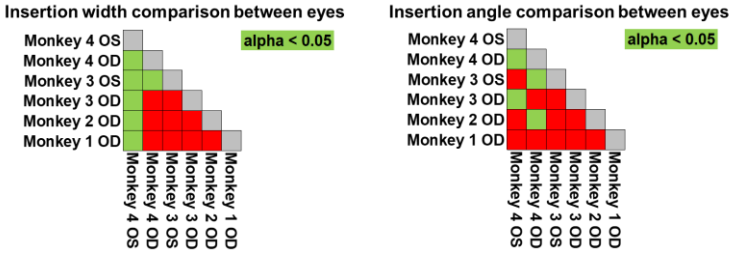

Figure 17. Matrix of LME tests doing pair-wise comparisons of (left) insertion widths and (right) insertion angles between eyes.Monkey 4 OS demonstrates significantly smaller insertion widths compared to other eyes

(p's < 0.05). Additionally, significant differences in insertion angles reveal that Monkey 4 OS has smaller insertion angles than Monkey 3 OD and Monkey 4 OD, while Monkey 4 OD exhibits larger insertion angles than Monkey 2 OD and Monkey 3 OS (p's < 0.05).

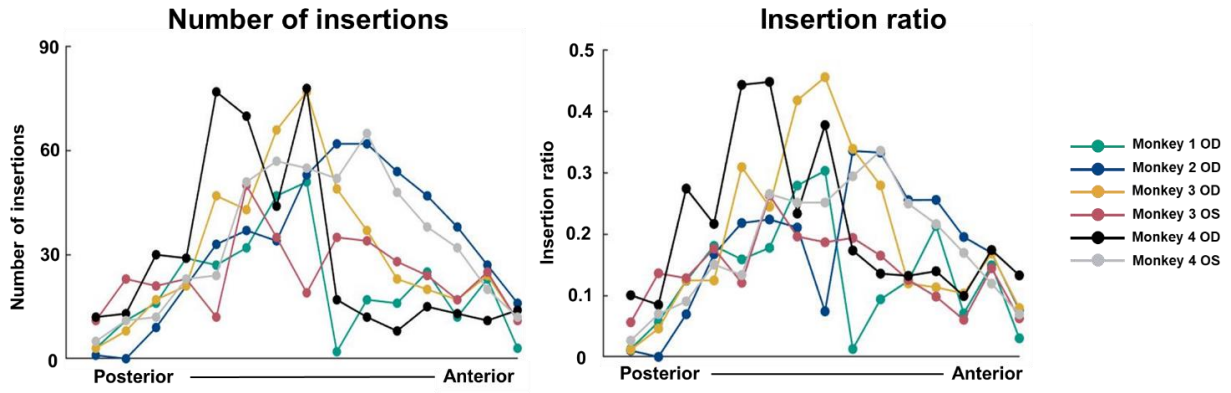

Figure 18. Line plots illustrating variations in the number of insertions (left) and insertion ratio (right) from posterior LC to anterior LC of each monkey eye.In every eye, the middle LC displays a greater number of insertions and larger insertion ratio in comparison to the anterior and posterior LC segments.

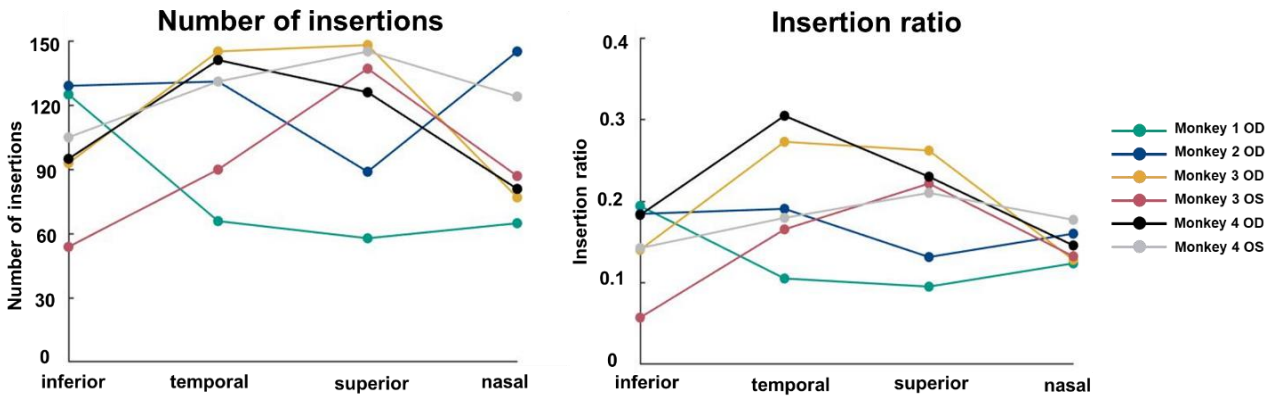

Figure 19. Line plots illustrating variations in the number of insertions (left) and insertion ratio (right) across the four quadrants of each monkey eye.

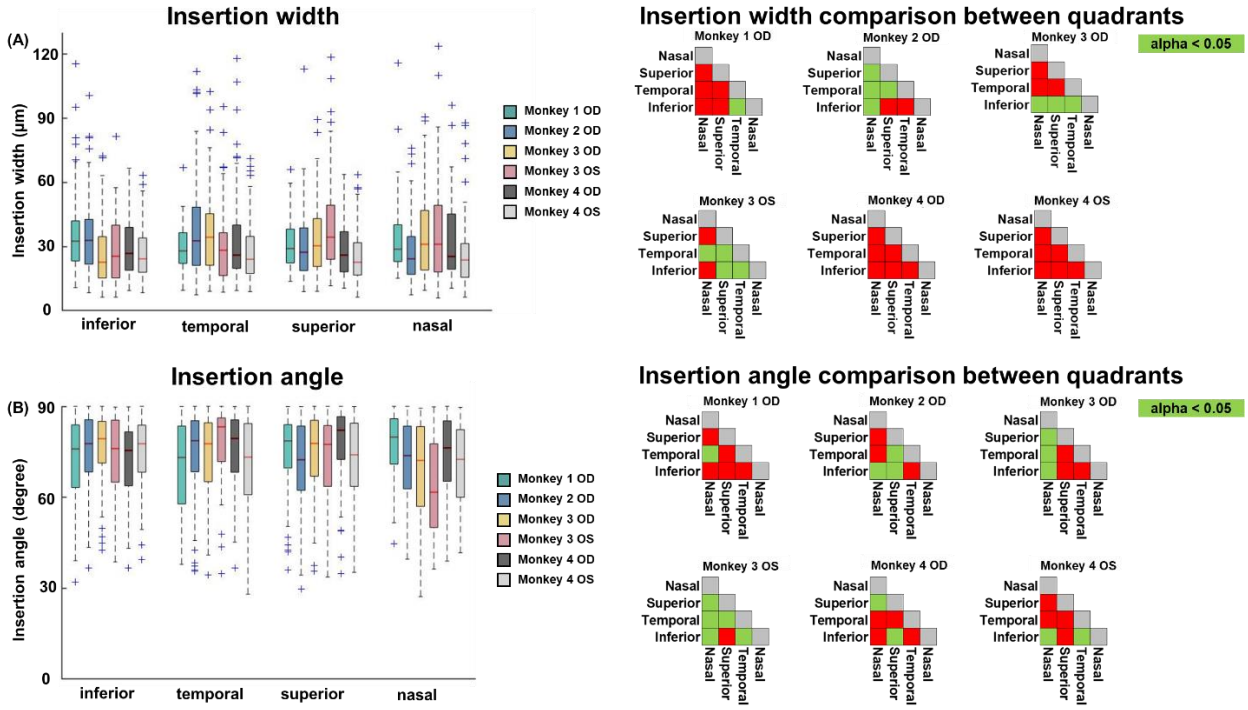

Figure 20. Variations in (A) insertion width and (B) insertion angle among each monkey eye.The matrix of LME tests illustrates pair-wise comparisons of these parameters between quadrants.

Considerable variations in insertion angles were observed across different eyes, indicating the absence of a consistent pattern valid for each individual eye. Similarly, the variations in insertion width, insertion ratio and number of insertions among the quadrants were also substantial, and no clear pattern was detected that could be applied consistently to each eye. Furthermore, the insertion parameters from eyes belonging to the same animal were not found to be more similar compared to unrelated eyes.

Table 1 shows that on average, each monkey eye has 431 insertions (± standard deviation 75) with an insertion ratio of 0.1715 (± standard deviation 0.0315).

Table 1. Number of insertions and insertion ratio in the whole LC region of individual monkey eyes. On average, the number of insertions in each monkey eye was found to be 431 (± standard deviation of 75), with an insertion ratio of 0.1715 (± standard deviation of 0.0315).

	Number of insertions	Insertion ratio
Monkey 1 OD	314	0.1318
Monkey 2 OD	494	0.1681
Monkey 3 OD	463	0.1972
Monkey 3 OS	368	0.1421
Monkey 4 OD	443	0.2142
Monkey 4 OS	505	0.1756

3.4 Discussion

Our goals were to carry out the first characterization of LC insertions in monkey and to test the hypothesis that the shape and number of LC insertions vary in-depth of LC and between quadrants. We characterized the LC insertions from six monkey eyes and quantified four parameters, insertion width, insertion angle, number of insertions and insertion ratio. The variations of the parameters were compared in-depth of LC and among the superior, inferior, nasal and temporal quadrants. Three major results arise from this work. First, insertion widths were larger in the posterior LC than in the anterior LC. Second, insertion angles were smaller in the anterior LC and in the nasal quadrant. Third, the number of insertions and insertion ratios were larger in the sections closer to the LC midplane and were smaller in the sections closer to the LC anterior/posterior surface. The three results were discussed in more detail below.

We found that insertion widths were larger in the posterior LC than in the anterior LC. A wider insertion beam can be stronger than a narrower insertion. Thus our observation means that the anterior LC can be weaker than the posterior LC. This potentially could contribute to the LC

remodeling in the development of glaucoma. Increased IOP is the primary risk factor of glaucoma. Under elevated IOP, two major changes have been observed, prelaminar neural tissue thinning and posterior (outward) migration of LC connective tissue (Yang, Williams et al. 2011, Grytz, Sigal et al. 2012, Burgoyne 2015, Kim, Jeoung et al. 2016). The weaker anterior LC can be less robust to support the neural tissue under increased load compared to the posterior LC, thus contributing to the prelaminar neural tissue thinning. The weak anterior LC insertion beams can fail earlier in the development of glaucoma, resulting in the progressive posterior migration of LC connective tissue. This explanation is consistent with a common assumption made in many studies, arguing that IOP-related deformations cause acute failure of the anterior laminar beams, thereby transferring load to adjacent beams in a cascade of damage that results in the glaucomatous cupping (Jonas, Berenshtein et al. 2004, Burgoyne, Downs et al. 2005, Downs, Roberts et al. 2008, Sigal and Ethier 2009).

We found that the insertion angles were smaller in the anterior LC than in the posterior LC. Insertion angles in the nasal quadrant were also found smaller than in the other three quadrants. A 90-degree, large insertion angle means a radially oriented LC insertion beam, while a 0-degree, small insertion angle means an LC beam tangentially inserted into the canal wall. This difference potentially can influence the behaviors of canal expansion when subjected to IOP load. For instance, regions with more tangentially aligned LC insertion beams can be less robust to withstand canal expansion, meaning that canal expansion will be dominant in that direction. Canal expansion will pull the LC radially and impart significant tensile strain on LC structure and neural tissue (Downs 2015, Downs and Girkin 2017), making the region more susceptible to glaucomatous damage. Under this circumstance, we expect that the smaller insertion angles of the anterior LC may not provide the robust support afforded by the insertions of the posterior LC. Under the

stresses of chronic IOP, damage to more fragile anterior LC insertions could contribute to LC bowing and deepening observed in glaucoma. This sounds like a reasonable hypothesis, but the quadrant variations of insertion angles could not explain previous findings related to regional susceptibilities, which showed that inferior-temporal and superior-temporal quadrants of the ONH are more susceptible to damage in early glaucoma (Kiumehr, Park et al. 2012, Lisboa, Leite et al. 2012). Perhaps it is because insertion angles have other implications that we haven't understood. Further work is necessary to test our hypothesis and to understand the detailed biomechanical role of insertion angles.

We found that the number of insertions and insertion ratios were larger with greater variability in sections closer to the LC midplane and smaller in the sections closer to the LC anterior/posterior surface. These variations could impact how forces and deformations are transmitted between the sclera canal and LC. The discrete LC beam insertions may imply that the interactions between LC and surrounding load-bearing tissues are nonlinear and discontinuous over the canal, with forces concentrated in where the LC beams are inserted into the canal. Regions with more beams and a larger portion of LC periphery attached to the canal wall may imply that these regions are stronger in supporting the neural tissues. However, due to the lack of information about LC insertion microstructure, number of insertions and insertion ratios were not considered previously. Instead, when modeling the ONH biomechanics, it was commonly assumed that the LC and LC insertions are continuum structures that cover 100% of the canal perimeter (Sigal, Flanagan et al. 2005, Sigal, Flanagan et al. 2009, Roberts, Liang et al. 2010, Grytz, Sigal et al. 2012). In fact, only 20 to 40 percents of the canal perimeter area is connected with LC beams. Ignoring the variations of number of insertions and insertion ratio may misinterpret the interactions between the LC and the surrounding loading-bearing tissues, which could impair our

understanding of the biomechanical robustness of the LC and sensitivity to elevated IOP (Figure 21) (Burgoyne, Downs et al. 2005, Sigal 2009, Jonas, Jonas et al. 2011, Sigal, Flanagan et al. 2012). Thus, it is beneficial to consider these two parameters in numerical models, and future study is important to explore their biomechanical roles.

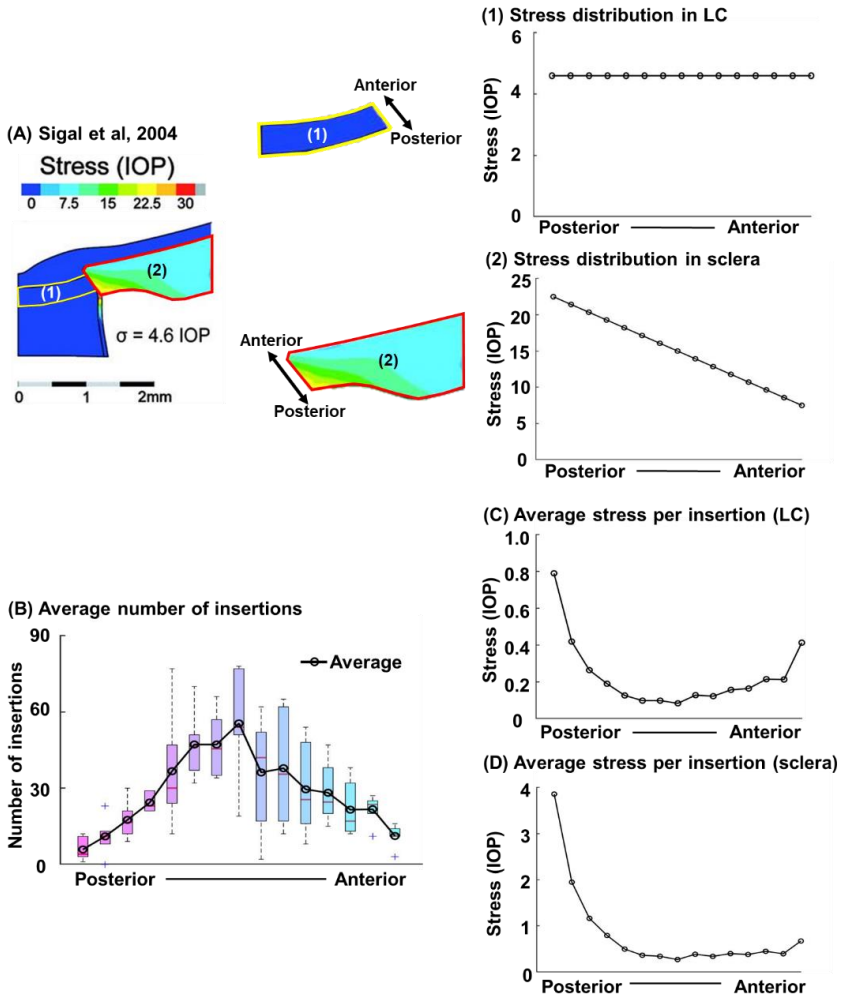

Figure 21. Variations in number of insertions and their impact on stress distribution in the ONH region.(A) Adapted from Sigal et al., 2004, this figure demonstrates the von Mises equivalent stress of the ONH region under an IOP of 50 mmHg. The stress is presented as multiples of IOP, providing insights into the forces acting within the tissue. The LC (yellow region) interacts with the sclera (red region) through LC insertions. (1) The stress within the LC region is relatively uniform at 4.6 IOP, while (2) the stress at the scleral canal edge varies from 7.5 IOP to 22.5 IOP from anterior to posterior. (B) The number of insertions across the 6

monkey eyes, spanning from the posterior LC to the anterior LC. Box plots illustrate the variations, while the black line represents the average number of insertions at different depths. (C) In contrast to the continuum approach in panel (A), where LC insertions were treated as a continuum, considering the average stress acting through the LC and borne by each insertion reveals significantly higher stress per insertion beam at the posterior and anterior LC surfaces. (D) Similarly, by assessing the average stress acting through the scleral tissue and borne by each insertion, it becomes evident that the average stress per insertion beam is 8 times higher in the posterior LC compared to the mid-plane of the LC. Consequently, the LC beams located at the posterior and anterior surfaces may face a higher risk of damage when subjected to increased IOP. Such critical information is not available if we study the LC insertions as a continuum.

This study was conducted using the IPOL imaging system. Although an objective with a higher imaging resolution was available (0.66μm/pixel), we chose to use the objective with a lower imaging resolution (1.49μm/pixel). Imaging with a lower resolution allows a higher speed of imaging and requires lower computer memory. To check the influence of the different imaging resolutions, we imaged the sections of two monkey eyes with both objectives and marked the insertions twice. We compared the parameters of insertions obtained from the images with different resolutions, and we found that there was no significant difference. Thus, we believe that the measurements in this study were independent to the variations of imaging resolutions.

There are two limitations to consider. First, we quantified the LC insertions only in monkey. Monkey and human LCs are different in geometry, where previous studies have reported the difference in LC shape and insertion widths between the two species (Tran, Wallace et al. 2017, Ji, Yang et al. 2020). Thus, the results of this study have limited application to human eyes. We position that it's important to understand monkey as an animal model (Rasmussen and Kaufman 2005, Burgoyne 2015). In future studies, it will be necessary to study LC insertions in other animal models and in human eyes.

Second, when mounting the ONH sample for sectioning, we leveled the LC surface and made it parallel to the sectioning plane. However, it was still possible that the LC surface was tilted at an angle relative to the sectioning plane, which could influence the measurements of the in-depth variations. We quantified the angle of tilting from the six eyes and found that the average tilted angle was 3.1 degrees, which was small and should not cause significant impact on the measurements. In the future, it would be beneficial to come up with advanced image processing methods to resolve the issue of tilting when needed.

In conclusion, we have characterized the insertion width, insertion angle, number of insertions and insertion ratio in monkey LC. We found substantial and significant variations of LC insertions in-depth of LC and among quadrants. Different shapes and varying number of LC insertions may represent different levels of robustness of the LC periphery. Understanding these differences potentially could contribute to a better understanding of the regional susceptibilities to glaucomatous damage.

4.0 Characterization Of In-Depth Collagen Fiber Organization Across The Corneoscleral Shell

The content of this chapter has been published by Experimental Eye Research (Ji, Quinn et al. 2023).

4.1 Introduction

The biomechanics of the eye corneoscleral shell are important in the basic eye function and are heavily influenced by the collagen fiber organization (Ethier, Johnson et al. 2004, Coudrillier, Boote et al. 2013). Accurate information on the corneoscleral shell collagen fiber organization is thus important to understand the eye's physiological load-bearing behavior and biomechanics-related diseases, such as glaucoma (Grytz, Meschke et al. 2011, Coudrillier, Pijanka et al. 2015).

Many studies have been conducted to study the collagen fiber organization of the corneoscleral shell (Boote, Hayes et al. 2006, Abahussin, Hayes et al. 2009, Girard, Dahlmann-Noor et al. 2011, Pijanka, Coudrillier et al. 2012, Coudrillier, Boote et al. 2013, Winkler, Shoa et al. 2013, Abass, Hayes et al. 2015, Jan, Lathrop et al. 2017, Gogola, Jan et al. 2018, Koudouna, Winkler et al. 2018, Yang, Brazile et al. 2018, Yang, Jan et al. 2018). These studies have revealed that the collagen architecture of corneoscleral shell is a complex 3D anisotropic, interwoven and inhomogeneous structure. The studies have shown, for instance, that the cornea exhibits a layered structure of lamellae. In terms of the overall cornea architecture, the studies have shown that the anterior cornea has no preferred lamella orientation, whereas the middle and posterior parts of the

cornea show an orthogonal arrangement of collagen fibers preferentially aligned in the superior-inferior and nasal-temporal axes (Boote, Hayes et al. 2006, Abahussin, Hayes et al. 2009). In the limbus, fibers form a circumferential ring (Newton and Meek 1998, Boote, Hayes et al. 2006). For the sclera, the studies have shown circumferential fibers surrounding the canal, radial fibers extending out from the canal, and interwoven fibers distributed throughout the thickness. (Girard, Dahlmann-Noor et al. 2011, Jan, Lathrop et al. 2017, Gogola, Jan et al. 2018).

The vast majority of studies of sclera fiber orientation, while helpful, have centered on characterizing collagen fiber architecture in the tissue plane. For the front and back of the eye this has meant the characterization of fiber orientations on a coronal plane, with analysis of other regions usually involving tissue patches analyzed transversely. Interested readers can consult two good examples of this approach aimed at mapping scleral fiber orientations in rat (Girard, Dahlmann-Noor et al. 2011) and human (Pijanka, Abass et al. 2013). For the cornea we recommend two (Winkler, Shoa et al. 2013, Meek and Knupp 2015). Studies of fiber orientation often involve the explicit or implicit assumption that the primary orientation of the fibers is close to that of the tissue plane (e.g. with the fibers exhibiting zero inclination angles relative to the local tissue plane). This is particularly common in numerical modeling of the peripapillary sclera (Zhang, Albon et al. 2015, Voorhees, Jan et al. 2018). From a mechanical perspective, this allows several convenient simplifications, such as modeling the corneoscleral shell as a thin shell structure, reducing computational demands. (Arciniegas and Amaya 1986, Watson and Young 2004, Kimpton, Walker et al. 2021). A few studies have explored depth-dependent variations in fiber orientation in both cornea and sclera (Abahussin, Hayes et al. 2009, Hayes, Khan et al. 2012, Pijanka, Coudrillier et al. 2012, Danford, Yan et al. 2013, Pijanka, Spang et al. 2015, Gogola, Jan et al. 2018). These have still primarily focused on analyzing the variations in the in-plane fiber

orientations across depth, such as the depth-dependent “rotation” of lamellae cross patterns (Vohnsen and Artal 2008, Latour, Gusachenko et al. 2012, Koudouna, Winkler et al. 2018). The information on these studies often comes from serial coronal section or from optical cross-sectioning in-depth. The characterization is therefore still primarily in-plane, with very limited information about fibers that have an inclination with respect to the tissue plane.

A few studies have been directed at quantifying and understanding collagen fibers that are not the tissue plane. Two notable studies analyzed cornea fiber orientations on the axial plane (Winkler, Shoa et al. 2013, Abass, Hayes et al. 2015). The authors noted a population of collagen fibers that are branching, interweaving and transversely inclined in-depth of cornea. The inclined fibers create a high degree of interconnectivity between fiber lamellae layers and appear to be useful for reducing fiber slippage, making the cornea more mechanically stable, and increase cornea stiffness (Morishige, Wahlert et al. 2007, Winkler, Chai et al. 2011, Petsche and Pinsky 2013). Studies looking at longitudinal sections show that in-depth collagen fibers also exist outside of the cornea, with potentially important mechanical roles (Yang, Jan et al. 2018). However, they remain uncharacterized in most of the globe, limiting our ability to understand their roles.

Our goal in this work was to quantify in-depth collagen fiber organization over the corneoscleral shell. These in-depth features of the collagen organization shed light on how fibers are organized within the cross-section of the tissue thickness. Specifically, we quantified collagen fiber orientation distribution, anisotropy, and fiber inclination in 15 regions and over the whole corneoscleral shell. The results of this study represent new quantitative data of in-depth fiber organization that will enhance understanding of the eye tissue collagen fiber organization, and in turn, eye biomechanics.

4.2 Methods

4.2.1 Sample Preparation

The study was conducted in accordance with the tenets of the Declaration of Helsinki and the Association of Research in Vision and Ophthalmology's statement for the use of animals in ophthalmic and vision research. Seven whole globe axial sections from 3 eyes of 3 sheep were used for the analysis: three sections from one eye, and two sections each from the remaining two eyes. The sections were originally prepared and processed by the University of Pittsburgh Ocular Biomechanics Lab for other purposes, with particular attention given to consistent tissue handling and imaging for all eyes and sections. Histological processing was as described elsewhere (Jan, Grimm et al. 2015, Jan, Gomez et al. 2017, Jan, Lathrop et al. 2017). Briefly, eyes from healthy sheep were obtained from the local abattoir and processed within 24 hours of death. The episcleral tissues, fat, and muscles were carefully removed. The globes were pressurized to 50 mmHg and immersion fixed in 10% formalin solution overnight. The intact whole globe eyes were embedded in such a way that all eyes lined up in the nasal-temporal anatomical directions for cryo-sectioning. The eyes were cryo-sectioned into axial slices, with a section thickness of 30 μm. For all eyes, the sections were obtained consecutively without loss. For imaging and analysis we selected 7 sections passing through both peripapillary sclera (PPS) and central cornea and free of artifacts, such as folds or bubbles (Figure 22).

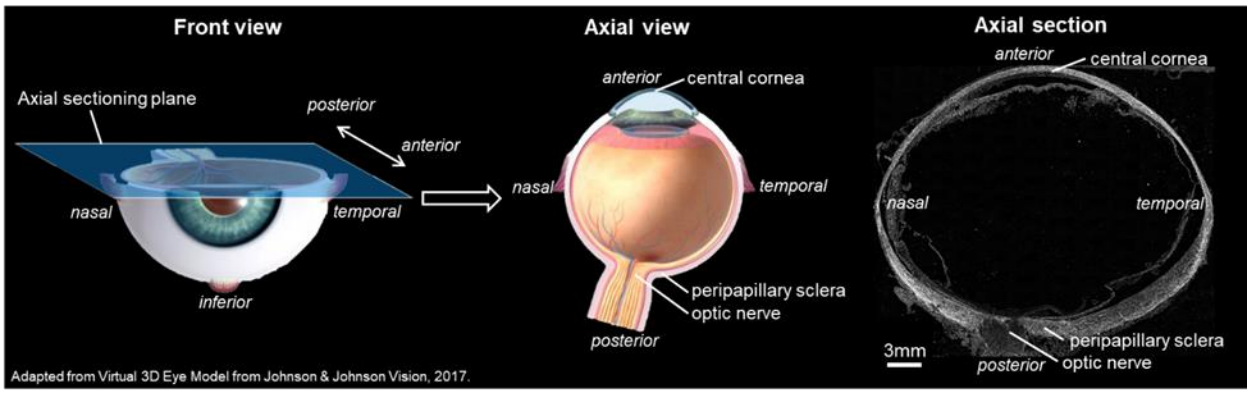

Figure 22. Location and orientation of the axial sectioning plane and example PLM image. (left and middle) 3D diagrams illustrating the location and orientation of the axial sectioning plane from which the sections analyzed in this study were collected. The axial view traverses both the central cornea and sclera, permitting direct observation of the collagen fibers. (right) Example PLM image of a sheep axial section utilized in the study, enabling investigation of fiber distribution throughout the tissue's thickness.

4.2.2 Imaging

The selected sections were imaged with polarized light microscopy (PLM) using previously reported methods (Jan, Lathrop et al. 2017) to visualize and quantify the collagen fiber orientations and density. We have shown that PLM is robust in visualizing collagen architecture and measuring localized collagen fiber orientation in eye tissue (Jan, Grimm et al. 2015, Gogola, Jan et al. 2018, Jan, Brazile et al. 2018). Briefly, the imaging system consisted of two polarized filters (Hoya, Tokyo, Japan), one a polarizer and the other an analyzer, to collect images at four filter orientations 45° apart. The relative changes in intensities at each pixel were used to determine the local collagen fiber orientation and density. The sections were imaged using an Olympus IX83 microscope with an Olympus DP74 camera and a 4x objective (1.49μm/pixel). Because the whole eye section was larger than the field of view, multiple images were captured (10% overlap) and stitched into mosaics to cover the whole section. The PLM images were processed as previously

described (Jan, Gomez et al. 2017, Jan, Lathrop et al. 2017) to obtain Cartesian orientation (Figure 23 A) and "energy" images (Figure 23 B). The Cartesian orientation images display the collagen orientation at each pixel in the section plane that ranges from 0 to 180 degrees. The "energy" image value at each pixel ranges from 0 to 1 and reflects the signal strength in each pixel that is proportional to collagen density (Jan, Grimm et al. 2015). Elsewhere, we have shown that PLM-derived measurements of the type of parameters of interest in this work are not affected by the imaging system, magnification, or mosaicking (Jan, Grimm et al. 2015).

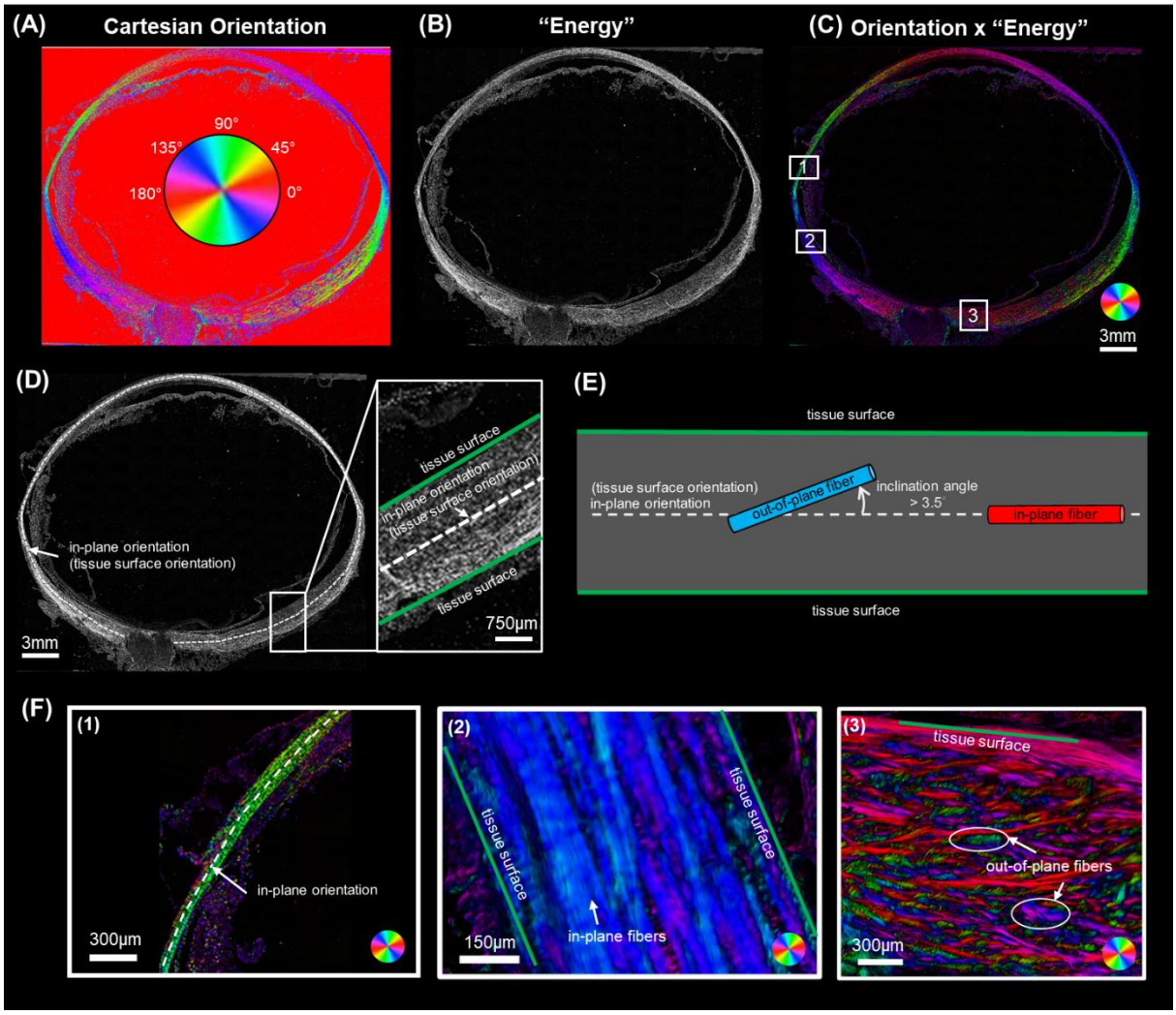

Figure 23. Example PLM images of an axial section in a sheep eye and terminology clarification.(A-C) Example PLM images of an axial section of a sheep eye. (A) Cartesian orientation image. The color at each

pixel indicates the local fiber orientation in the image plane estimated from four PLM images with different filter orientations, as per the colorscale in the center. (B) "Energy" image where pixel intensity is proportional to collagen local birefringence. Higher birefringence values indicate higher local density and fibers in the plane of the section. Please see the main text for details of how the energy is computed. (C) The combination of Cartesian orientation map and energy image helps distinguish the tissue collagen fiber architecture from the background and non-birefringent elements. (D-F) These panels are intended to clarify the terminology in this study. (D) An in-plane orientation can be defined at each location over the globe (white dashed line). In-plane orientation was determined by manually tracing a segmented line along the mid-layer, following the globe's overall curvature. This curve thus defines at each point on the shell a local orientation in-plane with the tissue. (E) Schematic diagram defining in-plane orientation, tissue surface orientation, inclination angle, out-of-plane fiber and in-plane fiber. In-plane orientation (white dash line), identical to tissue surface orientation, represents the local tissue surface's orientation. The angle between fibers and the in-plane orientation is termed the inclination angle. Fibers with an inclination angle greater than 3.5° were classified as out-of-plane fibers (blue), while those with inclination angle no more than 3.5° are classified as in-plane fibers (red). (F) Three sub-regions from the Orientation x 'Energy' image in panel C to for illustration (boxes labeled, 1, 2 and 3). Region 1 shows the sclera shell near the anterior equator with the white dashed line representing in-plane orientation. The tissues are very thin in this region. Overall, the sclera fibers are green, indicating that they are closely oriented with the tissue plane. Region 2 also contains predominantly in-plane fibers, although in this region the fibers exhibit more variations as discernible by the various tones of blue and purple. Region 3 in the posterior pole displays numerous out-of-plane fibers inclined relative to the tissue surface. These out-of-plane fibers vary in their inclination angles, from small for purple fibers, larger for red ones, and very large ones for fibers in green. Our goal in this study was to measure the inclination angles of the collagen fibers over the corneoscleral shell. The inclination angles are measured locally with respect to the in-plane orientation, and thus provide a measure of the fiber orientations in-depth and the number of out-of-plane fibers.

4.2.3 Quantification

4.2.3.1 Overview

We quantified three types of features of in-depth collagen fiber organization: orientation distribution, anisotropy, and fiber inclination. These in-depth features explore how fibers are arranged within the cross-section of the tissue's thickness, whether they mainly align parallel to the tissue surface or being interwoven/inclined relative to the tissue surface. We first studied the three features in the entire sclera (Figure 24 A), Then we divided the corneoscleral shell into 15 regions in total (Figure 24 B) to study the three features in each region.

All the manual markings in this section were done using Fiji is Just ImageJ (FIJI) (http://imagej.nih.gov/ij/; provided in the public domain by the National Institutes of Health, Bethesda, MD, USA) (Schindelin, Arganda-Carreras et al. 2012). The calculations were done in MATLAB v2022 (MathWorks, Natick, MA, USA).

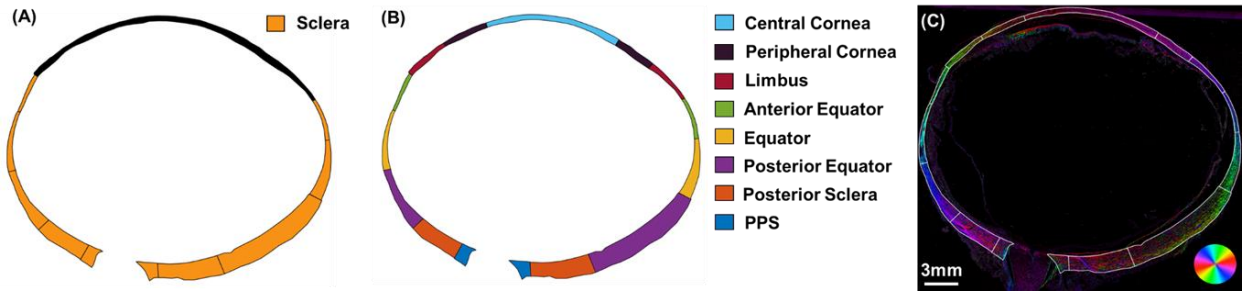

Figure 24. Schematic diagram of regions from which we characterized the in-depth collagen fiber organization.(A) Schematic diagram of an eye showing the entire sclera region, from which we characterized the in-depth collagen fiber organization. (B) To study regional variations, we divided the corneoscleral shell into 15 regions to study the features in each. The sclera region was divided into anterior equator, equator, posterior equator, posterior sclera, and PPS. Rest of the area was divided into central cornea, peripheral cornea and limbus. (C) Orientation x "energy" image of the example whole globe section, having region boundaries overlaid.

4.2.3.2 Quantification Of Orientation Distribution

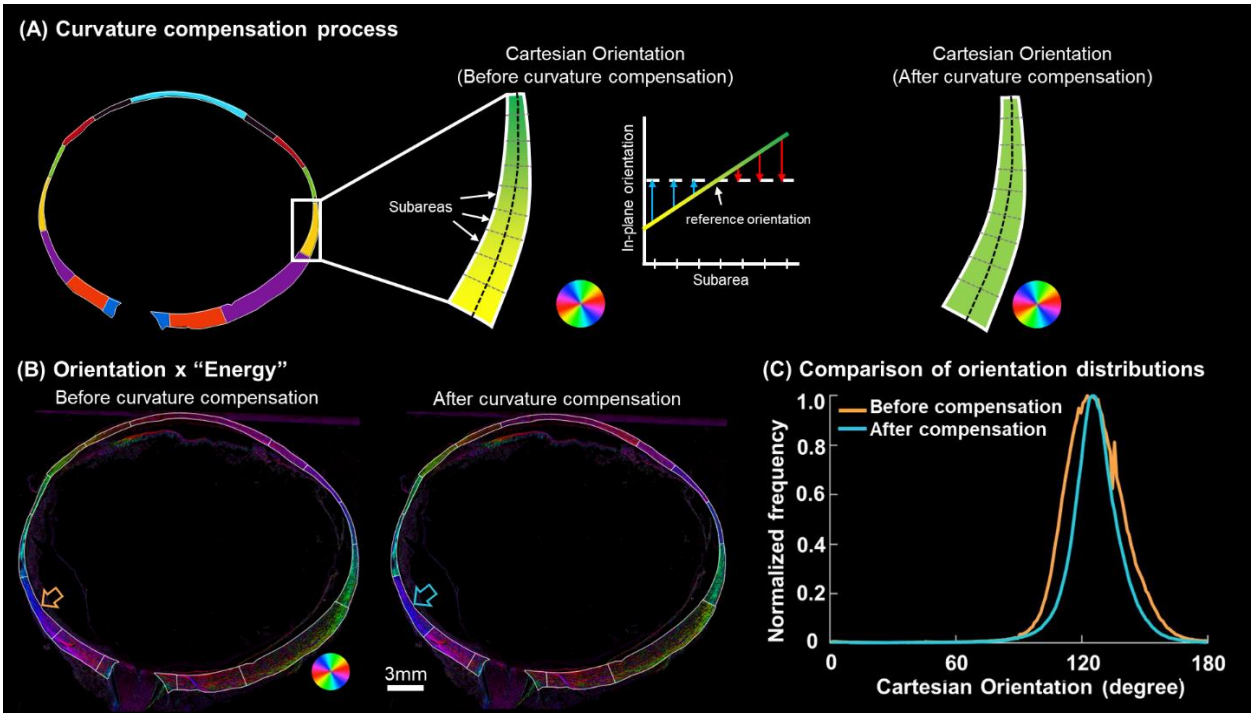

Figure 25. Curvature compensation for quantifying orientation distributions around the globe.(A) A demonstration was conducted in an equatorial region along the temporal side. Within this region, the Cartesian orientations exhibit a gradual shift from yellow to green due to tissue curvature. The in-plane orientations within subareas of this equator region were determined using the method in Figure 2D. To "flatten" this region, the Cartesian orientations of all pixels within each subarea were adjusted by subtracting the difference between their respective in-plane orientation and the reference orientation. The adjusted Cartesian orientations within each subarea appear constant. Note that the color of the Cartesian orientations is a schematic diagram and does not account for the diverse range of inclination angles present in the region. (B) Orientation x "Energy" image of an example whole globe axial section before and after curvature compensation. After curvature compensation, orientations in each region were more uniform, showing a more consistent color. (C) Comparison of the orientation distributions in an example region, the posterior equator (highlighted by the arrows in panel B), before and after curvature compensation. After curvature compensation, the orientation distribution became more concentrated with reduced variability.

To study the orientation distribution in a region, the boundary of the region was marked manually using FIJI. Cartesian orientations and "energy" values within the region were extracted from the images and processed for quantification.

To compensate for the orientation variations introduced by the corneoscleral shell curvature, first, we manually marked a segmented line along the mid-layer of the region to represent the overall curvature and orientation of the tissue surface. Each segment was designed to have a length smaller than 1% of the eyeball average radius (~11mm). Referring to the segmented line, we divided the region into small subareas, with each subarea centered on one of these line segments (Figure 25). The orientation of the tangent line at the center of the curve was selected as reference orientation. To compensate for the curvature-induced orientation variations, we adjusted the Cartesian orientations of all pixels within each subarea by subtracting the difference between their local in-plane orientation and the reference orientation. When characterizing the orientation distributions of entire sclera, we set 0 degree as reference orientation. After correction, the orientation distribution was calculated for each region and weighted by "energy". The weighting-by-energy was implemented as follows: when constructing the orientation distribution histogram, we assigned each orientation the corresponding energy value, which spans the range from 0 to 1, as its frequency value, rather than assuming all orientations have an equal frequency of 1. The weighing served several purposes. First, it ensured that the measurements are representative of the fibers in the plane of the section, eliminating potentially artefactual angles from fibers at a high angle to the section. Second, it accounted for the regional variations in collagen fiber density (Yang, Jan et al. 2018). These reduce potential measurement noise that could result from the fact that a section only exhibits smaller bits and pieces of the complex structure, by making the measurements better represent the higher quality data.

To quantify orientation distribution, we summed up n number of weighted π-periodic von Mises distributions (Gouget, Girard et al. 2012) and one uniform distribution $c(\theta)$ to fit the original orientation distribution, where $F(\theta; k, \mu, c, a) = c(\theta) + \sum_{i=1}^{n} a_i \frac{1}{\pi I_0(k_i)} \exp(k_i \cos(2(\theta - \mu_i)))$. In the equation, θ represents fiber orientation values lie in the interval [0, π]. a_i is the weighting factor associated with each von Mises distribution. μ_i is the primary orientation, the angle at the maximum of each von Mises distribution. I_0 is the modified Bessel function of the first kind of order zero. k_i is the fiber concentration factor.

To find the parameters that yield the best match with the original experimental orientation distribution, an iterative algorithm was applied (Lagarias, Reeds et al. 1998). In each iteration, we allowed for updates on the number of von Mises distributions n, the three parameters associated with each von Mises distribution (i.e., weighting factor a_i, primary orientation μ_i, fiber concentration factor k_i), and the frequency of the uniform distribution. We defined the cost function as the Euclidean distance between the original and the fitted distributions. This algorithm was terminated when one of the following three criteria was met: 1) the maximum number of the optimization iterations was larger than 100,000, 2) the tolerance on the cost function value was smaller than 1e-4, or 3) the tolerance on the parameter variation was smaller than 1e-4.

4.2.3.3 Quantification Of Anisotropy

Anisotropy was calculated to evaluate the overall degree of fiber alignment. Anisotropy ranges from 0 to 1 and is proportional to the circular standard deviation of all orientation values in a region. A high anisotropy value indicates a high degree of fiber alignment, whereas a low anisotropy value indicates low fiber alignment (Gogola, Jan et al. 2018). When calculating, we

used the Cartesian orientation values after being corrected for curvature and orientation frequencies weighted by “energy”, as described above.

4.2.3.4 Quantification Of Fiber Inclination

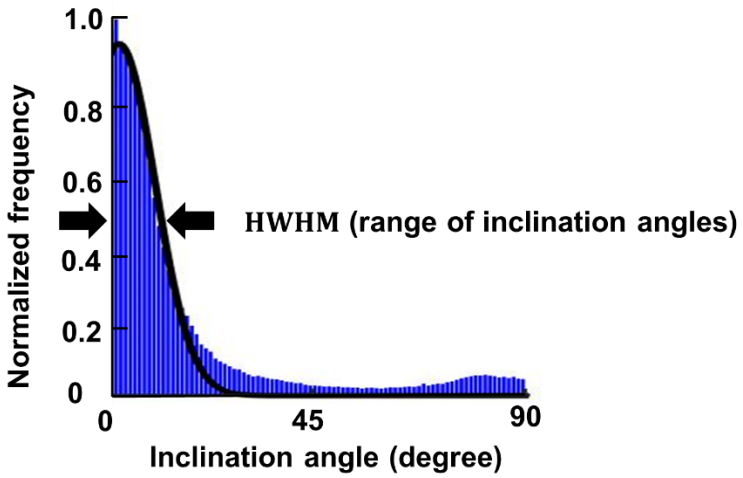

Figure 26. Fiber inclination quantification.The inclination angle distribution (blue) was fit by a half Gaussian curve (black solid line). The range of inclination angles was calculated as the half width at half maximum (HWHM) of the Gaussian distribution.

Section 4.2.3.2 described the general characterization of fiber orientation distributions. Herein we focus on measuring how fibers were oriented relative to the corneoscleral shell surface.

Similar to the process described in Section 4.2.3.2, we marked a segmented line along the mid-layer of the region following the overall curvature. The orientation of each line segment was considered as the local orientation of the tissue surface (i.e., in-plane orientation). The relative angle between a fiber and the in-plane orientation was defined as the inclination angle, which was calculated as the difference between the local in-plane orientation and the local fiber orientations obtained from the Cartesian orientation map. Inclination angles range from 0 to 90 degrees, where a 0-degree inclination angle represents that the fiber is perfectly in-plane and has no inclination

whatsoever, and a 90-degree inclination angle represents a fiber that is perpendicular to the tissue surface.

We quantified two parameters of fiber inclination: the range of inclination angles and the percentage of inclined fibers. To determine the range of inclination angles, we plotted the inclination angles as a histogram with frequencies weighted by "energy" values. A half-Gaussian curve was fit to the distribution. The half width at half maximum (HWHM) of the Gaussian distribution was quantified as the range of inclination angles (Figure 26). The range of inclination angles was designed because fibers in the corneoscleral shell can be inclined at different angles. Thus, a parameter was needed to describe the overall variation of inclination angles. The range of inclination angle ranges from 0 to 90 degrees. If the derived HWHM was greater than 90 degrees, which can happen when the distribution was more isotropic, we corrected the range of inclination angles to 90 degrees. A large range of inclination angles means that lots of fibers are inclined at large angles, whereas fibers largely parallel to the tissue surface will result in a smaller range of inclination angles. To compute a percentage of inclined fibers we defined a fiber as inclined if it had an inclination angle greater than 3.5 degrees. We recognize that choosing any specific angle to define inclined fibers is arbitrary. Nevertheless, we posit that selecting a value is useful for understanding the results. We selected the 3.5 degrees value because it corresponds with a study by Winkler et al, on fiber inclinations in the cornea, and therefore it provides a, still arbitrary, but useful level for comparison (Winkler, Shoa et al. 2013). Later work could look into how important the choice of angle was to the findings.

4.2.3.5 Statistics

We assessed variations in anisotropy, the percentage of inclined fibers, and the range of inclination angles by conducting ANOVA tests to distinguish inter-specimen and intra-specimen

differences. When deciding regional differences of anisotropy, percentage of inclined fibers and range of inclination angles, we used linear mixed effects models (LME) to account for autocorrelations between measurements from the same section and eye. We used a significant level of alpha = 0.01 to check if the three parameters were significantly different between any two regions (Gałecki and Burzykowski 2013). When evaluating the match between the fitted and original orientation distributions, we used R^2.

4.3 Results

The average anisotropy of fibers in the entire sclera across all eyes was 0.5552 with a standard deviation of 0.0552. Figure 27 shows the orientation distribution and anisotropy of an example sheep eye.

Figure 28 shows the anisotropies of all the regions on both nasal and temporal sides across all eyes. Anisotropy in the eye posterior part (i.e., PPS, posterior sclera, posterior equator on temporal side and PPS on nasal side) was lower than in other regions ($p<0.01$).

For the curve fitting, we achieved good agreements with $R^2 > 0.87$ between the fitted distribution and the original distribution for all cases. Curves were fit for each region of each eye (15 regions/eye x 7 eyes). For readability, we selected curve fitting results of two example regions, limbus and posterior equator, for an example eye (Figure 29). The curve fitting parameters of all other regions and eyes are provided in the Appendix A.

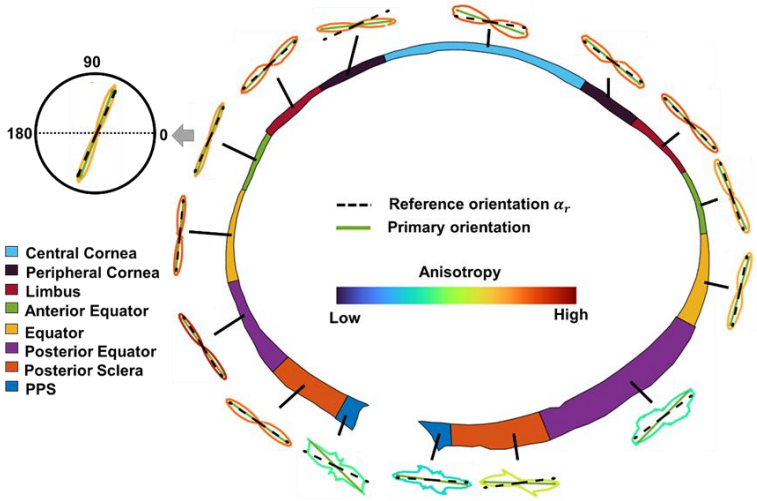

Figure 27. Orientation distributions of an example eye after curvature compensation.The distributions are shown as polar plots with the lines colored by anisotropy according to the legend in the center. The reference orientation is the in-plane orientation of each region. Primary orientation is the orientation with a maximum frequency in the distribution (the mode).

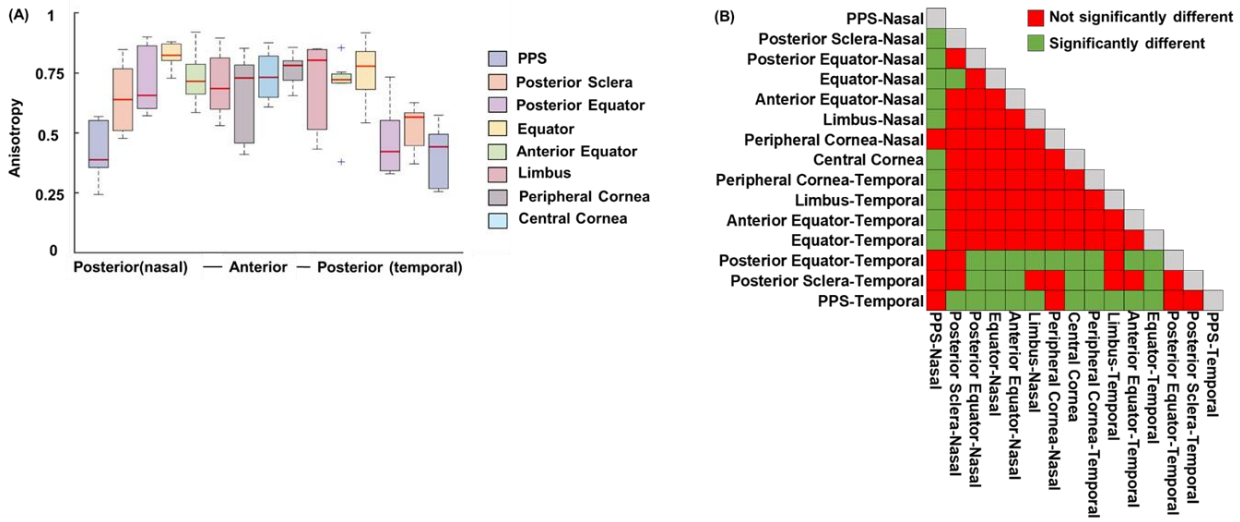

Figure 28. Fiber orientation anisotropies of all the regions on both nasal and temporal sides across all eyes. (A) Anisotropies of the 15 regions on both nasal and temporal sides across all eyes. (B) Matrix of LME tests doing pair-wise comparisons of anisotropy between all regions. PPS, posterior sclera, posterior equator on temporal side and PPS on nasal side had relatively smaller anisotropy that other regions, meaning their fibers were less aligned ($p<0.01$).

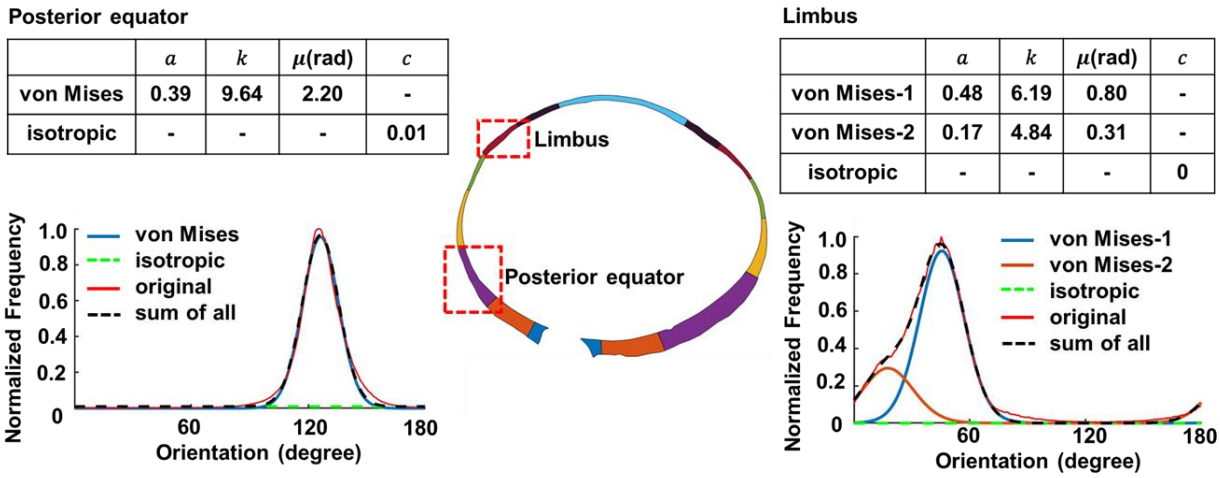

Figure 29. Quantification of the orientation distributions of two example regions, (left) a posterior equator region and (right) and a limbus region of an example eye.The optimized parameters (k, μ, c, a) are shown in the tables of each side. We found that only one von Mises distribution was needed to fit the posterior equator's orientation distribution, whereas two von Mises distributions were needed to fit the limbus's orientation distribution. In both cases, the fitted distribution (F(θ; k, μ, c, a), black dash line) matched with the original, or experimentally-measured, orientation (red line) at $R^2 > 0.87$. Note that in these plots the angles are absolute values and are therefore not relative to the main plane.

Figure 30 summarizes the number of von Mises distributions that were required to fit the orientations in each region. The posterior pole requires more distributions, suggesting that there are more collagen fiber families or groups in the posterior pole. Recall that these distributions are only accounting for the in-depth fiber distribution. The number of distributions needed for the fibers in-plane is likely different.

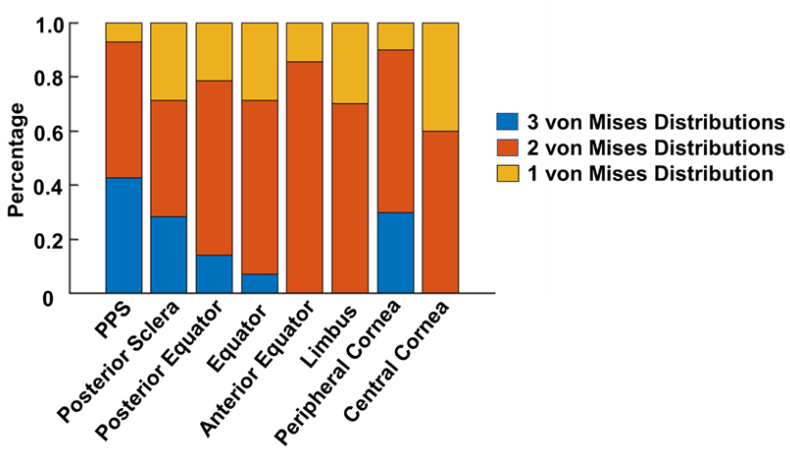

Figure 30. The number of von Mises distributions used to fit the orientation distribution of all regions of all eyes.In PPS, posterior sclera and peripheral cornea, we observed that in more than 20% of the cases, 3 von Mises distributions were needed to fit the original orientation distribution. In anterior equator, limbus and central cornea regions, only one or two von Mises distributions were needed for curve fitting.

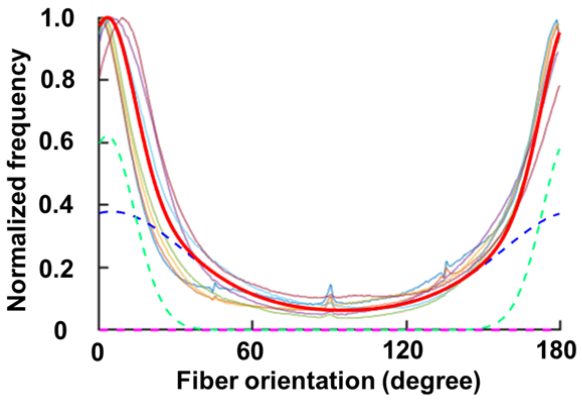

Average fitting parameters

	a	k	μ(rad)	c
von Mises-1	0.5873	0.9008	0.0924	-
von Mises-2	0.2937	7.3153	0.0605	-
isotropic	-	-	-	1.3799e-04

Figure 31. Orientation distribution in the entire sclera region.All the seven sections exhibited a similar distribution pattern, with most of the fibers aligned at 0/180-degree direction, which is in-plane and parallel to the tissue surface. We performed curve fitting for each eye. The average fitting parameters were calculated and shown in the table, with which we obtained the average fitting curve (red solid line). The average fitting curve was the combination of two weighted von Mises Distributions (blue and green dash lines) and an isotropic component (magenta dash line). The average fitting curve achieved a fitting with the original orientation distribution of each sample at $R^2 > 0.88$.

Figure 31 shows the original and fitted orientation distributions of fibers in the entire sclera region for all the sections. The original orientation distributions from all the sections exhibited similar patterns, which could be fit using two von-Mises Distributions. The isotropic component had a value of 1.3799e-04, which for practical purposes is negligible. With the averaged fitting parameters, the fitted distribution had good agreement with the corresponding experimental, or original, distributions of $R^2 > 0.88$.

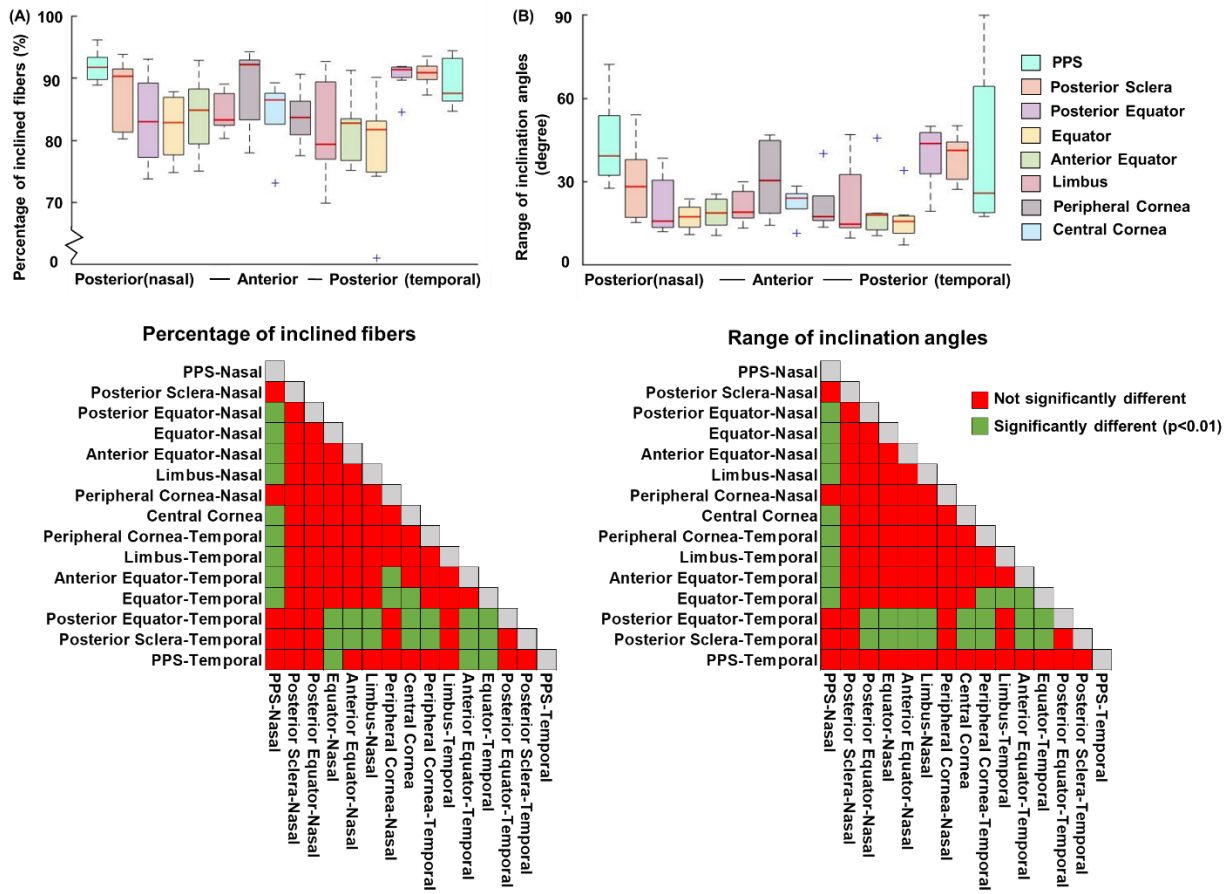

Figure 32. (A) Percentage of inclined fibers and (B) range of inclination angles.The two matrices of LME tests showed the statistical significance of pairwise comparisons of each parameter between all regions. Fiber inclination was substantial in all regions, whereby even the most aligned region had around 70% of fibers running inclined and exhibited a range of inclination angles of 7 degrees. In general, fibers in posterior sclera

and posterior equator on temporal side and PPS on nasal side had more inclined fibers ($p < 0.01$) and a larger range of inclination angles than other regions ($p < 0.01$).

Figure 32 shows the percentage of inclined fibers and range of inclination angles of all 15 regions on both nasal and temporal sides across all eyes. Posterior sclera, posterior equator on temporal side and PPS on nasal side exhibit a larger percentage of inclined fibers ($p < 0.01$) and a larger range of inclination angles ($p < 0.01$).

We found significant inter-specimen variation in the percentage of inclination angle, indicating differences between eyes ($p<0.05$). In contrast, intra-specimen variation within sections of the same eye was not significant for this parameter. Additionally, we did not observe significant variations, either inter-specimen or intra-specimen, in the range of inclination angle or anisotropy.

4.4 Discussion

We performed a systematic quantification of in-depth collagen fiber organization over the corneoscleral shell of sheep eyes. Specifically, we quantified orientation distribution, anisotropy, and fiber inclination with respect to the local plane, in 15 regions around the eye globe and in entire sclera. The following main results arise from this work: Over the globe, there were fibers with all in-depth orientations, with varying degrees of in-depth anisotropy. While many fibers had orientations close to the tissue plane, fiber inclinations were substantial in all regions. The percentage of inclined fibers and the range of inclination angles were larger in the posterior globe, particularly on the temporal side. Below we discuss these results in more detail.

Over the globe there were fibers oriented with all in-depth orientations, with varying degrees of in-depth anisotropy. Compared between regions, the fibers were less aligned in-depth in the nasal PPS, temporal PPS, posterior sclera and posterior equator. Our observations mean that the actual in-depth collagen organization is more complicated than the commonly assumed thin shell structure with primarily in-plane aligned fibers (Arciniegas and Amaya 1986, Watson and Young 2004, Kimpton, Walker et al. 2021). Our results suggest that many studies of eye structure and biomechanics, from our lab (Voorhees, Jan et al. 2017, Voorhees, Jan et al. 2017) and others (Girard, Dahlmann-Noor et al. 2011, Grytz, Meschke et al. 2011, Pijanka, Coudrillier et al. 2012, Coudrillier, Boote et al. 2013, Grytz, Fazio et al. 2014, Coudrillier, Pijanka et al. 2015, Zhang, Albon et al. 2015, Coudrillier, Campbell et al. 2016, Kollech, Ayyalasomayajula et al. 2019, Grytz, Krishnan et al. 2020), have substantially underestimated the in-depth variations. It is unclear the consequences. It seems plausible that assuming that all the fibers are in-plane may simultaneously overestimate the in-plane stiffness and underestimate the out-of-plane stiffness of the tissue. Collagen fiber organization is a main factor determining the eye tissue mechanical behaviors (Spoerl, Boehm et al. 2005, Girard, Downs et al. 2009, Pijanka, Coudrillier et al. 2012, Coudrillier, Boote et al. 2013, Fung 2013). Having accurate quantitative information about how fibers are organized is thus important. Our intent with this work is to provide the information on in-depth variation that can be incorporated in 3D modeling to improve the predictions of tissue mechanics.

We employed semi-circular von Mises distribution functions to quantify the fiber orientation distributions. These functions capture the distribution of fiber orientations about a preferred orientation and are widely used to describe the unimodal planar organization of fibers (Gouget, Girard et al. 2012). Through our analysis, we found that the in-depth orientation distribution is better described by more than one family of fibers with different primary

orientations and fiber concentration factors. Specifically in sclera, we found two groups of fibers that fit different von Mises distributions. To the best of our knowledge, the studies using the von Mises distributions for fiber orientations have only applied them to the in-plane distribution of fibers. (Girard, Downs et al. 2009, Feola, Myers et al. 2016, Schwaner, Hannon et al. 2020, Schwaner, Perry et al. 2020). Although our results suggest that assuming fully in-plane fibers is inaccurate, conveniently our results also suggest that the in-depth orientation of the fibers can be well-characterized by between one and three von Mises distributions. Since these functions have already been implemented in several software packages, as demonstrated by publications using them cited above, we trust that using them for the in-depth distribution will not be a major obstacle.

We observed substantial fiber inclination across the entire corneoscleral shell. The effects of fiber inclination has been studied in cornea and was found to have critical biomechanical roles. In this study the authors speculate that inclined fibers can introduce more connections between adjacent fibers, which are likely to prevent fiber slippage, stabilize the cornea shape, and increase cornea stiffness (Petsche, Chernyak et al. 2012, Petsche and Pinsky 2013, Winkler, Shoa et al. 2013). In ocular tissues, fiber inclination can also be associated with fiber interweaving. Elsewhere we have shown that interweaving can impact the structural mechanical behavior of sclera (Wang, Hua et al. 2020).

To our knowledge, fiber inclination had not been systematically characterized in sclera. The role of fiber inclination in sclera biomechanics is also not clear. One possibility is that fiber inclination may play a similar role as it does in cornea, where more fiber inclination could stabilize sclera structure and increase sclera stiffness. While we have drawn parallels between fiber inclination in the cornea and sclera, we acknowledge the compositional and ultrastructural distinctions between these ocular tissues. These distinctions encompass variations such as collagen

fibril characteristics, microfibril orientations, tissue hydration levels, and elastic fiber content (Boote, Hayes et al. 2006, Bell, Hayes et al. 2018). It is important to recognize these differences in understanding the specific role of fiber inclination in scleral biomechanics. It is also possible that fiber inclination in sclera has an opposite effect as it does in cornea, where more fiber inclination means the sclera contains more interweaving fibers, thus being less stiff and more susceptible to IOP changes (Wang, Hua et al. 2020). If the second hypothesis is true, our observation potentially could explain why in early glaucoma, neural tissue loss occurs predominantly in the inferior-temporal and superior-temporal sides (Kiumehr, Park et al. 2012, Lisboa, Leite et al. 2012), since we observed a larger percentage of inclined fibers and a larger range of inclination angles in posterior part of the eye especially on the temporal side. Future studies should evaluate the role of fiber inclination.

It is worth mentioning that fiber inclination is different from fiber crimp (Jan, Brazile et al. 2018). Crimp is a natural waviness within Type I collagen fibers, whereas fiber inclination is at a larger scale, focusing on measuring the orientation of the macroscale fibers relative to the tissue surface. The eyes that we analyzed were pressurized and fixed at 50 mmHg after most of the fibers have been recruited and the crimp is no longer present (Jan and Sigal 2018). Therefore, we believe the results from this study were not impacted by the variations caused by the crimp.

Our measurements took place across the entire thickness and ignored depth-dependent features. It is possible that the orientation distribution, anisotropy and fiber inclination vary from the episcleral surface to the inner surface of the corneoscleral shell. Depth-dependent features of collagen fiber organization can be functionally important. For example in human sclera, fibers were found organized in a more highly aligned pattern near the episcleral surface compared with

inner surface (Yan, McPheeters et al. 2011, Pijanka, Coudrillier et al. 2012, Pijanka, Spang et al. 2015, Jan, Lathrop et al. 2017, Gogola, Jan et al. 2018).

We acknowledge a potential concern regarding overparameterization when determining the number of von Mises distributions for fitting the original orientation distribution. To address this, we conducted a manual validation process once the algorithm determined the optimal number of distributions. Our observations consistently showed that removing one distribution significantly worsened the fit, suggesting the model's reduced ability to capture the data. Conversely, adding an extra distribution often maintained a similar fit quality, although there were instances where additional distributions did not improve the fit or even made it worse. While our approach was effective, we recognize room for future refinements. Future research may explore formalized criteria to address overparameterization for a more robust analysis of orientation distribution in complex tissue structures.

When interpreting the findings in this work is important to consider the limitations. First, we studied only sheep eyes. Sheep eyes are similar to human eyes. But they are larger and less symmetric than the human eye, with different axial lengths, equatorial diameters, and more variable tissue thicknesses in the corneoscleral shell (El-Maghraby, Nyland et al. 1995, Voorhees, Ho et al. 2017). Though it is possible that our characterization found in sheep are not the same in human, it is important to understand sheep as an animal model (Gerometta, Spiga et al. 2010, Candia, Gerometta et al. 2014). Future work should include additional animal models as well as human eyes. Additionally, the sample size in our study was limited to seven sections obtained from three sheep eyes. This constraint was primarily due to the availability of suitable specimens. A larger sample size could have enhanced the statistical power of our analysis, increasing the

likelihood of detecting significant differences or relationships. In future work, it is advisable to consider an expanded sample size, which would improve the generalizability of our findings.

Second, when evaluating the range of inclination angles, we choose to use Gaussian functions to fit the distribution of inclination angles. This is because the distribution of inclination angles was found to follow a normal distribution in more than 95% of the cases. In some regions the distributions of inclination angles were more complicated. In those cases, the HWHM is greater than 90 degrees. We corrected those values to 90 degrees, meaning that the variation of inclination angles could span the whole range. We aim to describe the overall variations of inclination angles in most cases. Future if more accurate quantification is necessary, we could introduce more complex definitions to better fit and describe those exceptional cases.

Third, the tissue sections were of 30μm thickness. The images used for this study provided a measure of the dominant fiber orientation in each pixel (Jan, Grimm et al. 2015). Especially in complex regions, it is possible that at through the depth of the section the fiber orientation distribution is not constant.

It is worth considering this point when interpreting the observation from this study. In the future, analyzing thinner sections could be useful to reduce the influence of fiber overlapping. The images were acquired from histologically processed tissue, which may have introduced artifacts such as tissue shrinkage or distortion from the fixation and sectioning. We have shown the influence of such artifacts is minimal (Tran, Jan et al. 2017).

In conclusion, we reported the first systematic experimental characterization of in-depth collagen fiber organization over the corneoscleral shell. Specifically, we have quantified orientation distribution, anisotropy, and the two parameters of fiber inclination (i.e., percentage of inclined fibers and range of inclination angles). The results from this study will contribute to a

better understanding of the collagen fiber in-depth organization of ocular tissue, developing more accurate fiber-based microstructure models of the eye, and understanding the role of collagen microstructure in eye biomechanics.

5.0 Introduction Of Direct Fiber Modeling Approach For Simulating Sclera Collagen Architecture And Biomechanics

The content of this chapter has been published by Experimental Eye Research (Ji, Bansal et al. 2023).

5.1 Introduction

Collagen fibers are the principal load-bearing component of sclera (Girard, Downs et al. 2009, Pijanka, Coudrillier et al. 2012, Grytz, Fazio et al. 2014, Jan, Gomez et al. 2017, Boote, Sigal et al. 2020), and thus play an important role on eye physiology and pathology (Ethier, Johnson et al. 2004, Summers Rada, Shelton et al. 2006, Coudrillier, Tian et al. 2012, Pijanka, Coudrillier et al. 2012). This has motivated many studies aimed at understanding the role of sclera collagen microarchitecture on macroscale eye biomechanical behavior (Girard, Downs et al. 2009, Grytz, Meschke et al. 2011, Coudrillier, Boote et al. 2013).

Because of the complexity of sclera microstructure and the difficulty of accessing it directly for experimentation, numerical models have been widely developed and used for the studies (Sigal, Flanagan et al. 2004, Girard, Downs et al. 2009, Girard, Downs et al. 2009, Grytz, Meschke et al. 2011, Coudrillier, Boote et al. 2013, Coudrillier, Pijanka et al. 2015, Voorhees, Jan et al. 2017, Voorhees, Jan et al. 2018, Hua, Voorhees et al. 2020). Most models have been formulated within a continuum mechanics framework in which collagen fiber architecture has been approximated using statistical distributions, often with the parameters derived from inverse fitting. The

conventional continuum approach, while helpful to describe the sclera macroscale behavior, does not account for potentially crucial tissue characteristics such as fiber interweaving, fiber-fiber interactions and the in-depth fiber orientation distributions (Jan, Lathrop et al. 2017, Boote, Sigal et al. 2020, Lee, Yang et al. 2022). Thus, the conventional approach is limited in the ability to capture sclera structure and mechanics at fiber-level scale. This is problematic because accurate predictions at the small scale are crucial if the intent is to use the models to understand effects at the scale of cells, axons and for studying mechanobiology. Further, ignoring interweaving and fiber-fiber interactions can introduce substantial errors when estimating sclera fiber mechanical properties using inverse fitting (Wang et al., 2020).

To address the limitations of conventional models and better account for microstructure, models have been developed that explicitly incorporate collagen fiber networks (Hadi and Barocas 2013, Zhang, Lake et al. 2013, Licup, Münster et al. 2015, Islam and Picu 2018, Picu, Deogekar et al. 2018). The models, however, are limited in their ability to represent specimen-specific collagen architecture. In addition, the models were formed by short fibers, sometimes generated stochastically, and do not represent well the long fibers that form the sclera (Boote, Sigal et al. 2020). Long fibers can, potentially, have fundamentally different mechanical behavior than short fibers (Voorhees, Jan et al. 2018), and thus that explicitly accounting for them is important in specimen-specific modeling of the eye. Altogether, the limitations of the current modeling tools highlight the need to develop more advanced modeling techniques that can incorporate detailed information on fibers.

Our goal was to demonstrate that it is possible to build a model of sclera that represents fiber microstructure better than the conventional modeling approaches and that also captures sclera macroscale behavior. In this manuscript we introduce a new modeling approach, that we call direct

fiber modeling, in which the collagen architecture is accounted for by long, continuous, interwoven fibers. The fibers are embedded in a continuum matrix representing the non-fibrous tissue components. We demonstrate the methodology by modeling a rectangular patch of posterior pole sclera. First, we show that a specimen-specific direct fiber computational model can be built based on high resolution polarized light microscopy data of cryosections from pig and sheep. We show that the fiber orientation distributions of the direct fiber model can be made to follow closely those of the cryosections simultaneously in both the coronal and sagittal planes. This is a more demanding requirement than in conventional models in which only the fiber orientations in coronal plane are accounted for (Girard, Downs et al. 2009). Second, we used the model in an inverse modeling approach by fitting experimental biaxial stress-strain data from the literature. We show that the direct fiber model can match the experiment simultaneously in both radial and circumferential directions. Overall, direct fiber modeling can provide unique insight into the interplay between tissue architecture and behavior and help answer questions that have been inaccessible with the conventional continuum approach.

5.2 Methods

This section is organized in three parts following the same general order as the process for building and using a direct fiber model. First, experimental data on sclera fibers and orientations were obtained using established polarized light microscopy (PLM) imaging of histological cryosections (Jan, Grimm et al. 2015). Second, a direct fiber finite element model of a patch of posterior sclera was built based on the PLM-derived orientation data. The fiber architecture of the model was first built from the collagen fiber orientation data in the coronal sections, and then

iteratively optimized to also match the orientation data from sagittal sections. The direct fiber model was then embedded in a matrix representing non-collagenous components. Third, the combined fiber and matrix model was used in an inverse fitting optimization process to match the models' simulated stress-strain behaviors with equi-biaxial test data from the literature (Eilaghi, Flanagan et al. 2010). This process produced estimates of the fiber mechanical properties. Below we describe these parts in detail.

Modeling was done in Abaqus 2020X (Dassault Systemes Simulia Corp., Providence, RI, 171 USA). Customized code and the GIBBON toolbox (Moerman 2018) for MATLAB v2020 (MathWorks, Natick, MA, USA) were used for model pre/post-processing and inverse modeling.

5.2.1 Histology, Polarized Light Microscopy And Fiber Orientation Quantifications

The study was conducted in accordance with the tenets of the Declaration of Helsinki and the Association of Research in Vision and Ophthalmology's statement for the use of animals in ophthalmic and vision research. For the fiber orientation distribution in the coronal plane, we used a porcine eye that was also part of a previous study on sclera architecture (Gogola, Jan et al. 2018). Details of the eye preparation, histological processing, PLM imaging and post-processing methods are reported elsewhere (Jan, Grimm et al. 2015, Jan, Lathrop et al. 2017). Briefly, a healthy eye without known abnormalities was obtained from the local abattoir and processed within 24 hours of death. The episcleral tissues, fat and muscles were carefully removed, and the globe was perfusion and immersion fixed in 10% formalin for 24 hours at an IOP of 0 mmHg. After fixation, the optic nerve head region was isolated with an 11 mm circular trephine and serially cryo-sectioned coronally with a slice thickness of 30 μm (Figure 33 A). Seventeen serial sections were

imaged with PLM using the 0.8× objective (NA 0.12) of an Olympus SZX16 microscope, paired with a dual chip Olympus DP80 camera (4.25 μm/pixel).

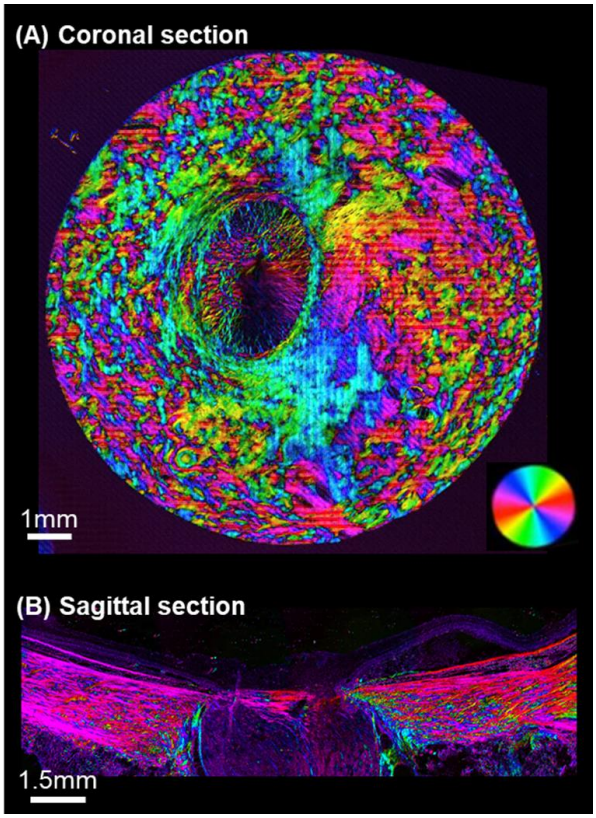

Figure 33. PLM images of coronal and sagittal sections.(A) Example PLM image of a coronal section of a pig eye through the lamina cribrosa. (B) Example PLM image of a sagittal section of a sheep eye through the optic nerve head (ONH). The colors indicate the local fiber orientation in the section plane, and the brightness the "energy" parameter (see main text).

For the fiber orientation distribution in the sagittal plane, we used a healthy sheep eye that was processed in the same way, except that the optic nerve head was sectioned sagittally. Naturally, it is impossible to section the coronal section sample again to obtain the information on in-depth sagittal orientations. Thus, we had to use a different sample. Three sections passing through the posterior temporal sclera and the middle of the scleral canal were selected and imaged with PLM using an Olympus IX83 microscope with 4x objective (1.49μm/pixel). The higher resolution in

this orientation was selected to resolve better the in-depth fiber interweaving. Fiber orientation distributions were normalized for use, and therefore we do not expect this to affect the reconstructions. Please see the discussion for a discussion of the potential consequences of having used different species for the coronal and sagittal planes.

PLM images were processed to derive at each pixel the in-plane collagen orientation (in Cartesian coordinates) and a parameter which we have previously referred to as "energy" (Yang, Jan et al. 2018). Energy helps identify regions without collagen, such as outside of the section, and regions where the collagen fibers are primarily aligned out of the section plane, so that they can be accounted for in the orientation distribution.

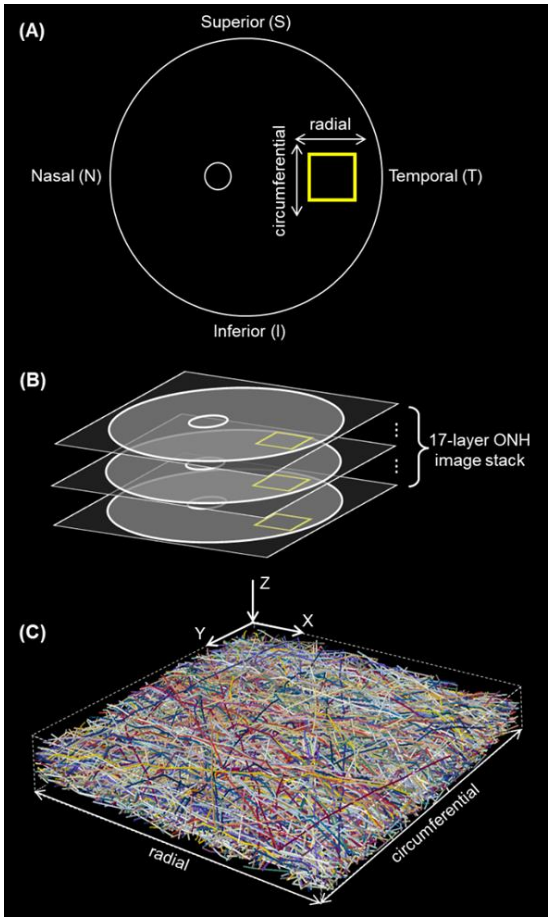

Figure 34. Visual representation of the scleral region and the process of modeling and extracting fiber orientation data.(A) Schematic coronal view illustrating the location of the scleral region modeled (yellow

box, 2.00 x 1.91 mm). The region was located at the temporal sector. Also shown are the radial and circumferential directions, which correspond with the directions used for the equi-biaxial testing in the experiment and simulation. (B) A set of 17 coronal sections were stacked and registered. Fiber orientation data was extracted from the selected rectangular patch of sclera region (yellow box in panels A and B) in the image stack and used to build the direct fiber model (C). Fibers, or fiber bundles, are shown in random colors to simplify discerning the complex interwoven architecture.

For the coronal fiber orientation, the coronal sections were stacked sequentially and registered (Gogola, Jan et al. 2018). After registration, the PLM data was reprocessed to align orientation values (Gogola, Jan et al. 2018). As target to build the direct fiber model we selected a rectangular block of sclera, 2.00 x 1.91 mm in size, in the temporal side of the optic nerve head (Figure 34). The location and shape were chosen to match the sample tested experimentally (Eilaghi, Flanagan et al. 2010). We then calculated the distribution of collagen fiber orientations from the PLM images. We used the pixel-level data from 17 sections, weighted by the local "energy". This allowed us to build the in-plane distribution based on fibers in the same plane (Yang, Jan et al. 2018).

For the sagittal fiber orientations distributions, we sampled sections through the posterior temporal sclera where the coronal information was obtained. However, instead of selecting one region and section for sampling, we reasoned that it was better to obtain a sagittal fiber orientation distribution that was more broadly representative of the region. This would help ensure good correspondence with the orientation distribution in the coronal orientation, and it would account for potential variations between eyes and misalignment between regions. To obtain the representative distribution, we measured the orientation distribution in 236 regions of three sagittal sections. All of these measurements were in regions 715 μm x 715 μm in size, and close to the

location from where the coronal sample was obtained. In each of those regions, the orientation distributions were calculated by using the out-of-plane information derived from the energy parameter to restrict the measurements to be on sagittal plane (Yang, Jan et al. 2018). We then computed the average orientation distribution over all these. We also calculated the sagittal fiber anisotropy from the median of the anisotropies among the 236 areas. The anisotropy indicates the degree of fiber alignment and was quantified as circular standard deviation (Gogola, Jan et al. 2018). Perfectly aligned fibers have an anisotropy of 1 and evenly dispersed fibers have an anisotropy of 0. We reasoned that the average distribution and median anisotropy provide a better representation of the orientation distribution in this direction than any single distribution.

5.2.2 Direct Fiber Model Construction

5.2.2.1 Fibers

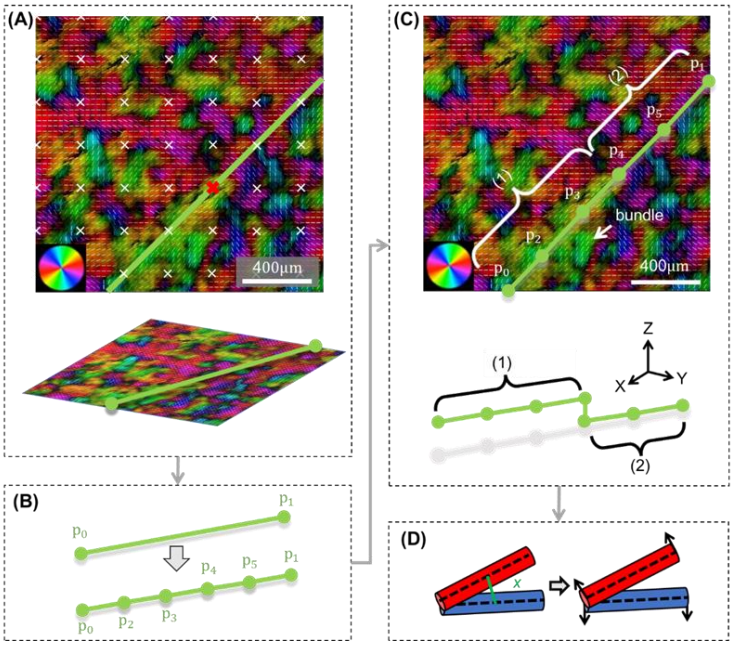

Figure 35. Workflow for creating and processing fibers.(A) The process begins with the pixel-level data from the coronal section PLM process (both orientation and energy). For clarity here we illustrate the process with

a small square region. The colors of the PLM image represent the local collagen orientation. To help discerning orientations the images are shown with overlaid short white line segments representing the mean orientation over a small square region. (top panel) A regular grid of "seed" points was defined (white x marks). At these seed points the local fiber orientation was sampled, averaged as per the white lines to avoid noise. The energy information was used to skip defining fibers in regions without a reliable well-defined orientation, and to give preference to the in-plane fiber orientations over the out-of-plane ones. The in-plane orientation was then used to define a straight fiber in the image plane. In the example case, a fiber was traced at the grid point (red x mark) at an angle around 45 degrees. The bottom panel shows an isometric view of the image with the fiber overlaid. (B) (top) The fiber was initially defined by one element and two nodes, p_0 and p_1. (bottom) The fiber was then refined into five elements and six nodes. (C) The average orientations over the fiber elements were then computed and compared with local image orientations to determine their agreement element by element. In the example shown, the element group (1), p_0-p_2, p_2-p_3, p_3-p_4, agreed well with the direction of a yellow-green bundle. Accordingly, the group was accepted at this section. In contrast, the element group (2) p_4-p_5, p_5-p_1, had poor agreement between element and image orientations. This group was then assigned a lower depth, effectively "pushing" the group or fiber segment to the depth of another section. Fiber connectivity was ensured by adding an element to connect the two element groups ((1) and (2)) at different depths. The fiber smoothness was restored when resolving fiber collisions. Meanwhile, elements were combined or split to maintain all element lengths within a pre-defined range. (D) Elements were moved apart if the shortest distance x between them was smaller than fiber diameter, indicating a collision.

Fibers were simulated using 3-dimensional linear truss elements (T3D2 in Abaqus). Fiber locations were defined by Cartesian coordinates (X, Y, Z) of element nodes. To define fibers, we sampled orientation values from PLM images at regularly spaced "seed" points with a spacing of 272 μm. At each seed point, a straight fiber 8.5 μm in diameter was traced in the section plane at an angle equal to the orientation at the seed point, meanwhile, the fiber passed through the seed point and extended the full span of the region. The process was applied for each layer, and then the fibers were stacked, resulting in a stack of 2D layers of fibers, each with a large number of

fibers crossing or “interpenetrating”. To resolve fiber interpenetrations, an algorithm was used to refine and displace fiber elements in the whole structure (Matuschke, Ginsburger et al. 2019, Matuschke, Amunts et al. 2021). Briefly, if the smallest distance between two elements was less than the fiber diameter, an interpenetration was detected. Interpenetrated elements were shifted apart iteratively until all interpenetrations were resolved. During the process, fiber elements were re-meshed so that the element length was kept between 25.5μm to 51μm. Fibers were smoothed by controlling the fiber minimum radius of curvature.

It is important to make a few important notes regarding our use of the term “fiber”. The collagen of the sclera has a complex hierarchical structure even more complex than that of the cornea and tendon (Jan, Brazile et al. 2018, Boote, Sigal et al. 2020). The models were reconstructed using a fiber diameter of 8.5 μm, which means that what we refer to as a fiber most likely represents a group of fibers that elsewhere may instead be described as a fiber bundle. Nevertheless, because our intent with this work is to call attention to the power of incorporating detailed microstructural information on sclera, we decided to use the term fiber, while also being careful to acknowledge at several critical points that these may be understood as fiber bundles. This is further addressed in the discussion.

To evaluate the similarity of the model and the images in the coronal plane, we quantified the model’s coronal orientation distribution and compared it with the distribution of the PLM images. We counted the occurrences of element orientations, where the orientation of an element was the slope angle in the coronal section plane and the number of occurrences was estimated as the element volume. This allowed us to account for uneven element sizes and to properly compare with PLM pixel-based measurements.

To better account for the fiber distribution in 3D, including the through-depth fiber undulations, we did the following: we shifted the fiber elements locally in-depth according to the fiber relative positions observed in coronal section images. If a fiber element had an orientation that disagreed with the orientation in the image by more than 45 degrees, the element was "shifted" in the posterior direction. A fiber segment that was in agreement with the local orientation was kept at the original sclera depth. After applying this process throughout the volume, we did another iteration resolving fiber interpenetrations. We then compared the in-depth fiber anisotropy of the model with the representative anisotropy in the sagittal plane. If the model had a larger in-depth anisotropy than the images, we shifted the fibers, increasing the fiber undulation amplitudes and decreasing the degree of fiber alignment. Conversely, if the model had a lower anisotropy than the sagittal images, we decreased the amplitude of fiber undulations. Each of these steps was followed by an iteration resolving fiber interpenetrations and a check in the agreement between the model and sample anisotropies in the coronal plane. Adjusted R-square (adjusted R^2) values were used to evaluate the fitness of orientation distributions. This process converged to a set of continuous fibers in excellent agreement with the PLM-derived orientations simultaneously in both coronal and sagittal planes. Adjusted R^2 is similar to the conventional R^2 in that it indicates fit to a curve, but it adjusts for the number of points considered, avoiding potentially misleading excellent fits that are the result of many points of comparison (Miles 2005).

5.2.2.2 Matrix

The model used for inverse fitting consisted of the direct fiber model and a coincident matrix with an overall dimension of 2.00 x 1.91 x 0.35 mm. The model of fibers and matrix had the same dimensions, and fiber end-nodes resided on the matrix surfaces.

5.2.3 Model Inverse Fitting

5.2.3.1 Meshing And Material Properties

Fibers were modeled as a hyperelastic Mooney-Rivlin material (Holzapfel 2001):$W = C_{10}(I_1 - 3) + C_{01}(I_2 - 3) + \frac{1}{2}K(J-1)^2$, where W was the strain energy density, C_{10} and C_{01} were the material constants, restricted by C_{10} + C_{01} > 0 and would be determined by inverse modeling, I_1 and I_2 were the first and second invariants of the right Cauchy-Green deformation tension, K was the bulk modulus and J was the determinant of the deformation gradient.

Fibers were simulated using 3-dimensional linear truss elements (T3D2 in Abaqus). A mesh convergence analysis was performed to verify that both the fiber and matrix models were sufficiently refined. The results shown were obtained with fiber element lengths between 25.5μm to 51μm, resulting in element aspect ratios from 3 to 6. This is consistent with a previous study on fiber mechanics in which we found that aspect ratios of 5 were optimal (Islam and Picu 2018). The matrix was meshed with linear eight-nodded, hybrid hexahedral elements (C3D8H in Abaqus) and modeled as a neo-Hookean material with a shear modulus of 200 kPa (Girard, Downs et al. 2009, Coudrillier, Pijanka et al. 2015). The element size of the matrix was 0.0887mm.

5.2.3.2 Interactions

Fiber-fiber interactions were simulated by preventing fiber interpenetrations using Abaqus' general contact with no friction. Preventing fiber interpenetration is computationally expensive and therefore commercial implementations are often directed at maintaining small interpenetrations rather than avoiding them altogether. We reasoned that a small interpenetration, in low single digits percent of fiber diameter, will likely not represent a major deviation from fiber

physical behavior. We calculated the extent of the interpenetration in the following way: we defined a deformed model based on the original model and the final nodal displacements. A customized MATLAB program was then used to find all existing interpenetrated element pairs. For each of these pairs, we quantified the percentage of interpenetration as $\frac{d-x_{min}}{d}$, where d was fiber diameter, and x_{min} was the minimum distance between two elements. Interpenetration thus varied between 0 when there is no interpenetration and 1 when two elements are perfectly overlapping. We found that 99.4% of the interpenetrations were smaller than 5%. This is further addressed in the discussion.

Fiber-matrix interactions were ignored, as is usual in biomechanical models of the eyes (Grytz and Meschke 2009, Petsche and Pinsky 2013, Grytz, Fazio et al. 2014).

5.2.3.3 Finite Element Analysis Procedure

The fiber-matrix assembly was subjected to a quasi-static process of equi-biaxial stretch to match the experimental results and boundary conditions reported elsewhere (Eilaghi, Flanagan et al. 2010). The matrix was simulated using Abaqus standard implicit procedure. Due to the presence of complicated fiber contacts, the direct fiber model was simulated using Abaqus dynamic explicit procedure, meant to improve the convergence and computational efficiency. The model fiber volume fraction (VF) is 7%. The resulting stresses σ along radial and circumferential directions were contributed by both matrix and fibers and calculated as $\sigma = (1 - \mathrm{VF})\sigma_{\mathrm{matrix}} + \sigma_{\mathrm{fibers}}$, where the matrix stress was weighted by fiber VF.

Because the process was quasi-static, the dynamic explicit procedure would require an excessive number of small-time increments, which is computationally impractical. Therefore, to run the dynamic analysis efficiently, mass scaling was implemented. We achieved a 1e-5 stable

time increment, where we modeled the process in the shortest time period in which inertial forces remain insignificant. During the simulation, we assured that the inertial effects were negligible by keeping the kinetic energy less than 5% of the internal energy.

5.2.3.4 Boundary Conditions And Inverse Modeling Procedure

The model was simulated iteratively to derive fiber material properties (C_{10} and C_{01}) by inversely matching published experimental stress-strain data (Eilaghi, Flanagan et al. 2010).

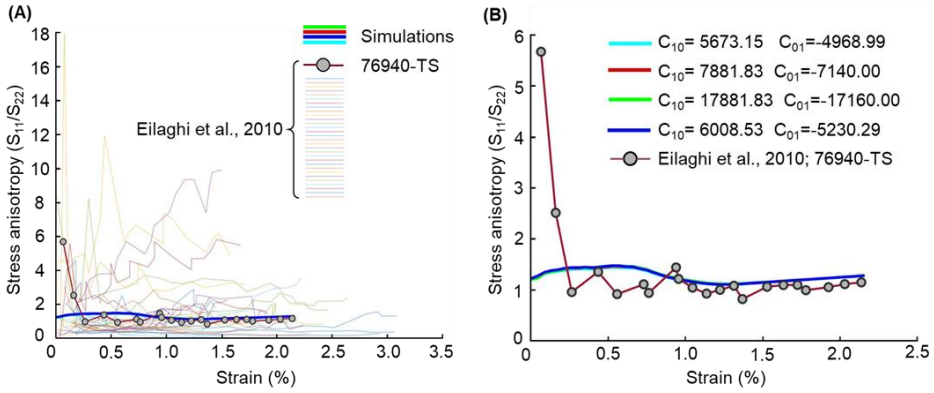

Figure 36. Analysis of fitting a model to an experimental curve by selecting a set of curves with similar anisotropy.(A) To properly fit the model to an experimental curve it was necessary to select out of all the experimental curves the set with a similar anisotropy. See text for more details. To do this we first assigned four sets of random material parameters, C_{10} and C_{01}, to the fiber model. The intent was to generate a set of model behaviors spanning the range of anisotropies to be expected over a wide range of material properties. Equi-biaxial stretch was applied to the fiber-matrix assembly and the stress anisotropy (S_{11}/S_{22}) of the model computed at many steps through the stretching process. We then also computed the stress anisotropy of the experimental curves reported by Eilaghi et al. There were substantial variations in their anisotropies. Out of all of the curves we selected 76940-TS because it had the closest agreement with the model anisotropy. The plot shows all experimental curves with 76940-TS highlighted. There was good agreement in anisotropy after about 0.25% strain. At smaller strains the experiment observed higher anisotropy, potentially due to the challenge of balancing the initial loads in the clamping when using rakes. (B) In this plot only the four models and the selected experimental curve. All C_{10} and C_{01} values are in MPa. The results revealed that the model

stress anisotropy was essentially independent of the fiber material properties. This can be discerned from the observation that the lines representing the four simulations are almost indistinguishable. This means that the process of fitting fiber material properties will preserve the stress anisotropy, allowing a close match of the stress-strain data simultaneously in both radial and circumferential directions.

Selecting the target experimental set: The fibers in the direct fiber model were not equally distributed in all directions. It seems reasonable to expect that this structural anisotropy will result in mechanical anisotropy (Coudrillier, Pijanka et al. 2015). It was therefore important to select for inverse fitting, among the multiple experimental results reported in the literature (Eilaghi, Flanagan et al. 2010), the one that exhibited a mechanical anisotropy matching the structural anisotropy of our model. To do this, we first quantified the mechanical anisotropy of our model (Figure 36). We did this by subjecting the model to displacement-controlled equi-biaxial stretch tests. At each strain level we quantified the model's stress anisotropy as the ratio of stresses in the orthogonal directions (S_{11}/S_{22}). The test was repeated several times with different fiber material property values. The results showed that the ratio of stresses had a fairly constant distribution and was essentially independent to the material properties changes within the ranges tested. With this, we were able to select the case with anisotropy most similar to that of our model among the several experimental results reported by Eilaghi et al.. Specifically, we selected the data for sample 76940-TS, as labeled by Eilaghi et al. (Eilaghi, Flanagan et al. 2010).

To be consistent with the selected experimental data, we assigned an equi-biaxial stretch of 2.16% as the displacement boundary condition to our fiber-matrix assembly. To optimize the fiber material properties (C_{10} and C_{01}), we used the simplex search method of Lagarias et al. (Lagarias, Reeds et al. 1998). The algorithm sought to identify the two parameters that yielded the closest match between the simulated and experimental stress-strain curves, simultaneously in both

directions. We optimized the fitness by minimizing the cost function, defined as the a between the model and experimental curves at 21 strain states. The optimization was terminated when the cost function value was smaller than 0.01. After optimization we also computed the adjusted R^2 between the curves to assess curve similarity. The complete inverse fitting process was repeated 11 times with various starting parameters to test the consistency and "uniqueness" of the results.

For interpretation of the results and to compare with other studies, it is useful to "convert" the optimal C_{10} and C_{01} parameters of the hyperelastic Mooney-Rivlin model into more intuitive representations of fiber mechanical properties. Specifically, we estimated the fiber shear modulus as $2(C_{10} + C_{01})$. We also derived a fiber elastic modulus by simulating uniaxial stretch of a single straight fiber with the optimal C_{10} and C_{01} values and the hyperelastic Mooney-Rivlin material. The fiber elastic modulus was then obtained as the slope of the stress-strain curve at 2.16% strain.

5.3 Results

After construction, the model consisted of 1016 fibers (or fiber bundles). Fiber orientation distributions and overall anisotropies were similar between the model and the tissue, as measured using PLM (Figure 37). In the sagittal plane, the anisotropies were 0.6031 and 0.5976 for the model and tissue, respectively (a difference smaller than 1%); In the coronal plane, the anisotropies were 0.1777 and 0.1626 for the model and tissue, respectively (a difference smaller than 10%).

Figure 37 shows the fiber orientation distributions of the direct fiber model and PLM images. The match of distributions was achieved simultaneously in both coronal and sagittal planes. By Wilcoxon rank sum tests, there were no significant differences in fiber orientation

distributions between the model and the PLM images, in either coronal ($p > 0.7$) or sagittal ($p > 0.6$) planes.

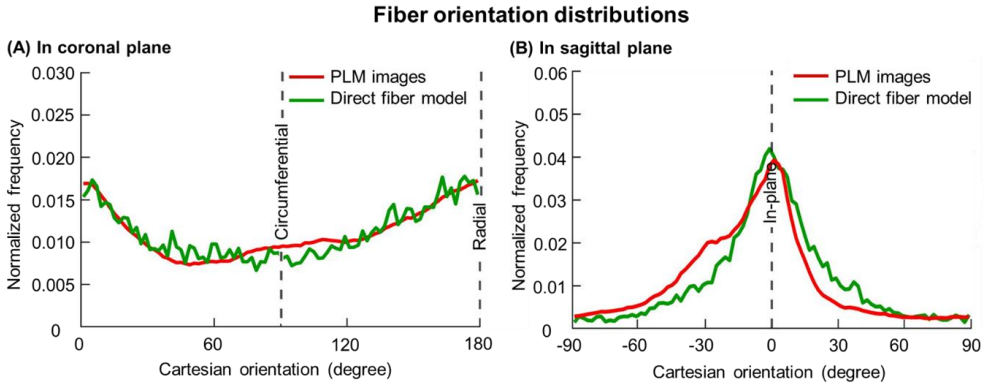

Figure 37. Fiber orientation distributions of the direct fiber model (green lines) and the PLM images (red lines), in the (A) coronal and (B) sagittal planes.For the coronal plane the PLM orientation was derived from the stack of 17 images. In the coronal plane the radial direction corresponds to 0 and 180 degrees and the circumferential direction with 90 degrees. For the sagittal plane, the PLM orientation shown is the average orientation distribution over the 236 regions analyzed. See main text for details. Frequencies were normalized by the total sum of frequencies. Overall these results show that fiber orientation distributions of the direct fiber model agreed well with those from the PLM images in both coronal (adjusted $R^2 = 0.8234$) and sagittal (adjusted $R^2 = 0.8495$) planes.

Figure 38 illustrates fiber displacements and stresses at half and full stretch. The large differences in stress between fibers were consistent with the anticipated process of stretch-induced recruitment (Grytz and Meschke 2010, Jan and Sigal 2018). All 11 optimization runs led to curves that were in good agreement with the experiment. They all led to fairly consistent estimates of fiber shear modulus, with an average of 1522.8 MPa and a standard deviation (STDEV) of 38.9 MPa (Table 2). Interestingly, these were obtained with C_{10} and C_{01} coefficients that varied substantially. For example, C_{10} ranged from 118.9 to 7881.8 MPa.

Table 2. 11 Sets of C_{10} and C_{01} hyperelastic Mooney Rivlin material parameters that led to stress-strain curves in good agreement with the experimental datafrom the literature (see main text). The resultant fiber shear modulus is with an average of 1522.87 MPa and a standard deviation of 38.94 MPa.

Set #	C_{10} (MPa)	C_{01} (MPa)	Shear modulus (MPa)
1	5732.2650	-4989.8000	1484.93
2	5929.2900	-5169.5800	1519.42
3	5971.4700	-5230.2900	1482.36
4	5722.4110	-4981.2290	1482.36
5	881.8312	-100.0000	1563.66
6	119.4267	662.3430	1563.54
7	119.3580	662.0210	1562.76
8	5746.9000	-5002.6000	1488.60
9	119.4156	662.3429	1563.52
10	7881.8000	-7140.0000	1483.60
11	118.9000	659.5000	1556.80
Max	7881.8000	662.3430	1563.66
Min	118.9000	-7140.0000	1482.36
Average	3485.7334	-2724.2993	1522.87
STDEV	3142.4550	3160.9742	38.94

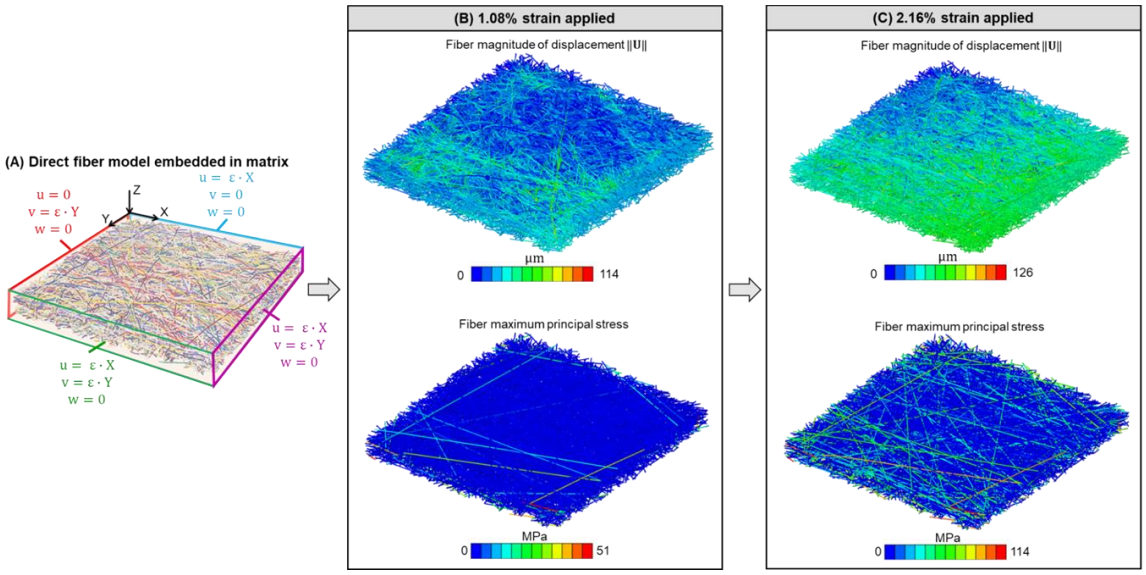

Figure 38. Schematic and visual representation of displacement boundary conditions and loading patterns in the direct fiber model of scleral tissue.(A) Schematic of the displacement boundary conditions for the fibers

and matrix to represent scleral tissue subjected to 2.16% equi-biaxial strain (ε). U is the nodal displacement vector of fiber with components u, v & w representing displacement in X, Y and Z direction, respectively. ‖U‖ is the fiber magnitude of displacement. In panel A the fibers are randomly colored to facilitate discerning their architecture. Panels B and C show isometric views of the direct fiber model with the fibers colored according to the magnitudes of displacement (top row) or maximum principal stress (bottom row). The model is shown when subjected to (B) 1.08% strain or (C) 2.16% strain. From the images it is clear that the model fibers exhibit complex loading patterns.

Figure 39 shows that the stress-strain curves of the optimal model fit very well the experimental data in both radial (adjusted R^2 = 0.9971; RSS = 0.00095) and circumferential directions (adjusted R^2 = 0.9508; RSS = 0.0098) simultaneously. The material parameters for the inverse fitting run that led to the closet model and experiment fit were C_{10} = 5746.9 MPa, and C_{01} = -5002.6 MPa.

The estimated fiber elastic modulus at 2.16% strain was 5.45GPa. The estimated fiber shear modulus is 1488.6 MPa.

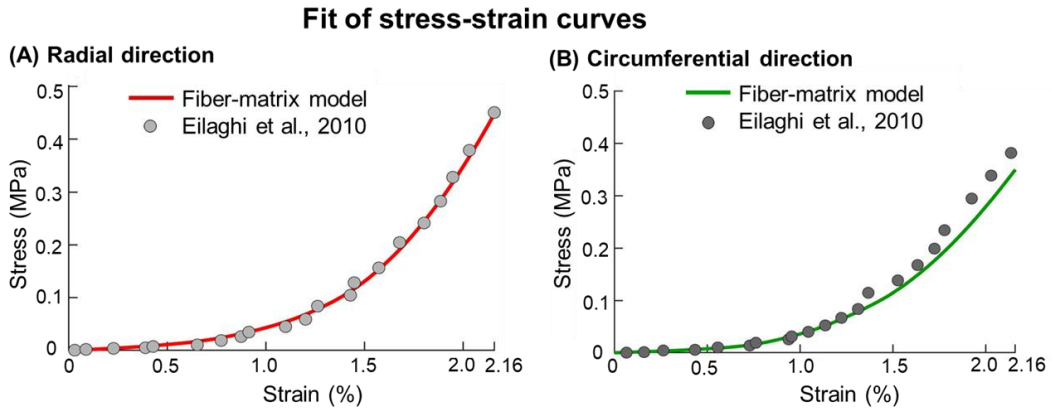

Figure 39. Fit of stress-strain responses between the model and the experiment.Fit of stress-strain response was achieved between the model and the experiment simultaneously in both the (A) radial direction (adjusted R^2 = 0.9971; RSS = 0.00095) and (B) circumferential directions (adjusted R^2 = 0.9508; RSS = 0.0098).

5.4 Discussion

Our goal was to develop a direct fiber modeling approach that captures both the microscale collagen fiber architecture and the macroscale mechanical behavior of the sclera. We demonstrated our approach by modeling a rectangular patch of the posterior sclera. The model incorporated several fiber characteristics ignored by most previous models of posterior sclera, such as fiber interweaving, fiber-fiber interactions, long fibers, and a physiologic experimentally-derived in-depth fiber orientation distribution. Below we provide a brief overview of the use of conventional continuum approaches to model the sclera, followed by a discussion on the importance of considering the fiber characteristics described above, and the strengths of the direct fiber modeling approach. We continue with a discussion on how to further interpret our models and the results obtained from them, including a comprehensive list of limitations.

5.4.1 Conventional Continuum Models Of Sclera

Numerical models of sclera have been widely developed and advanced for studying sclera structure and mechanics (Sigal, Flanagan et al. 2004, Girard, Downs et al. 2009, Girard, Downs et al. 2009, Grytz, Meschke et al. 2011, Coudrillier, Boote et al. 2013, Coudrillier, Pijanka et al. 2015, Voorhees, Jan et al. 2017, Voorhees, Jan et al. 2018, Hua, Voorhees et al. 2020). Most models have been formulated within a continuum mechanics framework in which collagen fiber architecture has been approximated using statistical distributions. For example, in a common approach, the scleral collagen microarchitecture is accounted for by collagen fiber “families”, each of which is described through the family preferred orientation and a “degree of alignment” around this preferred orientation (Girard, Downs et al. 2009, Grytz, Meschke et al. 2011, Coudrillier,

Boote et al. 2013). More advanced models have incorporated experimental data on collagen fiber orientations, obtained for example from small-angle light scattering or related scattering techniques (Coudrillier, Boote et al. 2013, Zhang, Albon et al. 2015, Schwaner, Hannon et al. 2020). Other recent models have focused on incorporating regional variations in fiber family characteristics (Kollech, Ayyalasomayajula et al. 2019). The success of the conventional models at the macroscale encouraged their use to predict microstructural characteristics of sclera fibers, such as collagen fiber crimp (Girard, Downs et al. 2009, Grytz, Meschke et al. 2011, Grytz, Fazio et al. 2014).

There is no doubt that the conventional models have been helpful in capturing macro-scale sclera mechanics, and to understand the interplay between mechanics and structure, both micro and macro. However as the experimental tools advance, the information available on sclera microstructure and mechanics has improved (Brown, Morishige et al. 2007, Winkler, Jester et al. 2010, Sigal, Grimm et al. 2014, Jan, Grimm et al. 2015, Coudrillier, Geraldes et al. 2016, Yang, Brazile et al. 2018, Behkam, Kollech et al. 2019, Ling, Shi et al. 2019, Pijanka, Markov et al. 2019, Yang, Lee et al. 2021, Hoerig, McFadden et al. 2022, Lee, Yang et al. 2022). These studies have demonstrated structural and mechanical characteristics of the sclera that are potentially crucial yet are not accounted for by the conventional continuum approach for modeling, such as fiber interweaving, fiber-fiber interactions and the in-depth fiber orientation distributions (Jan, Lathrop et al. 2017, Boote, Sigal et al. 2020, Lee, Yang et al. 2022). More importantly, some of those fiber characteristics are not suited to be incorporated under the continuum framework. This brings to the forefront the need to develop more advanced modeling techniques that can incorporate and take advantage of the newly available highly detailed information.

5.4.2 The Importance Of Considering Fiber Interweaving/Fiber-Fiber Interactions, Long Fibers, And In-Depth Fiber Orientation Distribution

A common preconception about the effects of fiber interweaving, and the resulting fiber-fiber interactions, seems to be that interweaving increases the stiffness of a material, or tissue. However, by comparing models with interweaving and non-interweaving fibers, we have shown that an interwoven architecture is, as a structure, more compliant than a non-interwoven architecture (Wang, Hua et al. 2020). This is consistent with the literature on textile mechanics (Saiman, Wahab et al. 2014, Stig and Hallström 2019). This effect can be understood by noting that the fibers of the interweaving architecture are undulated, whereas those from the non-interweaving models are straight. Straight fibers aligned with the load carry the forces more efficiently, and are shorter, and thus, the overall model is stiffer. Since fiber interweaving and the resulting fiber-fiber interactions play an important role in determining the structural stiffness of the sclera, it should be considered when modeling sclera biomechanics, as did our direct fiber model. Note that we are not the first to recognize the importance of fiber interweaving and fiber-fiber interactions in soft tissue biomechanics (Elliott and Setton 2001, Wagner and Lotz 2004, Guerin and Elliott 2007, Nerurkar, Mauck et al. 2011, Zhang, Lake et al. 2013). For example, in annulus fibrosus of intervertebral disc, interlamellar shearing can account for nearly 50% of the total stress associated with uniaxial extension. Therefore, interweaving collagen fiber layers may play an important role in annulus fibrosus tissue function.

It is important to note that the scale of the undulations of interweaving is different from that of the collagen fiber waviness referred to as crimp by us (Jan, Gomez et al. 2017, Gogola, Jan et al. 2018, Jan, Brazile et al. 2018, Jan and Sigal 2018) and others (Grytz and Meschke 2009, Grytz, Fazio et al. 2014, Grytz, Krishnan et al. 2020). For example, ocular collagen fibers crimp

has a period typically under 20 μm (Jan, Gomez et al. 2017, Gogola, Jan et al. 2018, Jan, Brazile et al. 2018, Jan and Sigal 2018), much smaller than the estimates of interweaving undulations on the order of 100 to 300 μm (Wang, Hua et al. 2020). From a mechanical perspective, the undulations of crimp affect directly the biomechanical behavior of a fiber under load, with the crimp "disappearing" as the fiber is loaded or stretched, and eventually recruited (Jan and Sigal 2018, Jan, Lee et al. 2022). The interactions between interwoven fibers mean that these undulations do not "disappear" under load, and are limited by the interlocking (Lee, Yang et al. 2022).

The collagen fibers of the sclera are long and continuous; thus, they can transfer forces over a long distance (Voorhees, Jan et al. 2018, Boote, Sigal et al. 2020). However, the conventional continuum approach to modeling sclera only considers the local or regional orientation distribution of these long fibers and maps such information into fairly small "finite elements" (Grytz, Meschke et al. 2011, Coudrillier, Boote et al. 2013). As a result, the force transmission is continuous across elements rather than along fibers, which alters the predicted mechanical behavior locally and potentially at the macroscale (Roberts, Liang et al. 2010, Coudrillier, Boote et al. 2013, Campbell, Coudrillier et al. 2015, Zhang, Albon et al. 2015, Voorhees, Jan et al. 2018, Kollech, Ayyalasomayajula et al. 2019, Zhou, Abass et al. 2019). We are not the first to recognize the importance of accounting for long fiber mechanics (Huang, Zhou et al. 2017, Lanir 2017, Grytz, Yang et al. 2020). One approach proposed to address the problem has been through the use of symmetry boundaries across elements. In this manner it is possible to simulate fibers that are continuous across elements. The approach, however, substantially limits the type of models that can be considered compared with the direct fiber model we present.

The collagen architecture of the sclera varies in depth (i.e., the direction perpendicular to the scleral surface) (Pijanka, Spang et al. 2015, Jan, Lathrop et al. 2017). Such variations are crucial

in the load-bearing capacity of the sclera (i.e., bearing shear stresses), and may even have clinical implications (Danford, Yan et al. 2013). Unfortunately, most fiber-aware models of the sclera only account carefully for the fiber orientations within the scleral plane, while the in-depth orientations are ignored or are modeled in a much more simplified manner than the out of plane orientations (Coudrillier, Boote et al. 2013, Zhang, Albon et al. 2015, Voorhees, Jan et al. 2017). Our direct fiber model incorporates both in-plane and in-depth specimen-specific fiber orientation distributions that match those measured using PLM, and thus, has a higher fidelity for representing the sclera and its mechanics.

5.4.3 Strengths Of Direct Fiber Modeling

Ultimately, a model is only as good as the predictions that can be made using it. On this, we point out that the fiber elastic modulus estimated with our direct fiber model is well within the range of values reported in the literature. For example, we estimated a fiber elastic modulus of 5.45 GPa, compared with those of 2-7 GPa of the bovine Achilles tendon (Van Der Rijt, Van Der Werf et al. 2006, Yang, Van Der Werf et al. 2007) and 5-11.5 GPa of the rat tail (Wenger, Bozec et al. 2007). In contrast, the estimates of fiber elastic modulus derived using continuum models, which used constitutive model formulations based on highly simplified assumptions of fiber architecture and behavior at the microscale level, are several orders of magnitude smaller, between 1 and 200 MPa (Grytz, Fazio et al. 2014, Coudrillier, Pijanka et al. 2015, Schwaner, Hannon et al. 2020, Schwaner, Perry et al. 2020). Hence, whilst both continuum and direct fiber models can closely approximate the macroscale sclera behavior, the estimates of fiber mechanical properties derived from both types of models can be substantially different. This may not be a problem when the intent is limited to describing tissue mechanical response. However, an important application

of continuum models is to “infer” characteristics of the underlying fibers. The large differences in fiber properties estimated by the continuum models and the experimental measurements already suggest that these should be interpreted very carefully as the values inferred may be inaccurate. A common application of this approach is to compare the fiber properties inferred from healthy and unhealthy tissues, or from young and old donors. The argument in this case is based on the idea that the methods may not produce accurate fiber estimates, but that the comparison remains valid. This may indeed be the case. But it is also possible that if the changes with pathology or age involve aspects of the fibers that are not accounted for in the continuum model formulation, then the origin of the changes will end up artefactually attributed to another tissue characteristic. Thus, while all models involve important approximations, if the goal is to derive estimates at the fiber scale, we posit that direct fiber models are preferrable over continuum models.

The methodology to build the direct fiber model structure can be applied to other collagenous tissues. The reconstruction method is not tied to PLM and can instead be done using second harmonic imaging or confocal microscopy, as long as they provide information on the density and orientation of collagen fibers. The level of detail necessary from the images can depend on the complexity of the tissue in question and the accuracy needed from the reconstruction and simulations. Because the sclera has a complex 3D architecture, we combined histological information from two sectioning directions. This may not be necessary for other tissues, or perhaps it may be possible to obtain depth information by taking advantage of the confocal nature of the imaging or 3D PLM (Yang, Jan et al. 2018).

5.4.4 Considerations Of The Uniqueness Of Material Parameters And Fiber Interpenetrations

A common concern with inverse fitting is the uniqueness of the so-called optimal parameters (Girard, Downs et al. 2009, Girard, Suh et al. 2009, Zhou, Abass et al. 2019). When we repeated the optimization with various starting parameters, we obtained fairly consistent fiber shear modulus predictions. However, the material model parameters C_{10} and C_{01} varied substantially (Table 2). This was not a surprise given the material formulation we used and the clear potential for interactions between the parameters (van Tonder, Venter et al. 2023). Altogether, this reinforces the importance of focusing on parameters with a clear physical interpretation, in this case fiber shear modulus. Such parameters are more likely to have better stability.

From a numerical perspective, prevention of fiber penetrations is computationally intensive. We took advantage of highly mature general contact tools implemented in commercial code to keep solution time reasonable. Ensuring absolutely no interpenetration would have required an impractical number of small elements to represent the undulating fibers. To avoid this problem, we decided to quantify and track the interpenetrations and consider a solution valid if these remained below 5% of the fiber diameter. In a worst-case scenario this would mean that two interacting fibers have “pushed” into each other such that the distance between their centers is only 95% of twice their radii. We assumed that the fibers are all circular and remain circular, despite pushing into each other.

5.4.5 Limitations

When interpreting the results from this work, it is important to consider also the following limitations. First, we considered highly simplified fiber-fiber interactions and ignored fiber-matrix interactions. We are aware that the forces between fibers may be much more complex, including friction, crosslinks and several other physical processes that are challenging to simulate. Some of these may have major impact on the results, and others may not. This likely depends on the specific structure and loading conditions of the tissue. We carried out a friction sensitivity test in which we repeated the inverse fitting while using several friction coefficients. The results were very similar in stress-strain (less than 5% difference). We thus conclude that in the particular test reported herein ignoring friction did not adversely affect the accuracy of the model estimates substantially. Fiber-matrix interactions are potentially even more complex than fiber-fiber interactions given the wide diversity of components that form what we describe simply as "matrix". These include non-fibrous components, such as GAG chains, that may act as lubricants and affect sliding, in which case their presence could make the tissue more compliant (Murienne, Chen et al. 2016, Hatami-Marbini and Pachenari 2020). Other components include elastin fibers and cells. While we acknowledge the highly simplified fiber-fiber and fiber-matrix interactions we used in this study, we argue that the methodology we have described can be extended to incorporate much more complex interactions. Conventional continuum modeling techniques of the eye and other tissues simply ignore fiber-fiber and fiber-matrix interactions, yet it is not obvious to readers that these assumptions have been made, or how to relax them.

Second, we did not account for sub-fiber level features, such as collagen fiber crimp and various fiber or bundle diameters. Future work would benefit from introducing collagen fiber crimp (Grytz, Fazio et al. 2014) and various fiber diameters (Komai and Ushiki 1991).

Third, our direct fiber model does not account for the very large number and complexity of fibers of the sclera. We posit that the fiber-level mechanics presented using the direct fiber model with reduced fiber density will likely be similar to the actual tissue. Therefore, our objective of introducing direct fiber model for simulating sclera is fulfilled. Meanwhile, it's beneficial to use fewer fibers to reduce computational cost. We agree that in future work, it will be worthwhile to work on improving computational efficiency and building the model with more fibers.

Fourth, we did not account for regional variations. In our model structure we did not observe the strong well-aligned region of fibers in the radial direction that have been reported to take about 10% of the sclera nearest to the choroid. This could be due to variations between eyes, regional inhomogeneities (the radial fibers appear to be more readily distinguished closer to the optic nerve head) or due to the specific coronal sections used for the reconstruction. It is likely that other regions and other eyes will produce different models that respond differently to mechanical loading. We posit that our goal in this manuscript was modest, aiming to demonstrate it is possible to build a fiber-based model that produces a macroscopic mechanical behavior matching experimental tests. It will be beneficial to consider more features and variations in future work.

Fifth, the model used to demonstrate the direct fiber method was reconstructed from PLM and experimental data from different species. We posit that the impact was minor because our goal was to demonstrate the reconstruction and modeling methodology. It should be clear to readers that the process could be redone with all data from the same species. In this sense the key result from this work still stands: the direct fiber modeling technique can work. If the goal is to obtain fiber properties that are as accurate as possible for a given species, then using all consistent data is probably necessary. More samples will also be needed to account for variability.

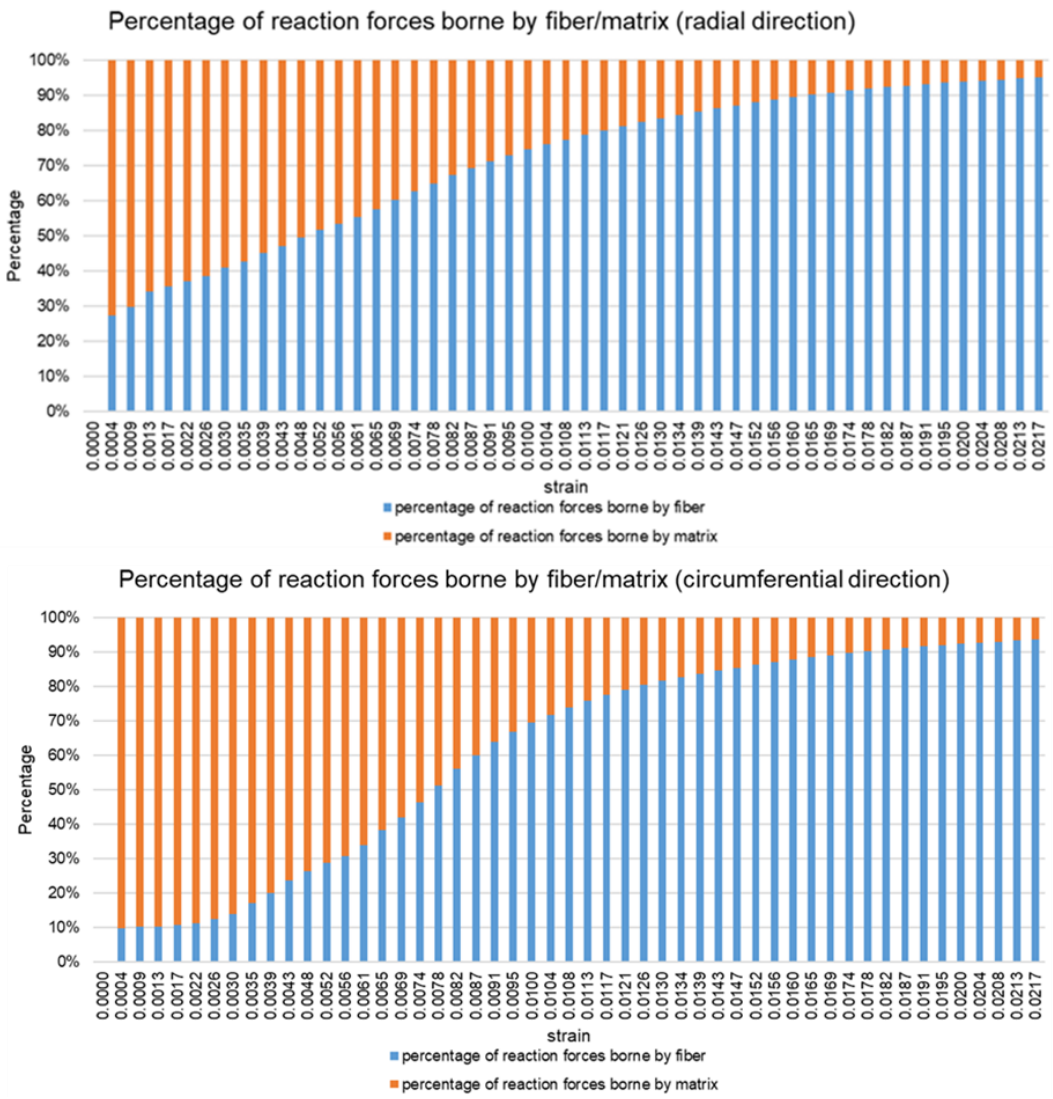

Figure 40. Total reaction forces borne by the matrix and fibers, respectively.

Sixth, the matrix mechanical properties were kept constant at literature values and not optimized iteratively like the fiber properties. This was for the sake of simplicity. Although the matrix properties could impact the load bearing of the fibers and potentially influence the fiber material parameters fit, we believe the impact is minor. It is because the matrix is much softer than the fibers (Coudrillier, Pijanka et al. 2015) and, consequently, the fibers are the principal load-bearing component (Girard, Downs et al. 2009, Huang, Fan et al. 2013). The final results in our

model show that the total reaction forces borne by the matrix are 5%-10% of those borne by the fibers at 2% of strain (Figure 40). Therefore, we reasoned that the properties of the fibers will predominantly influence how the model behaves and the matrix stiffness has only a slight influence on the fiber material parameters derived. Nevertheless, it would be beneficial to consider matrix properties variations in future studies. Introducing matrix properties changes to the model may be necessary to properly account for the effects of age and interweaving, given the evidence that changes in matrix properties could result in age-related changes in sclera properties (Grytz, Fazio et al. 2014).

Seventh, although our model has similar boundary conditions to the experiment it is impossible to match the experiment precisely. Holding the tissues with clamps, rakes or hooks alters the boundary conditions, in ways that are extremely complicated to replicate computationally. Moreover, the experiments to which we fit the model were biaxial stretch tests. This is not the physiologic mechanical condition of sclera. The mechanical behavior of sclera under inflation or more complex modes could be different.

Eighth, we have chosen only one set of experimental data for estimating the material properties of the fibers. Given the complexity of the mechanical behavior of sclera, fitting only a biaxial stretch test does not guarantee that the model will generalize to other conditions. It may be necessary to fit simultaneously to several experimental tests, as has been done for continuum models (Thomas, Lai et al. 2019).

Ninth, the thickness of the direct fiber model was 0.35mm, but the sclera thickness in Eilaghi et al.'s experimental study was roughly 0.5mm. Although there is a discrepancy in thickness, we believe it will not affect the derived fiber material properties because these were obtained by fitting stress-strain curves.

5.5 Conclusion

We have shown the possibility of developing specimen-specific direct fiber model of sclera that can represent the sclera fibrous microstructure better than the previous continuum modeling approaches and allow accurate capture of sclera mechanics. We successfully built the model with long, continuous, interwoven fibers that takes into account the effects of fiber interweaving and fiber-fiber interactions. Our results have demonstrated that the direct fiber model can match the fiber orientations measured in high-resolution PLM images simultaneously in coronal and sagittal planes. The model properties can be optimized through inverse fitting to match experimental stress-strain responses. The estimated fiber elastic modulus is in good agreement with the literature. The direct fiber modeling methodology potentially has broad application to simulate other fiber-based tissues. Overall, the direct fiber modeling technique in this study is important for characterizing sclera collagen architecture at the fiber level, analyzing microstructural responses to macroscale mechanical loadings, and for understanding the scleral biomechanical environment.

6.0 Validation Of The Direct Fiber Modeling Approach To Simulate Sclera Collagen Fiber Architecture And Anisotropic Mechanical Behaviors

The content of this chapter is in preparation as a manuscript.

6.1 Introduction

Collagen fibers serve as the primary load-bearing component of the sclera (Girard, Downs et al. 2009, Pijanka, Coudrillier et al. 2012, Grytz, Fazio et al. 2014, Jan, Gomez et al. 2017, Boote, Sigal et al. 2020), making them crucial for understanding the sclera mechanical behaviors and the eye physiology and pathology (Ethier, Johnson et al. 2004, Summers Rada, Shelton et al. 2006, Coudrillier, Tian et al. 2012, Pijanka, Coudrillier et al. 2012). Thus, numerous studies have been conducted to investigate the influence of collagen microarchitecture on sclera biomechanical behaviors (Girard, Downs et al. 2009, Grytz, Meschke et al. 2011, Coudrillier, Boote et al. 2013). Direct measurement is challenging due to the complexity of sclera microstructure and the difficulty of accessing it directly for experimentation. Consequently, numerical modeling has become a widely employed approach for studying the sclera fiber structure and mechanical behaviors (Girard, Downs et al. 2009, Grytz, Fazio et al. 2014, Pijanka, Spang et al. 2015, Whitford, Joda et al. 2016, Voorhees, Jan et al. 2018, Kollech, Ayyalasomayajula et al. 2019, Zhou, Abass et al. 2019).

However, there remains a need for developing a reliable model due to the existing models' inability to accurately capture crucial characteristics of collagen fibers. In our previous work, we

demonstrated that the current sclera numerical models were predominantly developed within a continuum mechanics framework and overlooked essential features such as fiber interweaving, fiber-fiber interactions, long fibers, and detailed fiber orientation distributions. Neglecting interweaving and fiber-fiber interactions can lead to significant errors when estimating the mechanical properties of scleral fibers through inverse fitting (Wang, Hua et al. 2020). Accurately incorporating fiber characteristics at the microscale is vital for understanding the effects at the cellular and axonal levels and studying mechanobiology (Lee, Yang et al. 2022).

To address these issues, we introduced the direct fiber modeling technique (Ji, Bansal et al. 2023). This approach integrated the specimen-specific 3-dimensional fiber orientations obtained through polarized light microscopy (PLM) (Jan, Grimm et al. 2015) while considering commonly ignored fiber characteristics, including interweaving, fiber-fiber interactions, and long fibers. Using an inverse fitting approach, we successfully matched experimental biaxial stress-strain data from the literature, simultaneously capturing the stress-strain behavior in both radial and circumferential directions. Although the direct fiber modeling approach showed promise and allowed for the consideration of critical fiber characteristics compared to conventional continuum approaches, it still possessed two primary limitations. First, we have yet to establish the robustness of the direct fiber modeling approach in capturing the varying fiber architecture observed in different samples. This is an important consideration as scleral fiber characteristics may vary among locations and individuals (Gogola, Jan et al. 2018). Second, our previous testing of the model's behavior has been limited to equi-biaxial loading conditions, neglecting the more complex loading conditions that the sclera may experience in physiological contexts (Boote, Sigal et al. 2020).

In this study, our aim was to expand on the analysis of the direct fiber modeling technique and conduct a more comprehensive investigation. First, we aimed to evaluate the robustness of the direct fiber modeling approach in simulating various collagen microstructures of posterior sclera. We showed that the direct fiber model can effectively capture the collagen structure of the tissue across multiple samples. Second, we aimed to match the behaviors of the direct fiber models with experimental stress-strain data obtained from multiple samples. Specifically, we aimed to achieve a more demanding requirement, wherein the model could match the behaviors observed under various biaxial loading conditions, including both equi-biaxial and non-equi-biaxial scenarios. Our results indicated that by fitting the model to one loading condition, the derived fiber material properties allowed for automatic matching of the behaviors under other loading conditions as well. Overall, the direct fiber modeling technique demonstrated its robustness and effectiveness in characterizing the collagen architecture at fiber level and representing the anisotropic mechanical behaviors of the sclera, which can provide unique insight into the interplay between tissue fiber architecture and behavior.

6.2 Methods

This section is organized in three parts. First, biaxial mechanical testing was conducted on healthy sheep posterior samples to obtain their stress-strain responses. Second, after running mechanical testing, we sectioned the samples and imaged the sections using PLM. The PLM images were post-processed that could be referenced to build direct fiber models. Third, we built direct fiber models based on the PLM-derived fiber orientation data. The direct fiber model was embedded in a matrix representing non-collagenous components. The combined fiber and matrix

model was used in an inverse fitting optimization process to match the simulated stress-strain behaviors with experimental data, where we derived the optimal fiber material properties and pre-stretching strains.

All the image processing was done in MATLAB v2020 (MathWorks, Natick, MA, USA) and FIJI is Just ImageJ (FIJI) (Preibisch, Saalfeld et al. 2009, Schindelin, Arganda-Carreras et al. 2012). Modeling was done in Abaqus 2020X (Dassault Systemes Simulia Corp., Providence, RI, 171 USA). Customized code and the GIBBON toolbox (Moerman 2018) for MATLAB v2020 (MathWorks, Natick, MA, USA) were used for model pre/post-processing and inverse fitting.

6.2.1 Biaxial Mechanical Testing

The experimental procedures were conducted in collaboration with a partner laboratory, utilizing a well-established methodology (Thomas, Lai et al. 2019, Salinas, Clark et al. 2020). The study was conducted in accordance with the tenets of the Declaration of Helsinki and the Association of Research in Vision and Ophthalmology's statement for the use of animals in ophthalmic and vision research. Three fresh sheep eyes were obtained from a local slaughterhouse within 24 hours postmortem and immediately transferred to the lab in a cold isotonic phosphate buffer saline (PBS) solution. Upon arrival, two posterior sclera samples measuring 11mm x 11mm were carefully excised from both temporal and superior quadrants, approximately 2 to 3 mm away from the sclera canal (Figure 41). For the purpose of optical tracking and tissue deformation/strain analysis, four submillimeter glass markers were affixed to the surface of each sample.

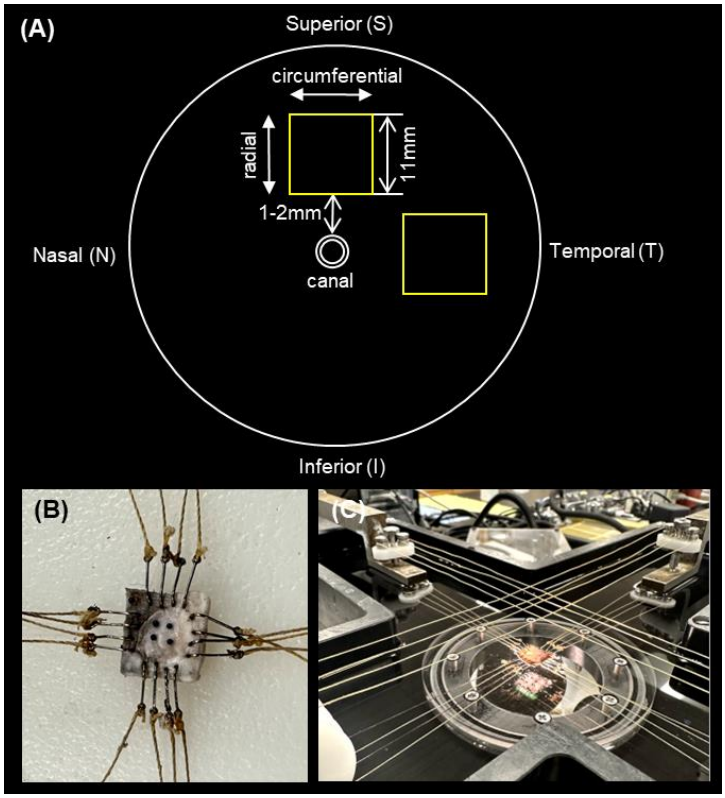

Figure 41. Key aspects of the experimental setup and procedures for the biaxial testing.(A) Schematic diagram showcasing the posterior pole of the eye, highlighting the locations of the two samples (depicted as yellow boxes) that were obtained specifically for the biaxial testing. (B) An example image showcasing a sample with hooks attached, ready for biaxial testing. The hooks ensure proper mounting and fixation of the sample during the experimental procedures. (C) The sample was mounted on a custom-built biaxial mechanical testing system. The loading axes of the system were aligned with the circumferential and radial directions of the sample, ensuring precise application of stress in the desired directions. The sample was then subjected to the five loading protocols, each designed to induce specific stress-strain behaviors. Note that the crossed strings, as depicted at the lower right of the sample, were corrected prior to conducting the experiment.

The sample was then mounted onto the biaxial testing equipment using fish hooks, with the loading axes aligned with the circumferential and radial directions of the sample (Figure 41). A 0.5g tare load was initially applied to flatten the sample. Subsequently, each sample was

subjected to biaxial stress control and underwent five distinct loading protocols (Table 3). Each loading protocol consisted of ten 20-second cycles. The first nine cycles served as a preconditioning phase, while data from the last loading cycle was used for subsequent analysis. Based on preliminary tests, a maximum stress level of 150kPa was applied, as it allowed the sample to maintain its shape without incurring damage. Once the stress-strain data were obtained, the samples were carefully unmounted from the biaxial testing equipment and then immersion fixed in 10% formalin for a duration of 24 hours.

Table 3 Maximum radial (anterior-posterior) and circumferential (equatorial) stress values for each biaxial loading protocol.

Loading Protocol #	Radial (kPa)	Circumferential (kPa)
1:1	150	150
1:0.75	150	112.5
0.75:1	112.5	150
1:0.5	150	75
0.5:1	75	150

Table 4. Information about the four posterior sclera samples used for direct fiber modeling.The samples were obtained from both the superior and temporal quadrants of three sheep eyes. Each sample had a different thickness, resulting in a variation in the number of collected coronal sections.

Sample #	Temporal/Superior	Sheep #	Thickness(μm)	Number of Coronal Sections
1	Superior	Eye-1	528	50
2	Temporal	Eye-2	1168	87
3	Superior	Eye-2	635	60
4	Temporal	Eye-3	838	74

Stress-strain responses were obtained from a total of four samples. Specific details regarding these samples can be found in Table 4. These four samples were utilized for further

analyses. Note that two additional samples, derived from the three eyes used in the experiments, were excluded from the analysis due to tissue damage incurred during the experimental procedures.

To address the presence of noise or variability observed at the initial stages of the stretch in the raw experimental stress-strain data, these data points were excluded from the direct fiber modeling and inverse fitting process. To further enhance the quality of the stress-strain curves, we employed a moving average smoothing algorithm to smooth the stress-strain curves (Chang, Li et al. 2015). For the rest of the analysis, we have been using the experimental data after smoothing.

6.2.2 Histology, Polarized Light Microscopy And Image Post-Processing

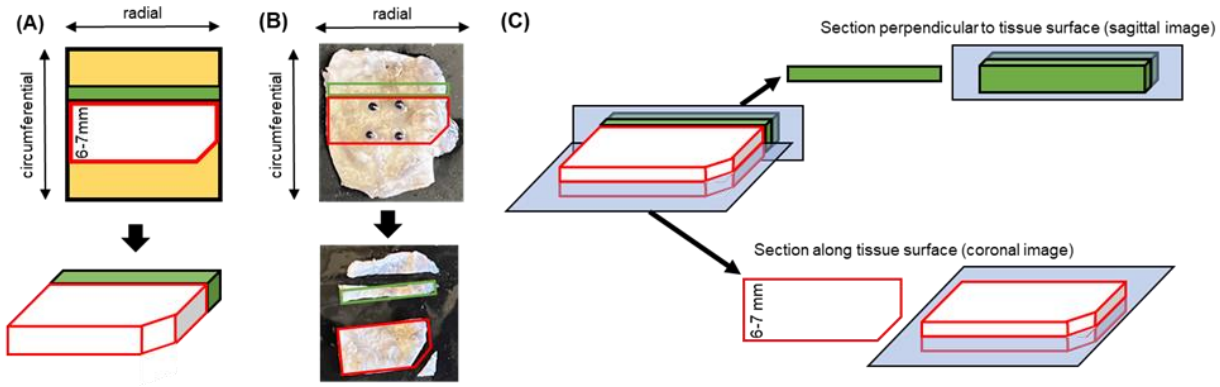

Figure 42. Process of sectioning a sclera sample. (A) Sclera sample after biaxial testing was processed for sectioning (top: 2D view; bottom: 3D view of the region for sectioning). A notch at the corner of the sample was used to indicate the tissue directions. Since it was not feasible to section the same piece of tissue both coronally and sagittally, a sample (depicted as a white block, the shorter length was 6-7mm) was obtained from the center of the tissue. Additionally, another sample was acquired from the adjacent tissue next to the white block (shown as a green block). (B) An example image of the sclera tissue with the two samples dissected. Prior to dissection, the fiberglass markers attached to the tissue were carefully removed. (C, top) The green block was sectioned sagittally, resulting in sagittal sections of the tissue. (C, bottom) The white

block was coronally sectioned, allowing for the acquisition of serial sections without any loss. The blue surface depicted in the image represented the plane of sectioning.

Following the fixation process, the samples were cryo-sectioned into 20 μm slices (Figure 42). For coronal sections, serial sectioning was performed at the center of the sample, where the sections were collected starting when there was visible sclera and stopping when the sclera was no longer visible. The number of sections collected varied among the different samples, and the specific quantities are detailed in Table 4. As for sagittal sections, two sections positioned close to the center square-shaped sample were obtained. Coronal and sagittal sections can be considered as the two orthogonal views of the collagen structure, providing information on the three-dimensional organization of the fibers.

All sections were imaged with PLM as described before (Jan, Grimm et al. 2015, Jan, Lathrop et al. 2017). Briefly, two polarized filters (Hoya, Tokyo, Japan) were used, one a polarizer and the other an analyzer, to collect images at four filter orientations 45° apart. The images were all captured using an Olympus MVX10 microscope (1× magnification setting, 6.84 μm/pixel).

PLM images were processed to derive the in-plane collagen orientation at each pixel (in Cartesian coordinates) and a parameter that we referred to as “energy” (Yang, Jan et al. 2018). Energy helped identify regions without collagen, such as outside of the section, and regions where the collagen fibers were primarily aligned out of the section plane, so that they can be accounted for in the orientation distribution. Following the processing of PLM images, all images obtained from a single sample were sequentially stacked and subjected to registration (Gogola, Jan et al. 2018). After registration, the original images underwent reprocessing to obtain "corrected" orientation angles. These corrected angles were determined based on the intersection rotations resulting from the registration process.

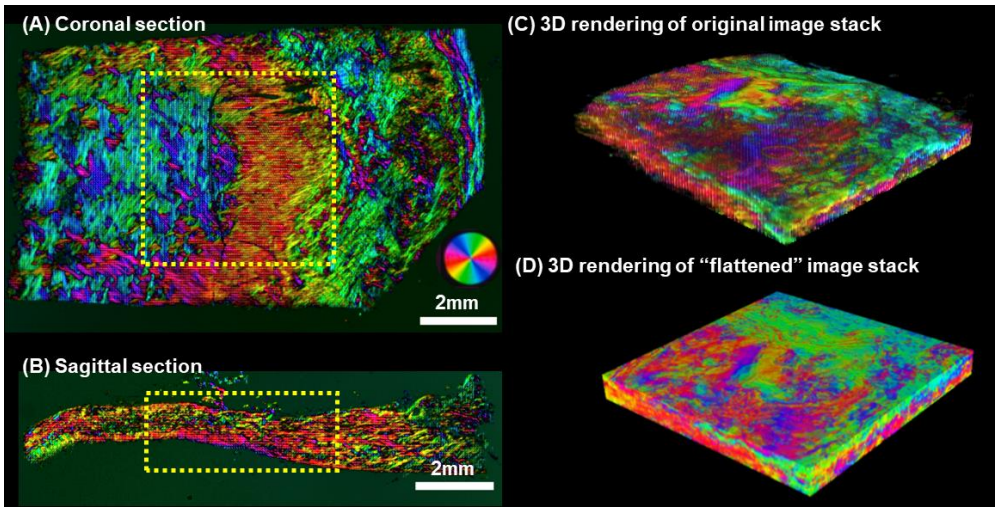

Figure 43. Example PLM images and process of image post-processing. (A) Example PLM image of a coronal section. A square-shape block was cropped from the stack and used as a reference to build the direct fiber model. (B) Example PLM image of a sagittal section. The model's in-depth fiber orientation distribution was adjusted based on the orientations obtained from the yellow block. The position of this block corresponded to the position of the square-shaped block obtained from the coronal section. The colors indicate the local fiber orientation in the section plane, with brightness proportional to the "energy" parameter. (C) The original stack showed irregular thickness from one location to another. (D) After interpolation, the thickness of the stack was uniformized which facilitates the tracing of fibers during the construction of the direct fiber model.

To focus on a specific area for subsequent construction of the direct fiber model, we selected a square-shaped block positioned at the center of the coronal sections. The dimensions of this selected block were 4.1x4.1mm (Figure 43 A). However, due to the irregular shape of the tissue and the folds caused during tissue sectioning, the stack of cropped blocks exhibited variations in thickness (Figure 43 C). In order to facilitate fiber tracing for the construction of the direct fiber model, we implemented a linear interpolation algorithm, as described by Akima (Akima 1970, Akima 1974). The interpolation algorithm was employed to interpolate angle and energy values at each location in-depth within the stack, thereby converting the inconsistent thicknesses into a uniform value. As a result of this interpolation, the image stack was transformed

into a uniform and regular block (Figure 43 D). Importantly, we proved that this interpolation process did not alter the orientation distribution of the fibers within the stack.

To validate the geometry of the direct fiber model, we computed both the coronal and sagittal collagen fiber orientation distributions. For the coronal orientation distribution, we utilized the pixel-level PLM data obtained from the original image stack, taking into account the local "energy" at each pixel. Similarly, for the sagittal orientation distribution, we summed up the PLM data obtained from the cropped block of the two sagittal sections (depicted in Figure 43 B). Again, the energy weighting was applied to ensure accurate representation of the collagen fiber orientations in the sagittal plane.

6.2.3 Direct Fiber Modeling

6.2.3.1 Model Construction

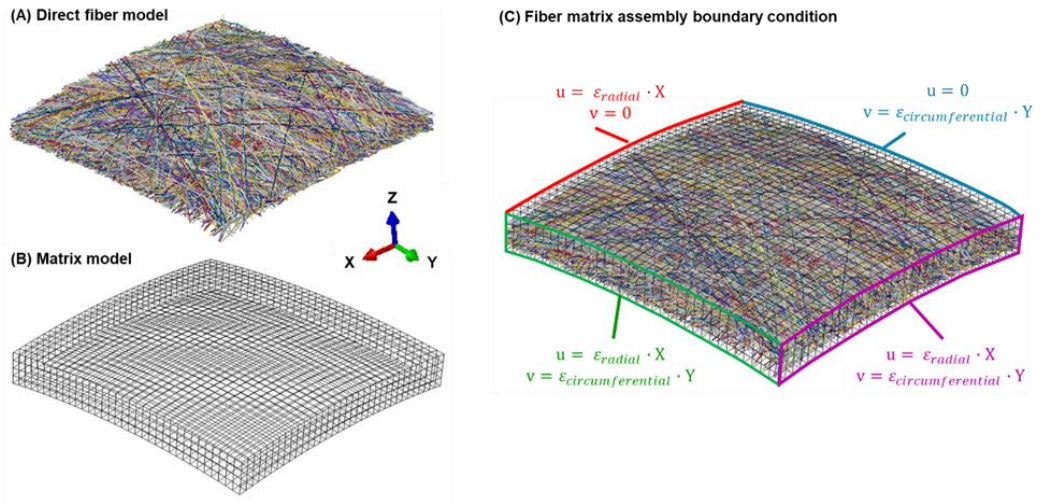

Figure 44. Example of the direct fiber model and boundary conditions.Isometric view of an example (A) direct fiber model and (B) matrix model. (C) Displacement boundary conditions were applied to the fiber matrix assembly, with components u, v representing displacement in X (radial) and Y (circumferential) direction, respectively. The displacement in Z direction was not constrained, given that fish hooks and strings

did not restrict the sample's displacement in the Z direction. In the first step biaxial stretch, the value of ε_{radial} and $\varepsilon_{circumferential}$ were optimized and derived in the inverse fitting procedure. In the second step biaxial stretch, the experimental strain values were assigned to ε_{radial} and $\varepsilon_{circumferential}$, aiming to match the model with the stress-strain behaviors observed in the experimental data.

We constructed four models (Figure 44 A) based on the procedure described previously (Ji, Bansal et al. 2023), corresponding to each sample listed in Table 4. Briefly, fibers were simulated using 3-dimensional linear truss elements (T3D2 in Abaqus). The locations of fibers were defined by sampling orientation values from PLM images at regularly spaced "seed" points (437 μm apart). Straight fibers, 13.68 μm in diameter, were traced at each seed point based on its orientation angle. The process was repeated for each layer, resulting in a stack of 2D fiber layers with interpenetrating fibers. An algorithm was employed to resolve interpenetrations by iteratively shifting the elements until they no longer overlapped (Matuschke, Ginsburger et al. 2019, Matuschke, Amunts et al. 2021). Fiber elements were re-meshed to maintain lengths between 82μm and 164μm, while controlling the minimum radius of curvature for smoothness. The amplitudes of the fiber undulations in-depth were adjusted to more accurately represent the distribution of fibers in three dimensions.

To account for the natural curvature of the sclera, an additional step was performed to adjust the flat fiber model and match it to the curvature of the eyeball. The radius of three sheep eyes was manually measured, and the average radius was determined to be 14856 μm. The flat model was then projected onto a sphere with a radius of 14856 μm, effectively introducing curvature to the model. It was important to note that this assumption assumed the sheep eye closely resembled a sphere, disregarding any variations in radius that may exist around the globe.

To assess the similarity between the model and the PLM images, the orientation distribution of the curved model was quantified and compared with the distribution obtained from the PLM images. This comparison aimed to evaluate how well the model captured the observed fiber orientations in the images. The quantification involved counting the occurrences of element orientations within the model, where each element's orientation represented the slope angle in the section plane. This approach accounted for varying element sizes and enabled a proper comparison with the pixel-based measurements obtained from PLM. To evaluate the fitness of the orientation distributions, adjusted R-squared (adjusted R^2) values were employed (Miles 2005). The adjusted R^2 values provided a measure of how well the model's orientation distribution fit the distribution observed in the PLM images. The use of adjusted R^2 values allowed for the consideration of the complexity of the model and the number of parameters involved, providing a more robust evaluation metric.

In addition to the fiber model, a matrix model was also constructed (Figure 44 B). The matrix model was designed to have the same curvature as the fiber model, ensuring consistency between the two. The matrix model shared the same dimensions as the fiber model, ensuring that the simulated fibers and matrix aligned properly. The end-nodes of the fibers were positioned on the surfaces of the matrix, creating a cohesive representation of the fiber-matrix structure.

6.2.3.2 Model Inverse Fitting

6.2.3.2.1 Meshing And Material Properties

Fibers were modeled as a hyperelastic Mooney-Rivlin material (Holzapfel 2001). W was the strain energy density and calculated as $W = C_{10}(I_1 - 3) + C_{01}(I_2 - 3) + \frac{1}{2}K(J-1)^2$, C_{10} and C_{01} were the material constants, restricted by $C_{10} + C_{01} > 0$ and would be determined by inverse

fitting, I_1 and I_2 were the first and second invariants of the right Cauchy-Green deformation tension, K was the bulk modulus and J was the determinant of the deformation gradient. The matrix was modeled as a neo-Hookean material with a shear modulus of 200 kPa (Girard, Downs et al. 2009, Coudrillier, Pijanka et al. 2015).

The fiber components were modeled using 3-dimensional linear truss elements (T3D2) in Abaqus. The length of the fiber elements ranged from 82 μm to 164 μm, resulting in aspect ratios between 6 and 12. The matrix was meshed using linear eight-noded hybrid hexahedral elements (C3D8H) in Abaqus. The element size for the matrix varied among the samples due to differences in sample thickness, which ranged from 101 μm to 179 μm, with 4 to 6 elements spanning the shell thickness. To ensure model accuracy, a mesh refinement study was conducted. The fiber model's mesh density was doubled, while the matrix model had its mesh density doubled in both in-plane directions and the thickness direction. The study's findings indicated that altering the mesh density had a negligible impact on stress predictions, with stress values changing by less than 1%. Based on these findings, the chosen mesh density was deemed sufficient to ensure numerical accuracy in the obtained results.

6.2.3.2.2 Interactions

Fiber-matrix interactions were ignored, as is usual in biomechanical models of the eyes (Grytz and Meschke 2009, Petsche and Pinsky 2013, Grytz, Fazio et al. 2014).

Fiber-fiber interactions were simulated in the following two ways. First, the interactions were considered by preventing fiber interpenetrations using Abaqus' general contact with no friction. Second, to enhance the interweaving effect of fibers and prevent them from sliding apart during stretching, a method involving the constraint of nodes was employed. Approximately 10% of the nodes, primarily located in the outer surface or boundary of the model, were selected. These

nodes were connected to their closest neighboring nodes, and their relative motion in the Z direction was constrained to zero using linear constraint equations in Abaqus. By applying these constraints, the free ends of the fibers were better controlled, resulting in a more stable and realistic model.

6.2.3.2.3 Finite Element Analysis Procedure

The fiber-matrix assembly underwent a quasi-static biaxial stretching process to match the experimental stress-strain data obtained in Method Section 6.2.1. The matrix was simulated using Abaqus standard implicit procedure, while the direct fiber model utilized Abaqus dynamic explicit procedure to enhance convergence and computational efficiency. The resulting stresses σ in the radial and circumferential directions were a combination of matrix and fiber contributions, with the matrix stress weighted by the fiber volume fraction (VF): $\sigma = (1 - \mathrm{VF})\sigma_{\mathrm{matrix}} + \sigma_{\mathrm{fibers}}$.

To ensure efficient dynamic analysis, mass scaling was implemented, allowing for a stable time increment of 1e-5. The simulation was conducted within a time period where inertial forces remained negligible, with the kinetic energy kept below 5% of the internal energy to confirm the insignificance of inertial effects.

6.2.3.2.4 Boundary Conditions And Inverse Fitting Procedure

In the biaxial stretching process of the fiber-matrix assembly (Figure 44 C), a two-step approach was employed to simulate the experimental conditions. In the first step, biaxial stretching was applied to pre-stretch the model. This step aimed to simulate the initial stretching process that occurs when a 0.5g tare load is applied to flatten the tissue. The resulting stress and strain values from this step were not recorded, as they were not included in the reported experimental stress-strain data. In the second step, the model was further stretched, and the same strains observed in the experiment were assigned as the displacement boundary condition to the fiber-matrix model.

In this step, the model stress and strain values were recorded, starting from 0. This approach was consistent with the experimental setup, where the stress and strain resulting from the tare load were not included in the reported experimental stress-strain data. By applying this two-step biaxial stretch with the appropriate displacement boundary conditions, the model aimed to replicate the mechanical behavior observed in the experiment and allow for a comparison between the model's stress-strain behaviors and the experimental data.

During the inverse modeling procedure, there were four parameters that needed to be determined. The first two parameters were the pre-stretching strains along the radial and circumferential directions in the first step of the biaxial stretch. Since the resultant strains caused by the tare load were not characterized in the experiment, these values were unknown and needed to be determined through the inverse modeling process. The second two parameters were the material properties of the fibers (C_{10} and C_{01}).

In the inverse fitting procedure, two optimizations were performed to determine the optimal parameters and match the stress-strain data of the five loading protocols. In the first optimization, all four parameters (pre-stretching strains and fiber material properties) were optimized to match the stress-strain data obtained using loading protocol 1:1. Further discussion on the selection of loading protocol 1:1 can be found in Section 6.4. A simplex search method was used for this optimization (Lagarias, Reeds et al. 1998). The algorithm aimed to find the values of the parameters that minimized the residual sum of squares (RSS) between the simulated and experimental stress-strain curves. The optimization process continued until the adjusted R^2 value between the curves exceeded 0.9, indicating a good fit between the model and experimental data. This optimization allowed for the determination of the optimal pre-stretching strains and fiber material properties (C_{10} and C_{01}).

In the second optimization, only the two pre-stretching strains were optimized, using the derived fiber material properties from the first optimization. This optimization aimed to match the stress-strain data obtained from the remaining four loading protocols. The same search method as before was employed, and the optimization was concluded when the adjusted R^2 value between the stress-strain curves exceeded 0.9 in both loading directions.

By performing these two optimizations, the model was able to find the optimal parameters that resulted in stress-strain curves closely aligned with the experimental data for all the five loading protocols.

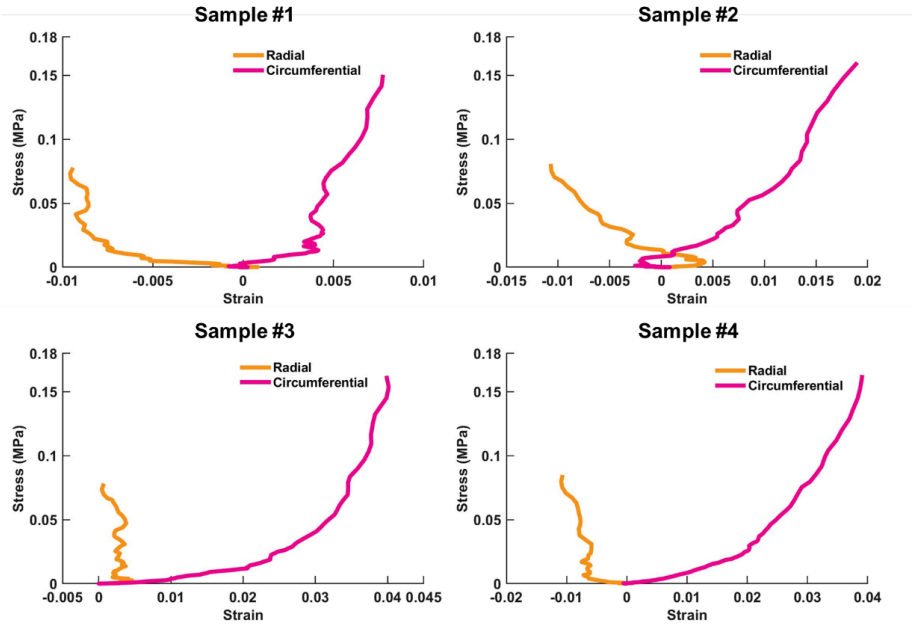

Figure 45. Stress-strain curves of the loading protocol 0.5:1 of the four samples. Under this loading condition, where the circumferential direction experienced higher stress compared to the radial direction, the radial direction of the sample exhibited a contraction, leading to negative strains.

Preliminary analysis: During the preliminary analysis of the inverse fitting procedure using Sample #1, it was observed that the experimental data from loading protocol 0.5:1 exhibited negative strains along one loading direction. This suggested the presence of anisotropic mechanical

properties, with one loading direction being much softer than the other direction. When assigning negative strains to the direct fiber model, it led to instability in the model. As a result, all the loading protocols that showed negative strains were excluded from the analysis. Based on the mechanical testing results, the loading protocol 0.5:1 of all the samples presented negative strains (Figure 45). Therefore, the results related to loading protocol 0.5:1 were not reported in this study. The focus was placed on the remaining loading protocols that did not exhibit negative strains.

6.3 Results

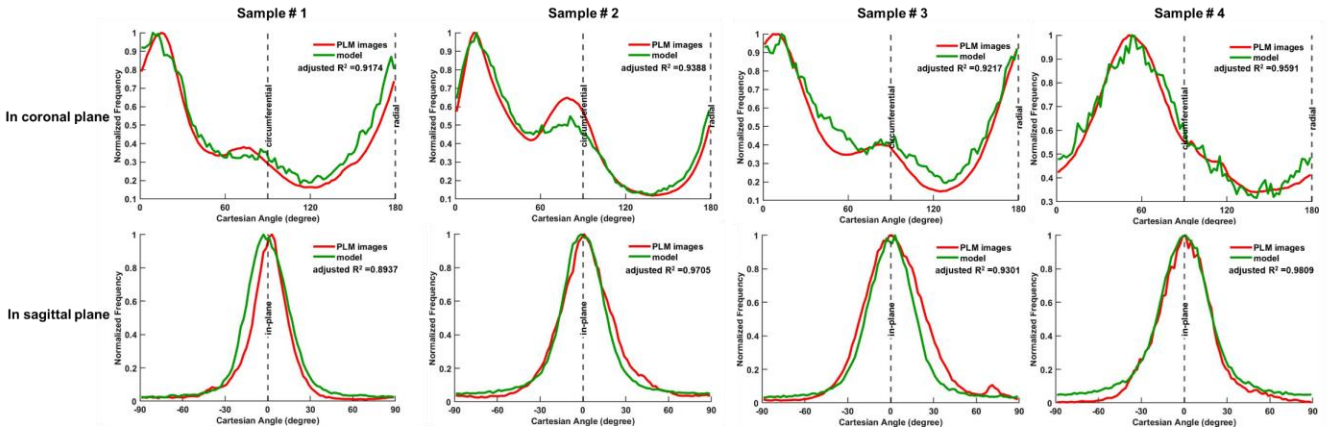

Figure 46. Fiber orientation distributions of the direct fiber model (green lines) and the corresponding PLM images (red lines).The analysis was performed in both the (top row) coronal and (bottom row) sagittal planes of the four samples. In the coronal plane, the PLM orientation was determined by analyzing a stack of all coronal images, with the radial direction represented by 0 and 180°, and the circumferential direction represented by 90°. The sagittal plane displayed the average orientation distribution obtained from two sections, with the in-plane direction represented by 0°. The frequencies of fiber orientations have been normalized by the total sum of frequencies for effective comparison. The results demonstrate a strong agreement between the fiber orientation distributions of the direct fiber model and those observed in the

PLM images, in both the coronal and sagittal planes. All the adjusted R^2 values, which exceeded 0.89, indicate a high level of similarity between the model and experimental data.

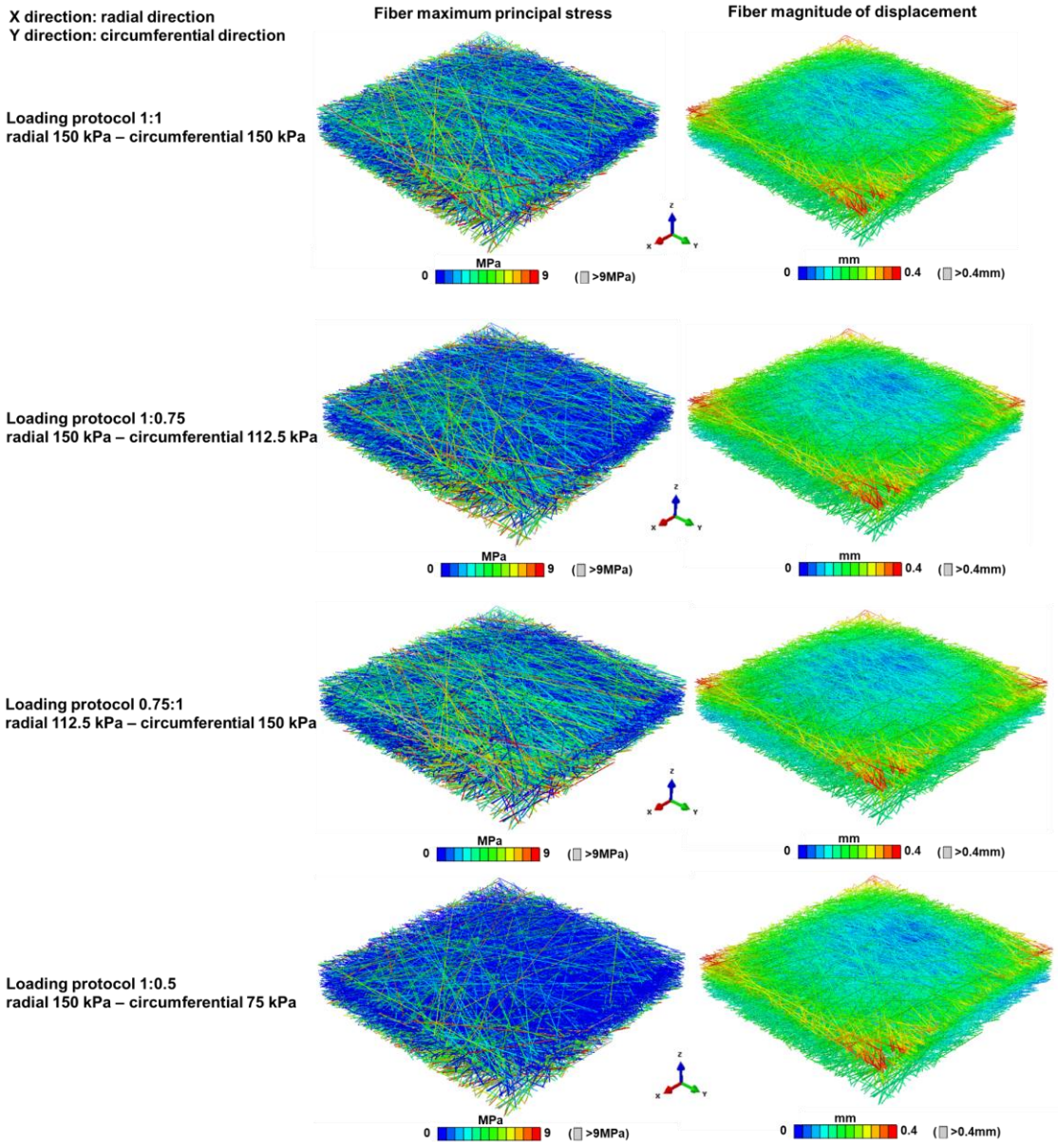

Figure 47. Isometric views of the direct fiber model of Sample #4 at full stretch. The visualization was enhanced by coloring the fibers based on two important mechanical parameters: the maximum principal stress (shown in the left column) and the magnitudes of displacement (shown in the right column) for each loading protocol. The variations in stress and displacement patterns can be observed, highlighting the non-uniform distribution of stresses and displacements within the tissue.

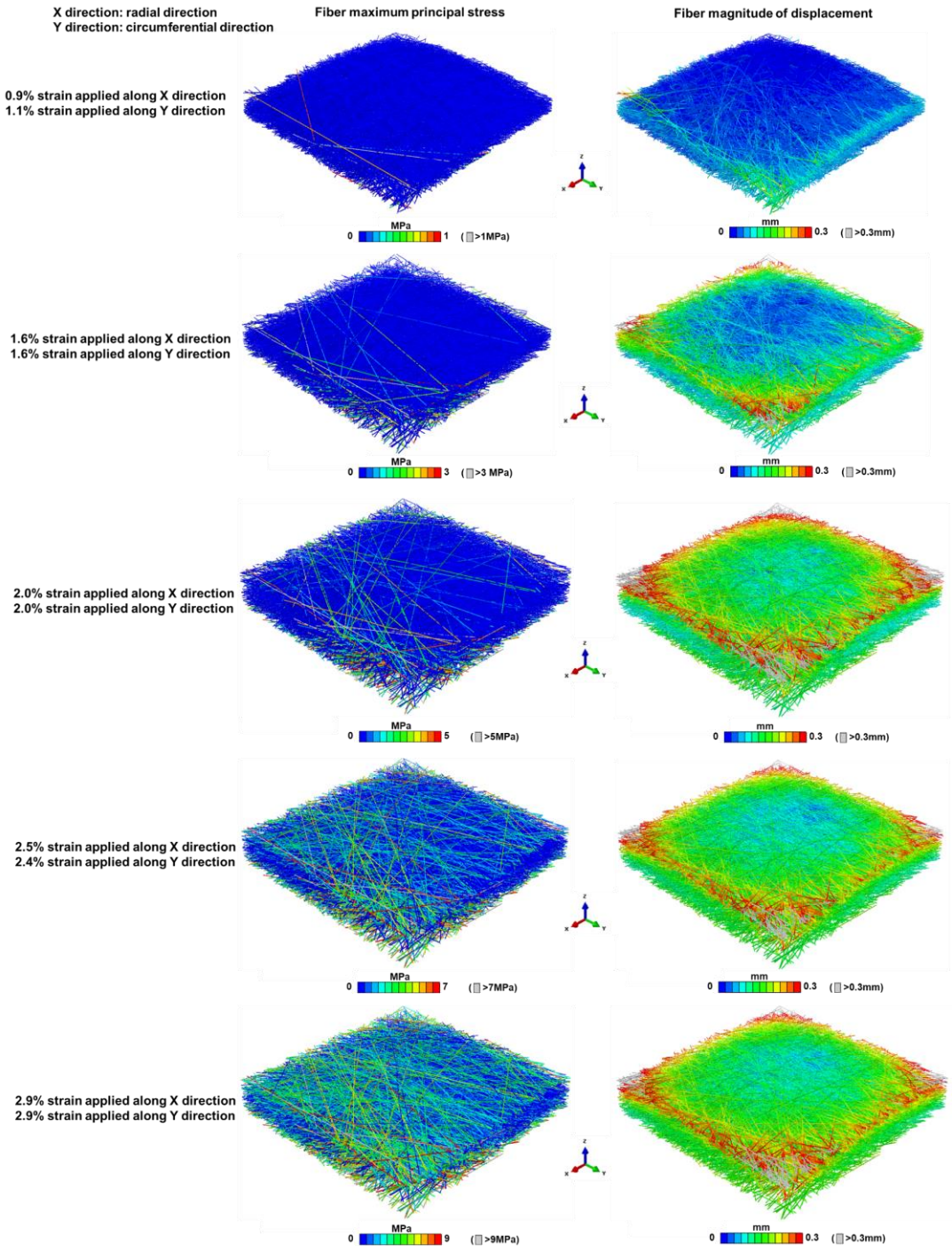

Figure 48. Isometric views of the direct fiber model of Sample #4 at different stages of the simulation while undergoing loading protocol 1:1.The visualization was colored based on the maximum principal stress (left column) and the magnitudes of displacement (right column). In the early stage of the simulation, the model exhibited some curvature. As it underwent stretching, the model gradually transformed into a flattened configuration. As stretching was applied, a larger number of fibers experience higher levels of stress.

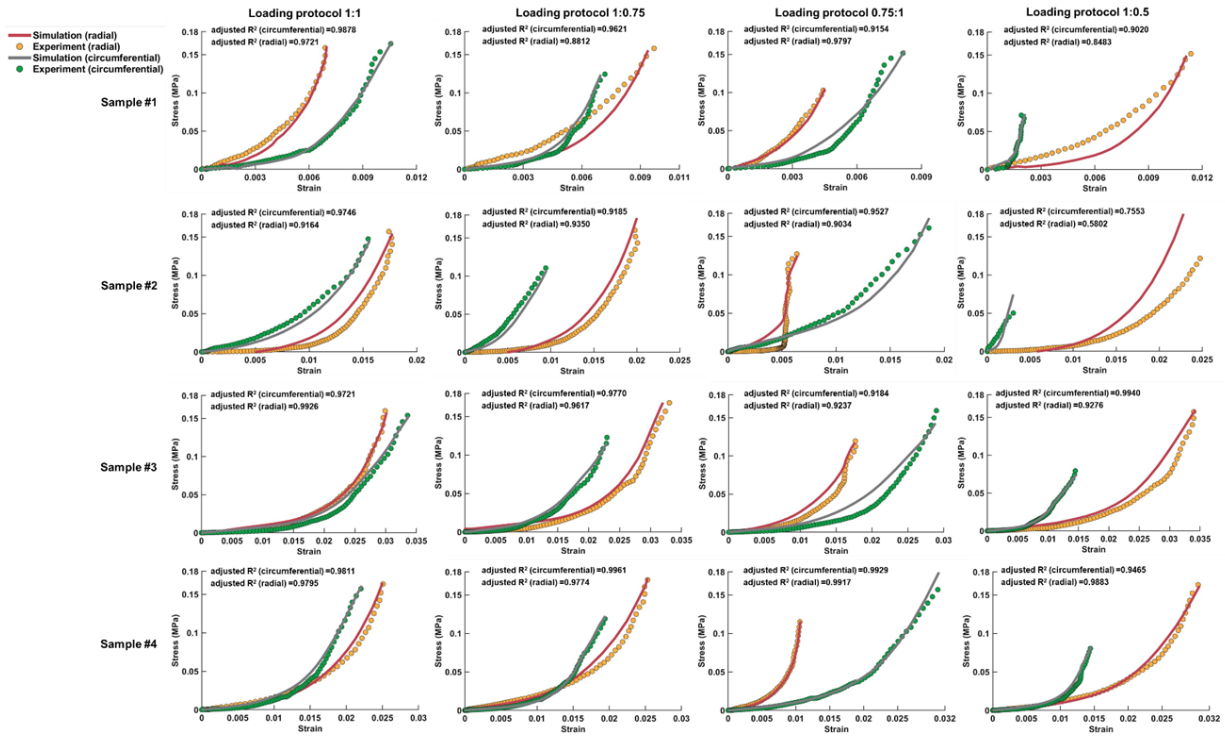

Figure 49. Stress-strain responses of the fiber-matrix assembly and the corresponding experimental data. The stress-strain curves were presented for both the radial and circumferential directions in each of the loading protocols. The fiber material properties were determined by fitting the model to the stress-strain data of loading protocol 1:1 (first column). These derived material properties were subsequently utilized directly for the inverse fitting in other loading schemes. The results demonstrated a successful fit between the model and the experimental data, with consistent agreement achieved simultaneously in both the radial and circumferential directions for each loading protocol. The goodness of fit was quantified using the adjusted R^2 value, which exceeded 0.9 in most of the cases. Notably for each sample, the stress-strain responses were obtained using the same fiber material properties throughout the simulations, with the variations observed solely in the pre-stretching strains.

Figure 46 presented the fiber orientation distributions of the direct fiber model and corresponding PLM images for the four samples. The agreement between the model and PLM images was observed in both the coronal and sagittal planes. The alignment of these orientation

curves yielded adjusted R^2 values exceeding 0.89 in all cases, indicating a strong match between the model and experimental data.

Figure 47 showed fiber displacements and stresses at full stretch of an example sample (Sample #4). The visualization revealed heterogeneous behaviors of the fibers, with varying deformations and stress distributions at the microscale. The model effectively captured the non-uniform response of the fibers under applied loading conditions, highlighting the intricate mechanical behavior within the tissue.

Table 5. The optimized fiber material properties (C_{10} and C_{01}) and the pre-stretching strains along radial and circumferential directions.

Sample#	Loading protocol#	C_{10}	C_{01}	Pre-stretching strain (radial)	Pre-stretching strain (circumferential)	Fiber elastic modulus (GPa)
1	1:1	4030	-2.0150	0.00825	0.00475	23.97
	1:0.75			0.00600	0.00725	
	0.75:1			0.00950	0.00750	
	1:0.5			0.00450	0.01050	
2	1:1	542.7	-0.1740	0.00050	0.00775	3.22
	1:0.75			0	0.01	
	0.75:1			0.01000	0.00625	
	1:0.5			0	0	
3	1:1	78.98	-0.0058	0	0.00400	0.47
	1:0.75			0	0.01100	
	0.75:1			0.01	0.01000	
	1:0.5			0	0.01350	
4	1:1	86.20	-0.0485	0.00410	0.00740	0.51
	1:0.75			0.00600	0.00510	
	0.75:1			0.01300	0	
	1:0.5			0.00150	0.00550	

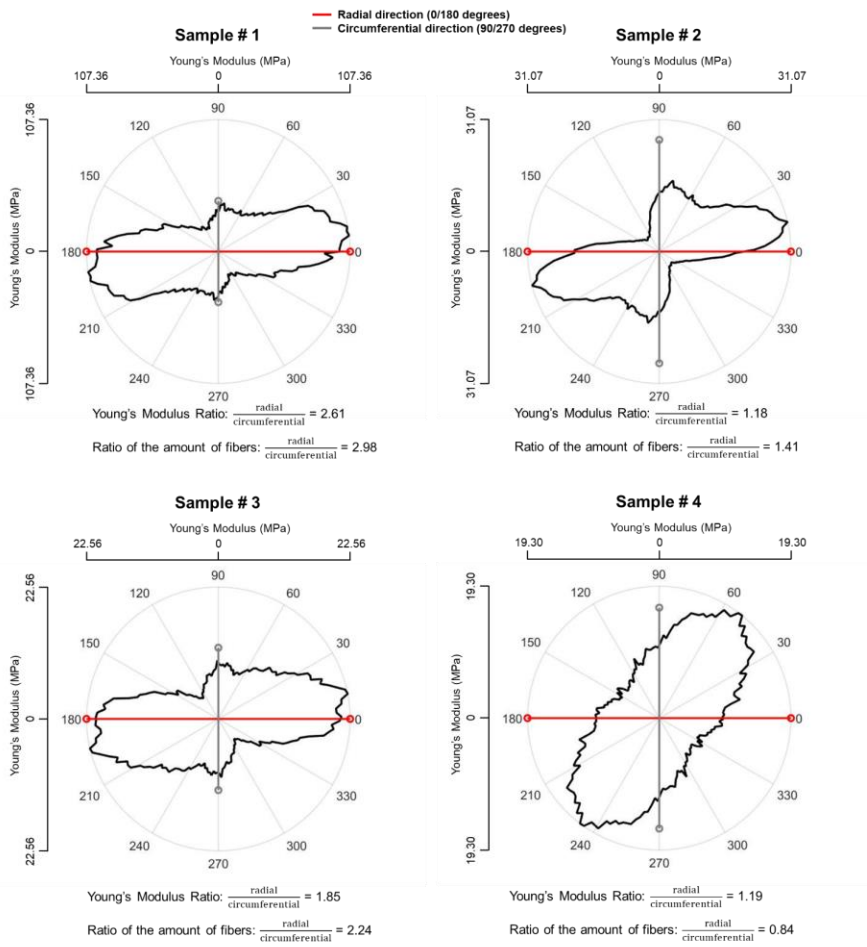

Figure 50. Orientation distribution and mechanical anisotropy of all the models.The orientation distributions are depicted in polar plots. Young's modulus of each sample was estimated by calculating the slope of the model's stress-strain curve at maximum strain state. The results indicate that at maximum strain state, the stiffness along each direction is approximately, but not exactly proportional to the amount of fibers aligned in the loading direction.

Figure 48 showed isometric views of the Sample #4 direct fiber model during loading protocol 1:1. The visualization used color to represent the maximum principal stress (top row) and displacement magnitudes (bottom row). Initially, the model showed curvature, which gradually flattened during stretching. More fibers experienced higher stress as stretching was applied.

Figure 49 showed the stress-strain curves of the optimized models, showcasing the excellent agreement with experimental data in both the radial and circumferential directions for most of the loading protocol cases. The majority of adjusted R^2 values exceeded 0.9, indicating a robust fit between the model predictions and experimental observations. The derived parameters that achieved this high level of agreement were provided in Table 5.

Figure 50 presented the fiber orientation distributions of the direct fiber model and the model's mechanical anisotropy at maximum strain state. The findings suggest that the stiffness along each direction is approximately proportional to the amount of fibers in the loading direction at the maximum strain state.

6.4 Discussion

Our goal was to enhance the analysis of the direct fiber modeling technique and perform a comprehensive validation. We developed direct fiber models to simulate four sclera samples, incorporating specimen-specific three-dimensional fiber orientation distributions. Subsequently, we conducted an inverse fitting study and matched the models with specimen-specific anisotropic stress-strain behaviors, derived from biaxial testing experiments. This study yielded two major findings. First. the direct fiber models successfully captured the collagen structure of multiple sclera samples from different quadrants and eyes. Second, the macroscopic mechanical properties of the models matched with the experimental stress-strain data obtained under various anisotropic loading conditions. Notably, the direct fiber models inherently incorporated the anisotropy of tissue mechanical behaviors within their fiber structure, thereby eliminating the necessity for separate optimization with different loading conditions. This indicated that the fiber material

properties obtained by fitting one loading condition enable the model to accurately represent the behaviors under other loading conditions as well. Below we discussed the two findings in detail.

6.4.1 The Direct Fiber Models Can Accurately Capture The Collagen Fiber Structure Across Different Samples

In our previous study, the primary focus was on introducing the direct fiber modeling methodology, which involved utilizing experimental data from different samples and species obtained for other research purposes (Ji, Bansal et al. 2023). In this study, we deliberately chose to construct models that simulate multiple sclera samples from different quadrants and eyes. This decision was driven by the fact that the collagen fiber architecture of the sclera varies both spatially within different locations and between different eyes (Gogola, Jan et al. 2018). Furthermore, it is known that the mechanical behaviors of the sclera exhibit varying degrees of anisotropy across different quadrants, such as superior and temporal quadrants (Coudrillier, Boote et al. 2013, Hua, Quinn et al. 2022). By employing samples from both superior and temporal quadrants of multiple eyes, our study successfully demonstrated the robustness of the direct fiber modeling approach in capturing the varying fiber structure as well as the anisotropic stress-strain behaviors. It is important to emphasize that our models were specimen-specific, meaning that the fiber structure was individually constructed based on each sample, and the model's behaviors were optimized using experimental data obtained from the same sample. The results of this study proved a high level of accuracy and reliability of direct fiber modeling in representing real tissue microstructures and properties.

6.4.2 The Macroscopic Mechanical Properties Of The Models Matched With The Experimental Stress-Strain Data Obtained Under Various Anisotropic Loading Conditions

In our previous study, we constructed a single model and validated it against a specific equi-biaxial experimental dataset. In this study, we specifically opted to match the stress-strain behaviors under different loading conditions, taking into account the fact that the sclera is subjected to complex loading conditions (Boote, Sigal et al. 2020). This study enables the inclusion of these more intricate loading conditions, ensuring the validity of the model under such complex scenarios. It is worth noting that achieving validity by simultaneously matching multiple loading conditions has not been extensively accomplished in many previous studies, despite their attempts to utilize inverse fitting techniques to optimize the model and align it with experimental data (Coudrillier, Pijanka et al. 2015, Karimi, Rahmati et al. 2022). Thus, our study distinguishes itself by successfully addressing this challenge and demonstrating the direct fiber model's capability to accurately represent the sclera's mechanical responses under diverse and complex loading conditions.

6.4.3 The Direct Fiber Models Inherently Incorporate The Anisotropy Of Tissue Mechanical Behaviors Within Their Fiber Structure

We gave this conclusion based on the derivation of fiber material properties through fitting the equi-biaxial loading condition. By utilizing the optimized fiber material properties directly, the direct fiber model can accurately represent the mechanical behaviors of the sclera under other loading conditions as well, exhibiting a strong overall fit (adjusted $R^2 > 0.9$). We postulate that the

direct fiber modeling should have captured the tissue collagen microstructure in a very accurate way since collagen fibers serve as the primary load-bearing component of the sclera (Girard, Downs et al. 2009, Coudrillier, Pijanka et al. 2015). Therefore, the introduction of specimen-specific mechanical anisotropy becomes a natural outcome when designing the geometric arrangement of collagen fibers within the model. This is an advantage of the direct fiber modeling approach because the material properties derived from fitting a single loading protocol can be considered as optimal properties applicable to complex loading conditions. In contrast, previous approach required optimizing the model across all loading conditions to obtain the ideal material properties (Thomas, Lai et al. 2019). Our method significantly streamlines the process of determining tissue mechanical properties, making the direct fiber modeling technique more efficient and effective.

6.4.4 Advantages And Optimization Of The Procedure For Building Direct Fiber Model Structures

The models developed in this study inherited several advantages that we discussed previously. Briefly, the direct fiber models have considered fiber interweaving and the resulting fiber-fiber interactions that play an important role in determining the structural stiffness of the sclera (Wang, Hua et al. 2020). The models also have included collagen fibers of the sclera that are long and continuous. Thus, they can transfer forces over a long distance (Voorhees, Jan et al. 2018, Boote, Sigal et al. 2020), where it's commonly recognized that it's important to account for long fiber mechanics (Huang, Zhou et al. 2017, Lanir 2017, Grytz, Yang et al. 2020, Islam, Ji et al. 2023). Furthermore, the direct fiber models have considered three-dimensional specimen-specific collagen architecture, whereas previous fiber-aware models tend to overlook or simplify

the in-depth orientations of the collagen fibers (Coudrillier, Boote et al. 2013, Zhang, Albon et al. 2015, Voorhees, Jan et al. 2017). Collagen fiber variations in-depth of the tissue are crucial in determining the sclera's load-bearing capacity, particularly in bearing shear stresses, and may have clinical implications (Danford, Yan et al. 2013).

In comparison to our preliminary study, we implemented two optimizations to the approach when building direct fiber model structures. Firstly, we incorporated the natural curvature of the tissue into the model, enabling a more accurate representation of the physiological shape of the sclera. This enhancement ensured that the model closely mimicked the three-dimensional geometry of the sclera, improving its realism and fidelity. Secondly, in order to address the issue of fibers that were supposed to be tightly interwoven but were actually floating within the structure, we introduced a constraint function in Abaqus. This constraint function served to tightly constrain the interconnections between fibers. As a result, the model not only exhibited increased stability, but also better matched the actual interweaving and cohesion of collagen fibers in the sclera. This optimization helped overcome the challenge of inaccuracies caused by floating fibers and enhances the model's reliability and validity in representing the real tissue structure.

6.4.5 Interpretation Of The Derived Fiber Material Properties

In our study, we initially derived the fiber material properties by matching the experimental data of loading protocol 1:1. Concerns may arise regarding the validity of the direct fiber modeling technique if different fiber material properties are obtained when matching experimental data from other loading protocols. To address this concern, we randomly selected a sample and derived the fiber material properties by independently fitting the loading protocols 1:0.75, 0.75:1, and 1:0.5. The fiber material properties were initially assigned random values and iteratively optimized to

match the experimental data. Importantly, the fitting processes were performed without any reference to the results obtained from other loading schemes. Interestingly, we observed that the derived fiber material properties from fitting different loading protocols fell within a similar range, as indicated in Figure 51. To further evaluate the physical significance of these properties, we examined the resulting fiber elastic modulus and bulk modulus. Remarkably, these two properties demonstrated consistency across the results obtained from fitting different loading protocols. These findings demonstrate the robustness of our method and confirm that the derived material properties are independent of the choice of loading protocols for fitting.

Loading protocol #	C_{10}	C_{01}	Pre-stretching strain (radial)	Pre-stretching strain (circumferential)	Fiber elastic modulus (GPa)	Fiber bulk modulus (GPa, $2(C_{10} + C_{01})$)
1:1	86.20	-0.049	0.0041	0.0074	0.512	0.172
1:0.75	97.601	-0.976	0.0045	0.005	0.574	0.193
0.75:1	77.729	-0.777	0.0135	0	0.457	0.154
1:0.5	86.625	-1.055	0.002	0.005	0.508	0.171

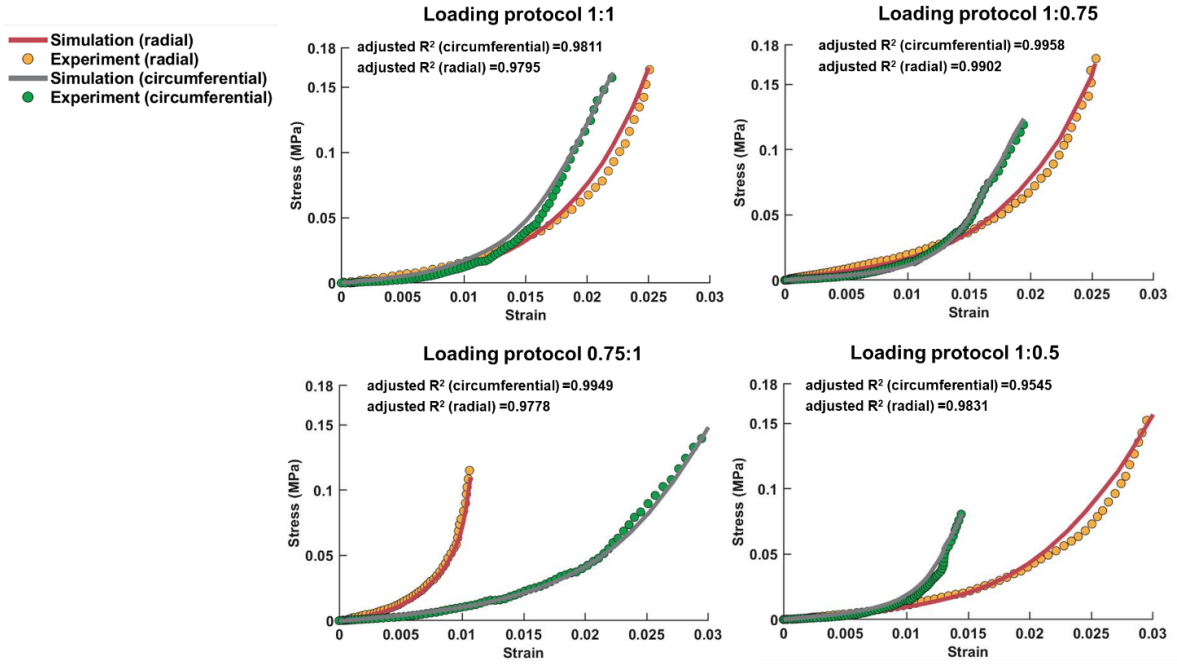

Figure 51. This figure illustrates the findings from the analysis using Sample #4 to assess the similarity of derived material properties when fitting the model to experimental data from different loading protocols.The table demonstrates that the values of C_{10} and C_{01} derived from fitting the model to different loading protocols are closely aligned, resulting in comparable fiber elastic modulus and fiber bulk modulus. Additionally, the

stress-strain curves between the model and experimental data exhibit a strong overall fit, with an adjusted R^2 greater than 0.9. These results support the conclusion that the choice of loading protocol for fitting does not influence the derived fiber material properties.

The uniqueness of optimal parameters is a common concern in inverse fitting techniques (Girard, Downs et al. 2009, Zhou, Abass et al. 2019). To address this concern, we conducted the inverse fitting process using four different sets of starting parameters to assess the consistency and uniqueness of the results. The derived fiber material properties, C_{10} and C_{01}, exhibited significant variation among the four samples. To better understand those values which are lack specific physical interpretation, we further estimated the elastic modulus of individual fibers by simulating uniaxial stretch of a single straight fiber with the optimal C_{10} and C_{01} values of the hyperelastic Mooney-Rivlin material. The estimated fiber elastic modulus ranged from 0.47 GPa to 23.94 GPa, and the detailed values can be found in Table 5. This wide range of values aligned with the experimentally reported elastic modulus values found in the literature, which ranged from 0.2 GPa to 7 GPa in bovine Achilles tendon fibers (Van Der Rijt, Van Der Werf et al. 2006, Yang, Van Der Werf et al. 2007), and 5 GPa to 11.5 GPa in rat tail (Wenger, Bozec et al. 2007). It is worth noting that one value falled outside this range, which we believe may be attributed to two factors. Firstly, the load was primarily borne by a small portion of the fibers, leading to an overestimation of the fiber material properties. Secondly, the volume fraction of the models in this study was approximately 15%, which may not accurately represent the actual tissue composition. The estimated fiber material properties were closely associated with the designed fiber volume fraction in the model. Further research is necessary to comprehensively understand how variations in fiber volume fraction influence the behavior and derived material properties of the direct fiber model.

Another concern pertaining to the derived material properties and pre-stretching strains is the possibility of achieving an excessively favorable match between the models and experimental data across all loading schemes. To address this concern, we conducted a specific analysis using the fiber structure of Sample #1 and attempted to match the experimental data of sample #2. The results revealed that we could successfully match the experimental data for loading protocols 1:1, 1:0.75, and 0.75:1. However, when attempting to match the experimental data for loading protocol 1:0.5, the model could not achieve a satisfactory fit (Figure 52). This outcome indicates that the model is not universally applicable but rather depends on accurately matching the orientation distribution of the sample in order to replicate the experimental data of that specific sample.

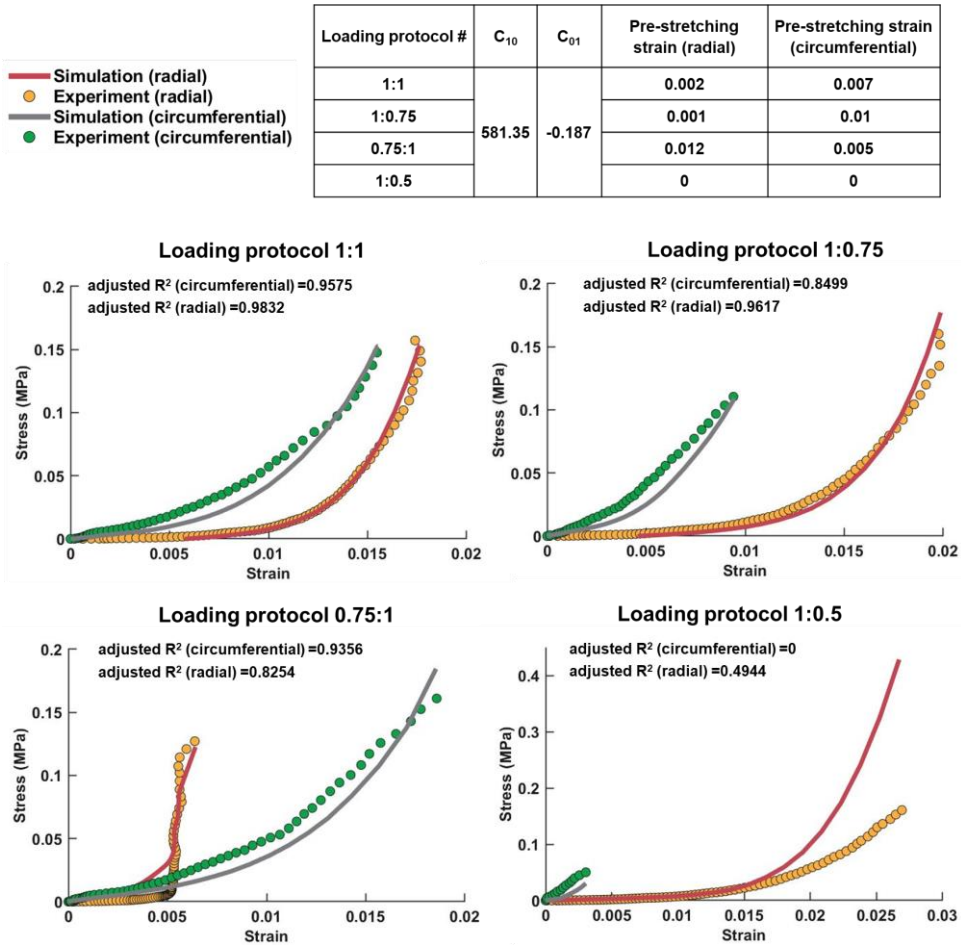

Loading protocol #	C_{10}	C_{01}	Pre-stretching strain (radial)	Pre-stretching strain (circumferential)
1:1	581.35	-0.187	0.002	0.007
1:0.75			0.001	0.01
0.75:1			0.012	0.005
1:0.5			0	0

Figure 52. This figure presents the results of using the model fiber structure of Sample #1 to fit the experimental stress-strain data of Sample #2, aimed at assessing the possibility of achieving an overly favorable match between the models and experimental data. Following the process described in the main text, the fiber material properties C_{10} and C_{01} were derived by fitting the model to loading protocol 1:1. The results indicate successful matches between the model and experimental data for loading protocols 1:1, 1:0.75, and 0.75:1, with overall adjusted R^2 values exceeding 0.8. However, for loading protocol 1:0.5, the model exhibits softer behavior than the experiment in the circumferential direction and stiffer behavior in the radial direction, resulting in adjusted R^2 values lower than 0.5. As such, it cannot be considered as a valid match. These findings reinforce that the model's applicability is not universal but rather dependent on accurately matching the orientation distribution of the specific sample in order to replicate its experimental data.

6.4.6 Limitations

The first limitation was observed in the matching of stress-strain curves between the model and experimental data. While the majority of loading conditions exhibited strong agreement with adjusted R^2 values exceeding 0.9, there were instances, particularly in the loading protocol 1:0.5, where the model's fit was relatively lower. This discrepancy may be attributed to the sequential application of five different loading protocols during the testing process. After multiple rounds of testing, the tissue may become softer than its original condition. As a result, the model's behavior appeared to be stiffer than the corresponding experimental data in these cases. Despite this limitation, it is important to emphasize that the direct fiber modeling technique demonstrated robustness and effectiveness in capturing the overall mechanical behaviors of the sclera, as evidenced by the strong agreement between the model and experimental data in the majority of the cases. The observed discrepancies in certain loading conditions provide valuable insights for future refinements of the model and highlight the need for further investigation into the dynamic changes in tissue properties during sequential loading.

Second, we encountered difficulties in accurately matching the loading protocol 0.5:1 due to the model's inability to perform well under compression. This limitation indicated that further optimization of the approach was required to enable stable simulations under compression loading conditions. Future efforts should be focused on addressing this issue to enhance the applicability of the direct fiber modeling approach. By improving the model's performance in compression scenarios, we can broaden its utility in studying the mechanical behaviors of the sclera across a wider range of loading conditions.

Third, our study only used sheep eyes as the sample model, without validation using other animal models or human eyes. Considering the robustness of the approach in capturing the

complex fiber structure and anisotropic mechanical behaviors of sheep sclera, we anticipated that the direct fiber modeling technique can serve as a valid and effective tool for investigating scleral biomechanics in other species and potentially in other collagen-based tissues as well. Future studies can extend the application of this approach to validate its broader utility and ensure its generalizability across various biological tissues.

Fourth, the direct fiber models, while consistent with experimentally measured fiber orientation distribution, are still approximations of the actual tissue. Several aspects were simplified or ignored in the modeling process, which may introduce discrepancies between the models and the real tissue. One such simplification was the assumption of uniform fiber or bundle diameters within the models. In reality, collagen fibers in the sclera can exhibit variations in diameter (Komai and Ushiki 1991). Additionally, sub-fiber level features were not explicitly included in the models, such as fiber crimp (Grytz, Fazio et al. 2014). Future work would benefit from incorporating more detailed and realistic microstructural features, where the models can provide a more accurate representation of the scleral tissue and enhance our understanding of its mechanical behaviors.

Fifth, the matrix mechanical properties were kept constant at literature values and not optimized iteratively like the fiber properties. This simplification was made for simplicity. Although the matrix properties could potentially affect fiber load-bearing and parameter fitting, their impact is considered minor. The fibers, being the primary load-bearing component, exhibit significantly greater stiffness compared to the matrix (Girard, Downs et al. 2009, Coudrillier, Pijanka et al. 2015). Analysis of our model indicated that the matrix bears only 4%–6% of the total reaction forces at the maximum strain. Therefore, we believe that the fiber properties predominantly influence the model's behavior, while the matrix stiffness has minimal influence on

the derived parameters. In future work, it would be worthwhile to explore the role of matrix properties and consider more detailed matrix-fiber interactions for further refinement.

Sixth, we ignored fiber-matrix interactions and considered simplified fiber-fiber interactions, similar to our previous work (Ji, Bansal et al. 2023). However, it should be noted that the interactions between fibers and the matrix can be much more complex and may influence the tissue behaviors (Murienne, Chen et al. 2016, Hatami-Marbini and Pachenari 2020). Future research could benefit from incorporating more realistic and complex interactions within the direct fiber modeling framework. The direct fiber modeling technique has the potential to be a valuable tool for studying and considering such complex interactions in future studies.

In conclusion, we performed a comprehensive validation of the direct fiber modeling approach through the simulation of multiple sheep posterior sclera samples. We characterized the macroscopic and anisotropic stress-strain behaviors of the samples through biaxial mechanical testing. Then direct fiber models were generated based on the microstructural architecture of each sample. An inverse fitting process was employed to simulate biaxial stretching conditions, enabling the determination of optimal pre-stretching strains and fiber material properties. Our findings demonstrated the efficacy of the direct fiber modeling approach in simulating the scleral microarchitecture, capturing critical fiber characteristics, and accurately describing its anisotropic macroscale mechanical behaviors. Moreover, we highlighted the capability of the direct fiber models to inherently incorporate the anisotropy of tissue mechanical behaviors within their fiber structure. Overall, the direct fiber modeling approach proved to be a robust and effective tool for characterizing the biomechanics of sclera.

7.0 Dissertation Conclusions

7.1 Summary

In this study, we investigated two critical collagen microstructural features with significant implications for glaucoma research: LC insertions and in-depth collagen fiber organization within the corneoscleral shell. Through the characterization, we quantified essential parameters related to LC insertions, including insertion width, insertion angle, number of insertions, and insertion ratio. Additionally, we quantified the in-depth collagen fiber orientation distribution, the percentage of inclined fibers and the range of inclination angles in the corneoscleral shell.

To further our understanding of tissue collagen microstructural biomechanics, we developed an innovative direct fiber modeling technique specifically tailored to simulate the collagen microstructure in fiber-based soft tissues, such as the sclera. This advanced modeling approach not only provided explicit representations of individual collagen fibers but also accurately captured the tissue's anisotropic mechanical behavior in diverse biaxial loading schemes.

7.1.1 Specific Aim 1: Characterize Variations Of LC Insertions.

1a. Characterize the variations in insertion widths and insertion angles among four different species (sheep, pig, monkey, and human).

PLM images of ONH cryosections from sheep, pig, monkey, and human eyes were acquired. Manual measurements of insertion width and insertion angle were conducted. The results

revealed significant variations in LC beam insertions among the species, with differences in shape (curved or straight), width (broad or narrow), and penetration depth (shallow or deep). The widths of the LC insertions differed significantly between all species. Insertion angles of sheep and pig were larger than monkey and human. These findings have implications for understanding the mechanics of the LC region and its impact on neural tissues, potentially shedding light on why peripheral vision is affected earlier in glaucoma. For example, our data suggest an intriguing hypothesis that monkey, with its smallest insertion widths, might be the most sensitive to changes in IOP. Similarly, humans, with relatively narrower LC insertions, could also display elevated sensitivity to IOP changes. However, it is essential to emphasize that these hypotheses are preliminary and demand careful evaluation through further research.

1b. Characterize the spatial distribution of LC insertions from the anterior to posterior LC and across the four quadrants of monkey eyes. Quantify variations in insertion width, insertion angle, number of insertions, and insertion ratio.

Coronal cryosections of the LC from six healthy monkey eyes were imaged using IPOL. LC insertions were manually marked, noting their in-depth position and quadrant. Insertion width, insertion angle, number of insertions, and insertion ratio were quantified. LME models were used to determine if these parameters were associated with in-depth position or quadrant. The results showed significant variations in LC insertions over the canal. The anterior LC had sparser, narrower, and more slanted insertions compared to the middle and posterior LC. Additionally, insertion angles were significantly smaller in the nasal quadrant. The sparser, narrower and more slanted insertions of the anterior LC may not provide the robust support afforded by insertions of

the middle and posterior LC. These findings suggest that the variations in LC insertions may contribute to the progressive deepening of the LC and the regional susceptibility to glaucoma.

7.1.2 Specific Aim 2: Characterize In-Depth Collagen Organization In The Corneoscleral Shell.

2a. Quantify in-depth fiber orientation distributions and anisotropy around the corneoscleral shell. Test if the orientation distributions could be accurately summarized with a combination of a uniform distribution and a sum of π-periodic von Mises distributions.

Seven sheep whole-globe sagittal sections from eyes fixed at an IOP of 50 mmHg were imaged using PLM to measure collagen fiber orientations and density. In-depth fiber orientation distributions and anisotropy (degree of fiber alignment) accounting for fiber density were quantified in 15 regions: central cornea, peripheral cornea, limbus, anterior equator, equator, posterior equator, posterior sclera and peripapillary sclera on both nasal and temporal sides. Our measurements showed that the fibers were not uniformly in-plane but exhibited instead a wide range of in-depth orientations, with fibers significantly more aligned in-plane in the anterior parts of the globe. We found that fitting the orientation distributions required between one and three π-periodic von Mises distributions with different primary orientations and fiber concentration factors. These variations in orientation distributions and anisotropies imply the presence of diverse out-of-plane tissue mechanical properties around the eye globe, highlighting the importance of considering the three-dimensional nature of collagen fiber orientations for a comprehensive understanding of corneoscleral shell biomechanics. Additionally, the substantial out-of-plane fibers suggest the presence of the large number of inclined fibers. In the cornea, such inclined fibers play a crucial role in enhancing stiffness and controlling the shape of the cornea. Therefore,

it is reasonable to infer that out-of-plane fibers likely contribute to the stiffness and shape of the rest of the globe as well, necessitating careful consideration.

2b. Quantify fiber inclination in the corneoscleral shell, characterized by the percentage of fibers that are inclined-not parallel to sclera surface, and the range of inclination angles (half width at half maximum of inclination angle distribution).

Among the 15 regions around the corneoscleral shell that we analyzed, we observed that regions of the posterior globe, particularly on the temporal side, exhibited a larger percentage of inclined fibers and a broader range of inclination angles compared to anterior and equatorial regions. The anisotropic distribution of fiber inclinations in the corneoscleral shell suggests that the different regions may respond differently to mechanical loads. Regions with less inclined fibers may demonstrate more fibers loaded in-plane during inflations. Conversely, regions with more inclined fibers may experience increased bending. Moreover, the substantial presence of inclined fibers implies a higher occurrence of interlocking patterns in the collagen structure. This feature may potentially enhance the overall mechanical strength, stiffness, and stability of the region, similar to the effects found in textiles and in cornea. The interlocking effect allows fibers to distribute forces more effectively, contributing to the eye's structural integrity and biomechanical robustness. Understanding these characteristics is crucial for gaining insights into the mechanical behavior of the corneoscleral shell and its potential implications in ocular biomechanics.

7.1.3 Specific Aim 3: Develop And Validate The Direct Fiber Modeling Technique For Posterior Sclera.

3a. Develop the methodology of direct fiber modeling capable of simulating the specimen-specific 3D collagen fiber architecture of sclera. Utilize an inverse fitting approach to estimate the model's fiber mechanical properties.

We developed the direct fiber modeling technique to represent the collagen architecture explicitly, using long, continuous, and interwoven fibers embedded in a continuum matrix representing non-fibrous tissue components. The model's fiber structure was validated using PLM data from pig and sheep corneoscleral sections. The fibers were described by a Mooney-Rivlin model, while the matrix was modeled using a Neo-Hookean model. By inversely matching experimental equi-biaxial tensile data from the literature, we determined the fiber parameters (C_{10}=5746.9 MPa; C_{01}=-5002.6 MPa) and the matrix shear modulus (200 kPa). The reconstructed model's fiber orientations agreed well with the microscopy data in both coronal and sagittal planes of the sclera. The model successfully fit experimental stress-strain curves in both radial and circumferential directions, revealing sub-fiber level stresses and strains during stretch, including interactions among individual fibers not captured by conventional continuum methods. Our results demonstrate that direct fiber models can simultaneously describe the macroscale mechanics and microarchitecture of the sclera, providing unique insight into tissue behavior not accessible through continuum approaches.

3b. Validate the direct fiber modeling approach by simulating collagen microstructures of multiple sclera samples. Determine, by inverse fitting, the fiber material properties that allow the models to

accurately replicate the anisotropic mechanical behaviors observed in multiple biaxial loading schemes.

We validated the direct fiber modeling approach using four sheep posterior sclera samples. By employing a biaxial mechanical testing method with five different loading protocols, we characterized the macroscopic and anisotropic stress-strain behaviors of the samples. Subsequently, we generated direct fiber models based on the microstructural architecture of each sample, which was obtained through PLM. By employing an inverse fitting process, we simulated the biaxial stretching boundary conditions to determine the optimal pre-stretching strains and fiber Mooney-Rivlin material properties that could simultaneously match the experimental data from all loading protocols. Our findings demonstrated the robustness of the direct fiber modeling technique in accurately representing specimen-specific collagen fiber orientation distributions across different samples. Furthermore, the model's behaviors can match the anisotropic mechanical behavior exhibited in different loading protocols and across all the samples. Notably, the model naturally accounted for the tissue's anisotropic behaviors within its fiber structure. By fitting equi-biaxial stress-strain data, the model derived fiber material properties and matched experimental stress-strain behavior under non-equi-biaxial conditions. These results demonstrate the efficacy of the direct fiber modeling approach in simulating scleral microarchitecture and describing anisotropic macroscale mechanical behavior. The technique offers valuable insights into the scleral biomechanical environment and its response to mechanical loadings.

7.2 Future Work

7.2.1 LC Insertions

In-depth analysis of the spatial variations of LC insertions should be performed in all four species (sheep, pig, monkey, and human) to comprehensively understand the unique features of LC insertions in patients, and in the most commonly used animal models. This comprehensive investigation will provide valuable insights into the species-specific biomechanical differences and help build a more robust understanding of LC biomechanics and sensitivity to glaucoma.

Additionally, it is essential to explore the potential differences in LC insertions between glaucoma and healthy eyes. Investigating whether the parameters of LC insertions could serve as diagnostic criteria to predict glaucoma onset or identify eyes more susceptible to the disease will be of significant clinical importance. Even if at this point the LC insertions remain out of reach of in-vivo imaging, understanding the link between LC insertions and glaucoma progression can potentially lead to early detection and personalized treatment strategies. Tools for in-vivo imaging are progressing rapidly (Sigal, Wang et al. 2014), and it seems plausible that tools could be developed to visualize LC insertions, particularly if they are demonstrated to be critical in glaucoma.

Furthermore, to gain deeper insights into the biomechanics of LC insertions, more in-depth studies are required to explore the mechanical implications of insertion width, insertion angle, number of insertions, and insertion ratio. The direct fiber modeling approach can play a pivotal role in this exploration, offering the ability to simulate and analyze the effects of various insertion characteristics on tissue behavior under different loading conditions (Figure 53). This endeavor

will facilitate a better understanding of the biomechanical significance of LC insertions and their role in glaucoma pathogenesis.

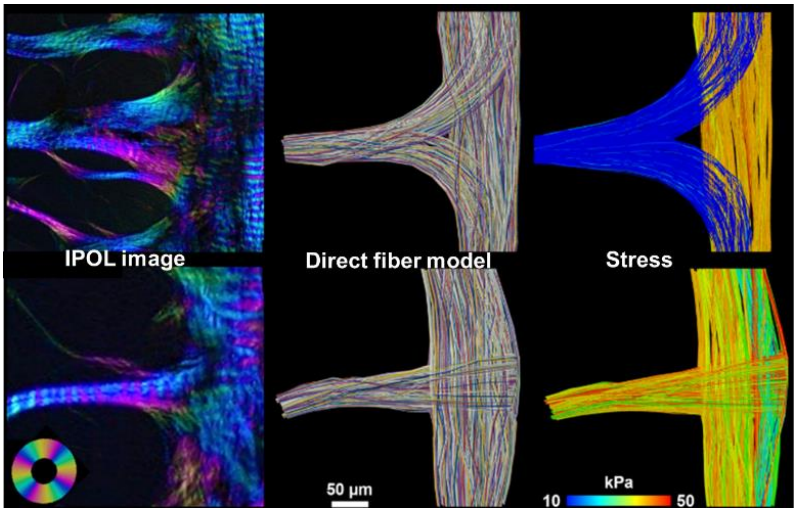

Figure 53. An example comparison of the mechanical response between a spread and wide insertion (top row) and a straight and narrow insertion (bottom row).Direct fiber models (middle column) were created by tracing collagen fibers on IPOL images (left column). The fibers were discretized with linear truss elements (T3D2) of circular cross-section and linear elastic material properties. Fiber overlaps were resolved using an iterative algorithm that refined and displaced them, resulting in discrete, interwoven realistic-looking fibers. Fiber-fiber interactions were incorporated using general contact to prevent fiber interpenetration. The solution was obtained using Abaqus/Explicit. The stress responses of fibers under 15% equi-biaxial stretch are shown (right column). The insertion with spread and wide LC beam bears substantially less load (lower stress) than the other one, illustrating that LC insertion shape has a large effect on the local sensitivity to IOP.

7.2.2 In-Depth Collagen Fiber Organization In The Corneoscleral Shell

The study of in-depth collagen fiber organization holds the potential for uncovering crucial factors influencing the macroscale biomechanics of ocular tissues. Conducting further research to investigate the role of fiber inclination and different levels of in-depth fiber anisotropy on tissue

mechanics is vital for understanding how tissue microstructure influences overall mechanical behavior. Utilizing the direct fiber modeling approach, we can introduce various degrees of fiber inclination to model the complex collagen architecture accurately. By constructing and comparing models with different combinations of inclined fiber percentages and ranges of inclination angles, the study can unveil how these microstructural variations impact the tissue's mechanical response under various loading conditions. This comprehensive analysis will provide deeper insights into the mechanics of the corneoscleral shell, offering valuable information for understanding the biomechanical environment of the eye and its relevance to glaucoma development.

7.2.3 Direct Fiber Modeling

Although this dissertation has shed light on crucial aspects of direct fiber modeling, certain questions remain to be fully understood, as discussed in Section 5.4 and Section 6.4. One such area of exploration involves the disparity between fiber orientation anisotropy and tissue mechanical anisotropy. Chapter 6 presents an intriguing example of this disparity. In Sample #1 and Sample #2, despite having similar distributions of fiber orientations, their mechanical anisotropies differ. Sample #1 is stiffer along the radial direction, whereas Sample #2 is stiff along the circumferential direction. Another example is presented in Figure 50, where the stiffness of the loading direction is not precisely proportional to the amount of fibers in that direction. Investigating the underlying mechanisms responsible for this phenomenon is essential to gain deeper insights into tissue behavior and its connection to collagen microstructure.

Expanding the application of the direct fiber modeling method to study additional ocular tissue structures or larger regions in the eye represents an exciting avenue for future research. For instance, applying the direct fiber modeling approach to study the entire optic nerve head will be

a transformative step in understanding its biomechanics comprehensively. By capturing crucial microstructural mechanisms, such as fiber interactions and long-range strain transmission among bundles, the model will provide unprecedented insights into the role of fibrous collagen structure in the biomechanics of the optic nerve head. Moreover, the direct fiber modeling method holds the potential for exploring the interactions between collagen microstructure and cells within ocular tissues. By incorporating cellular behavior and responses into the model, we can further advance our understanding of how cellular activities influence the biomechanical properties of the tissues and contribute to overall ocular health.

7.3 Conclusion

This study delves into crucial collagen microstructural features with significant implications for glaucoma research: LC insertions and in-depth collagen fiber organization within the corneoscleral shell. Through comprehensive characterization, we quantified essential parameters related to LC insertions and explored intricate in-depth collagen fiber orientation distributions and fiber inclinations. To advance our understanding of tissue collagen biomechanics, we developed and validated the direct fiber modeling technique, providing explicit representations of individual collagen fibers and critical fiber characteristics, while accurately capturing anisotropic mechanical behaviors. This research significantly enhances our knowledge of the ocular tissue microstructure and biomechanical environment, offering valuable insights into the pathogenesis of glaucomatous optic neuropathy.

Appendix A In-Depth Collagen Fiber Orientation Distribution Curve Fitting Results Of All The Regions And Sections

Appendix A.1 In-Depth Orientation Distribution Curve Fitting Results Of Section #1

	a	*k*	μ(rad)	*c*
von Mises-1	0.578	0.347	1.752	-
von Mises-2	0.555	2.703	2.577	-
isotropic	-	-	-	0

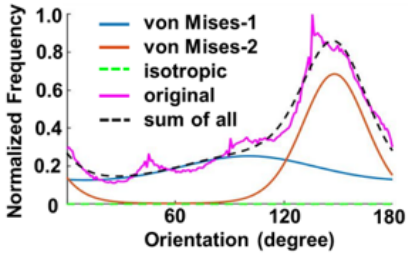

Appendix Figure 1. Curve fitting results of Section #1 nasal side PPS region.

	a	*k*	μ(rad)	*c*
von Mises-1	0.185	14.553	3.017	-
von Mises-2	0.015	67.286	2.261	-
von Mises-3	0.986	0.382	2.790	-
isotropic	-	-	-	0

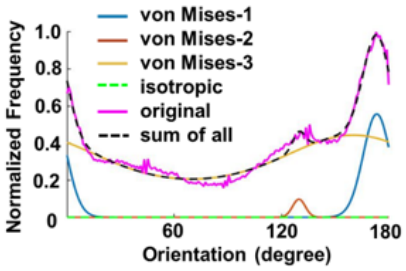

Appendix Figure 2. Curve fitting results of Section #1 temporal side PPS region.

	a	*k*	μ(rad)	*c*
von Mises	0.582	4.375	2.562	-
isotropic	-	-	-	0.019

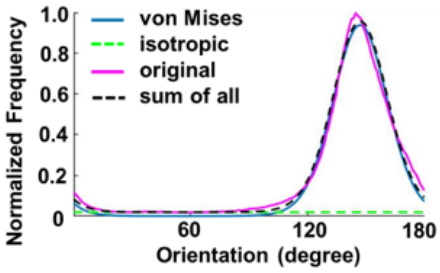

Appendix Figure 3. Curve fitting results of Section #1 nasal side posterior sclera region.

	a	*k*	μ(rad)	*c*
von Mises	0.777	2.069	2.973	-
isotropic	-	-	-	0.027

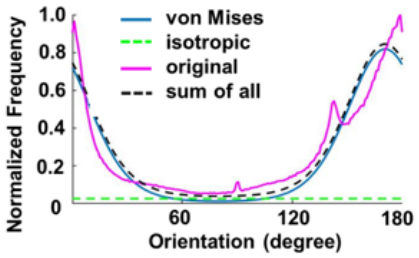

Appendix Figure 4. Curve fitting results of Section #1 temporal side posterior sclera region.

	a	*k*	μ(rad)	*c*
von Mises	0.391	9.637	2.202	-
isotropic	-	-	-	0.010

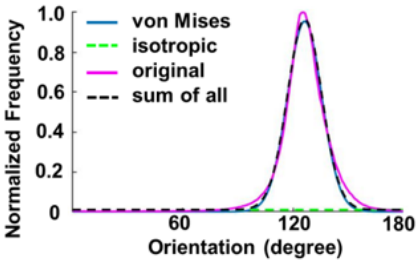

Appendix Figure 5. Curve fitting results of Section #1 nasal side posterior equator region.

	a	*k*	μ(rad)	*c*
von Mises-1	0.292	5.319	0.768	-
von Mises-2	0.589	1.315	0.307	-
von Mises-3	0.472	0.150	2.358	-
isotropic	-	-	-	0

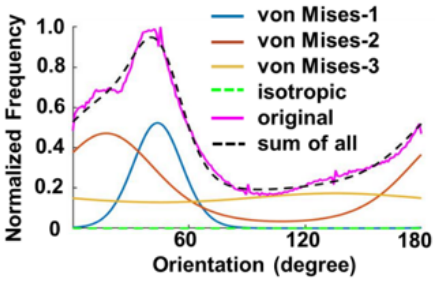

Appendix Figure 6. Curve fitting results of Section #1 temporal side posterior equator region.

	a	*k*	μ(rad)	*c*
von Mises	0.382	10.522	1.506	-
isotropic	-	-	-	0.028

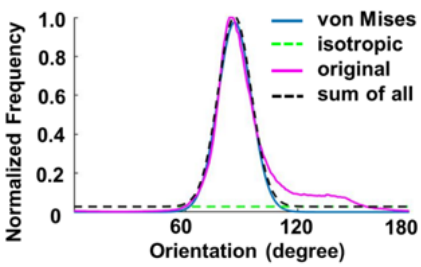

Appendix Figure 7. Curve fitting results of Section #1 nasal side equator region.

	a	*k*	μ(rad)	*c*
von Mises-1	0.112	19.258	1.288	-
von Mises-2	0.123	0.644	2.261	-
von Mises-3	0.450	3.080	1.373	-
isotropic	-	-	-	0

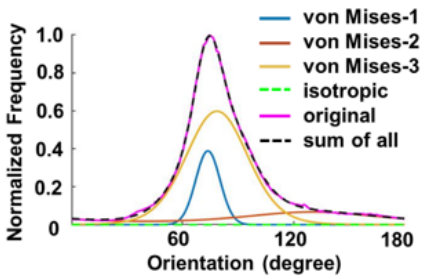

Appendix Figure 8. Curve fitting results of Section #1 temporal side equator region.

	a	*k*	μ(rad)	*c*
von Mises-1	0.153	26.925	1.211	-
von Mises-2	0.177	6.855	1.263	-
isotropic	-	-	-	0.022

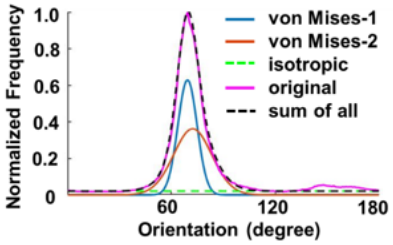

Appendix Figure 9. Curve fitting results of Section #1 nasal side anterior equator region.

	a	*k*	μ(rad)	*c*
von Mises-1	0.218	13.078	1.986	-
von Mises-2	0.365	2.322	2.091	-
isotropic	-	-	-	0.015

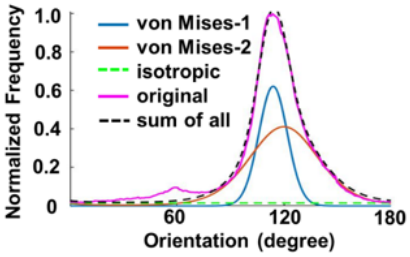

Appendix Figure 10. Curve fitting results of Section #1 temporal side anterior equator region.

	a	*k*	μ(rad)	*c*
von Mises-1	0.475	6.194	0.800	-
von Mises-2	0.173	4.841	0.314	-
isotropic	-	-	-	0

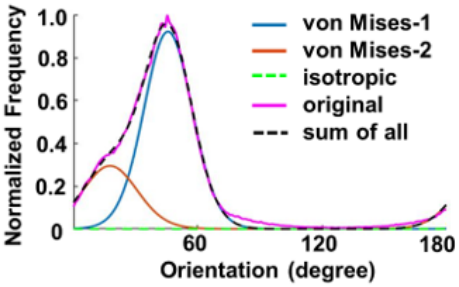

Appendix Figure 11. Curve fitting results of Section #1 nasal side limbus region.

	a	*k*	μ(rad)	*c*
von Mises-1	0.434	6.894	2.332	-
von Mises-2	0.136	1.366	2.609	-
isotropic	-	-	-	0.002

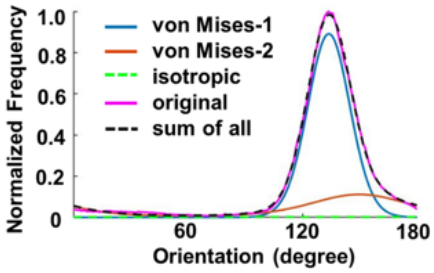

Appendix Figure 12. Curve fitting results of Section #1 temporal side limbus region.

	a	*k*	μ(rad)	*c*
von Mises-1	0.158	18.361	0.089	-
von Mises-2	0.341	3.275	0.175	-
isotropic	-	-	-	0.013

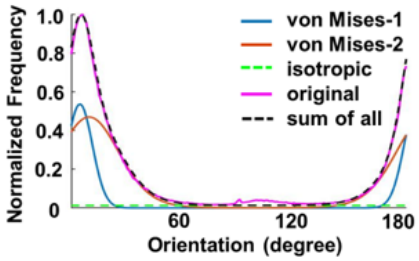

Appendix Figure 13. Curve fitting results of Section #1 nasal side peripheral cornea region.

	a	*k*	μ(rad)	*c*
von Mises-1	0.027	25.513	2.118	-
von Mises-2	0.194	12.511	2.432	-
von Mises-3	0.469	2.439	2.631	-
isotropic	-	-	-	0.002

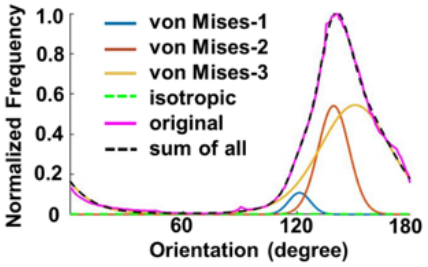

Appendix Figure 14. Curve fitting results of Section #1 temporal side peripheral cornea region.

	a	*k*	μ(rad)	*c*
von Mises-1	0.721	3.332	2.818	-
von Mises-2	0.048	1.598	2.294	
isotropic	-	-	-	0

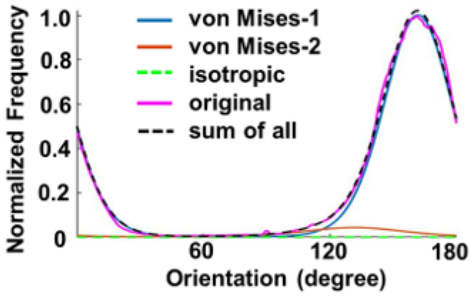

Appendix Figure 15. Curve fitting results of Section #1 central cornea region.

Appendix A.2 In-Depth Orientation Distribution Curve Fitting Results Of Section #2

	a	*k*	μ(rad)	*c*
von Mises-1	1.044	1.533	2.582	-
von Mises-2	0.203	2.564	0.772	-
von Mises-3	0.195	1.618	1.816	-
isotropic	-	-	-	0

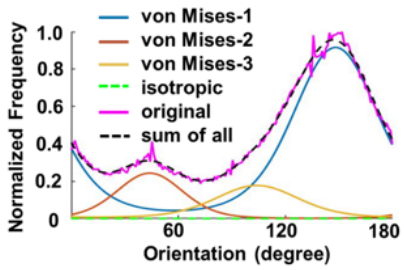

Appendix Figure 16. Curve fitting results of Section #2 nasal side PPS region.

	a	*k*	μ(rad)	*c*
von Mises-1	0.237	8.047	2.980	-
von Mises-2	0.890	0.869	1.812	-
von Mises-3	0.316	1.999	2.851	-
isotropic	-	-	-	0.004

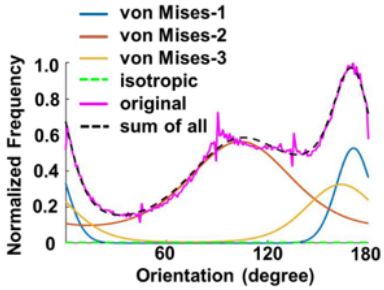

Appendix Figure 17. Curve fitting results of Section #2 temporal side PPS region.

	a	*k*	μ(rad)	*c*
von Mises-1	0.122	16.037	2.651	-
von Mises-2	0.089	0.504	0.284	-
von Mises-3	0.390	3.968	2.575	-
isotropic	-	-	-	0

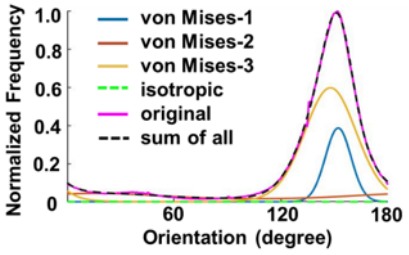

Appendix Figure 18. Curve fitting results of Section #2 nasal side posterior sclera region.

	a	*k*	μ(rad)	*c*
von Mises	0.763	3.006	3.021	-
isotropic	-	-	-	0.086

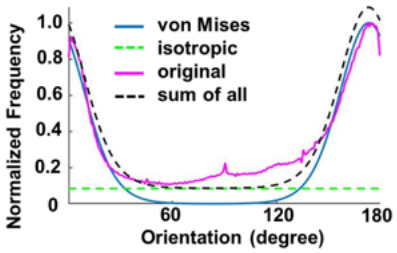

Appendix Figure 19. Curve fitting results of Section #2 temporal side posterior sclera region.

	a	*k*	μ(rad)	*c*
von Mises	0.470	7.145	2.255	-
isotropic	-	-	-	0.013

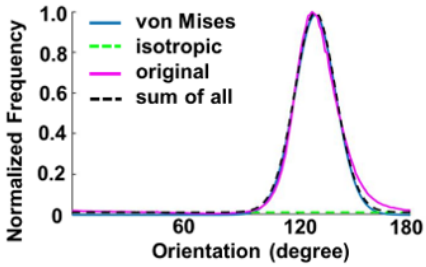

Appendix Figure 20. Curve fitting results of Section #2 nasal side posterior equator region.

	a	*k*	μ(rad)	*c*
von Mises	1.175	0.781	0.614	-
isotropic	-	-	-	0.005

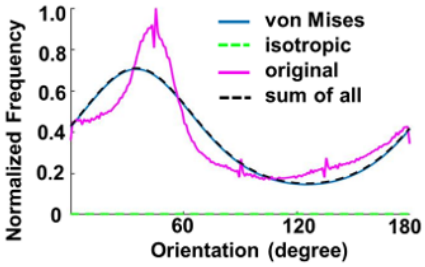

Appendix Figure 21. Curve fitting results of Section #2 temporal side posterior equator region.

	a	*k*	μ(rad)	*c*
von Mises-1	0.143	18.819	1.806	-
von Mises-2	0.435	2.225	1.794	-
isotropic	-	-	-	0.008

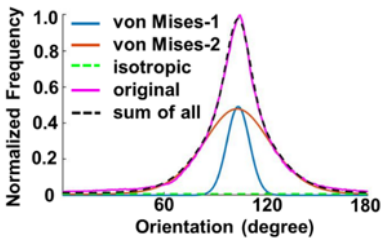

Appendix Figure 22. Curve fitting results of Section #2 nasal side equator region.

	a	*k*	μ(rad)	*c*
von Mises-1	0.356	10.263	1.172	-
von Mises-2	0.153	1.213	1.389	-
isotropic	-	-	-	0.002

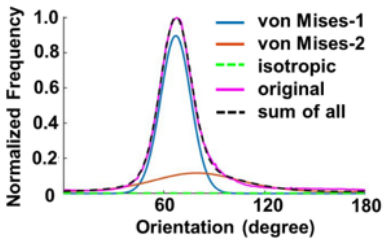

Appendix Figure 23. Curve fitting results of Section #2 temporal side equator region.

	a	*k*	μ(rad)	*c*
von Mises-1	0.323	8.425	1.027	-
von Mises-2	0.440	0.720	1.160	-
isotropic	-	-	-	0

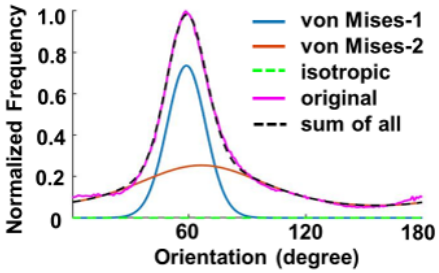

Appendix Figure 24. Curve fitting results of Section #2 nasal side anterior equator region.

	a	*k*	μ(rad)	*c*
von Mises-1	0.165	16.645	1.979	-
von Mises-2	0.321	3.772	2.078	-
isotropic	-	-	-	0.004

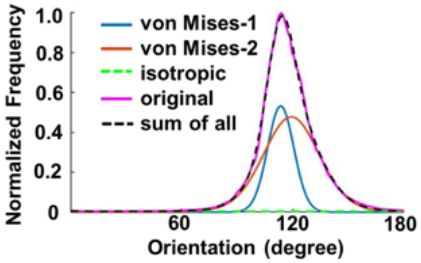

Appendix Figure 25. Curve fitting results of Section #2 temporal side anterior equator region.

	a	*k*	μ(rad)	*c*
von Mises-1	0.301	7.686	0.882	-
von Mises-2	0.604	0.734	0.671	-
isotropic	-	-	-	0

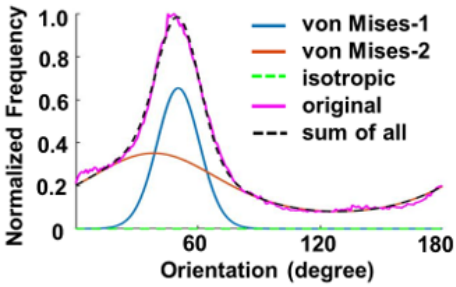

Appendix Figure 26Curve fitting results of Section #2 nasal side limbus region.

	a	*k*	μ(rad)	*c*
von Mises-1	0.332	9.222	2.279	-
von Mises-2	0.179	2.284	2.427	-
isotropic	-	-	-	0.002

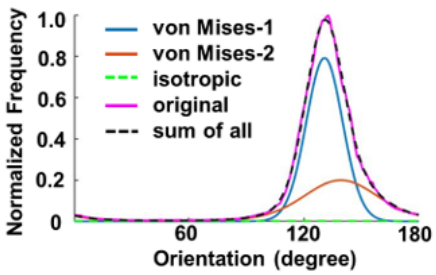

Appendix Figure 27. Curve fitting results of Section #2 temporal side limbus region.

	a	*k*	μ(rad)	*c*
von Mises-1	0.062	3.538	1.324	-
von Mises-2	0.410	4.941	0.716	-
von Mises-3	0.919	1.036	3.127	-
isotropic	-	-	-	0

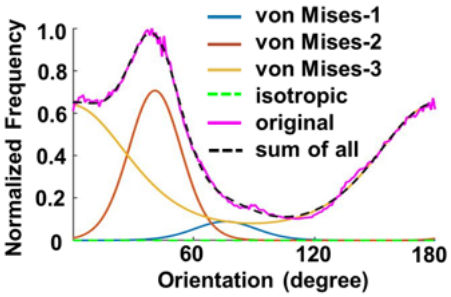

Appendix Figure 28. Curve fitting results of Section #2 nasal side peripheral cornea region.

	a	*k*	μ(rad)	*c*
von Mises-1	0.360	8.633	2.605	-
von Mises-2	0.171	1.818	2.536	-
isotropic	-	-	-	0

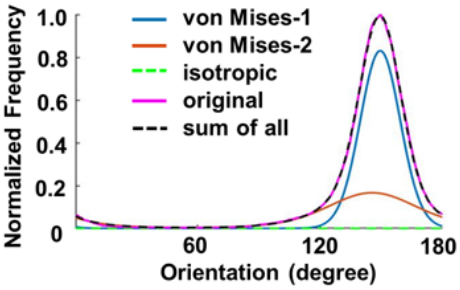

Appendix Figure 29. Curve fitting results of Section #2 temporal side peripheral cornea region.

	a	*k*	μ(rad)	*c*
von Mises-1	0.488	4.882	3.096	-
von Mises-2	0.383	1.777	2.541	-
isotropic	-	-	-	0

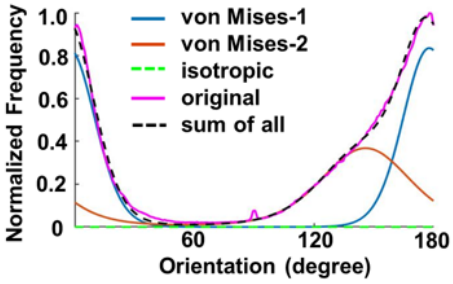

Appendix Figure 30. Curve fitting results of Section #2 central cornea region.

Appendix A.3 In-Depth Orientation Distribution Curve Fitting Results Of Section #3

	a	*k*	μ(rad)	*c*
von Mises-1	0.774	2.431	2.512	-
von Mises-2	0.191	3.135	1.567	-
isotropic	-	-	-	0.003

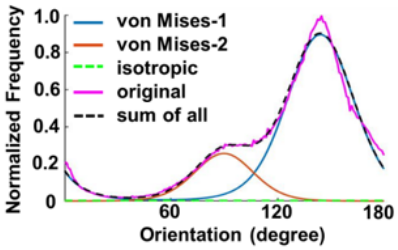

Appendix Figure 31. Curve fitting results of Section #3 nasal side PPS region.

	a	*k*	μ(rad)	*c*
von Mises-1	0.323	8.901	2.976	-
von Mises-2	0.435	0.631	2.593	-
isotropic	-	-	-	0.003

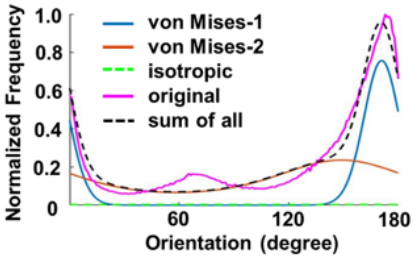

Appendix Figure 32. Curve fitting results of Section #3 temporal side PPS region.

	a	*k*	μ(rad)	*c*
von Mises-1	0.503	5.213	2.594	-
von Mises-2	0.122	1.658	2.367	-
isotropic	-	-	-	0

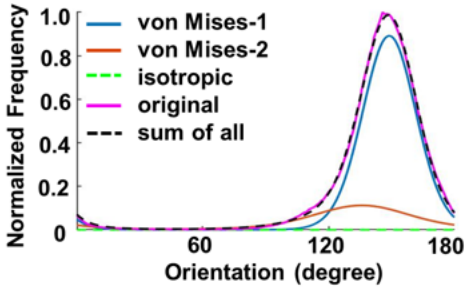

Appendix Figure 33. Curve fitting results of Section #3 nasal side posterior sclera region.

	a	*k*	μ(rad)	*c*
von Mises-1	0.325	6.533	0.140	-
von Mises-2	0.773	0.545	2.985	-
isotropic	-	-	-	0

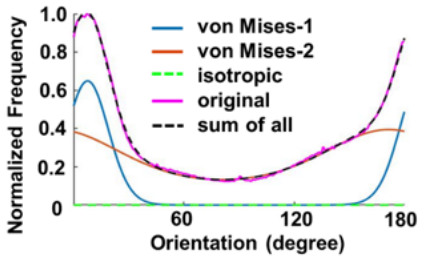

Appendix Figure 34. Curve fitting results of Section #3 temporal side posterior sclera region.

	a	*k*	μ(rad)	*c*
von Mises-1	0.214	10.517	2.085	-
von Mises-2	0.332	3.333	2.172	-
isotropic	-	-	-	0

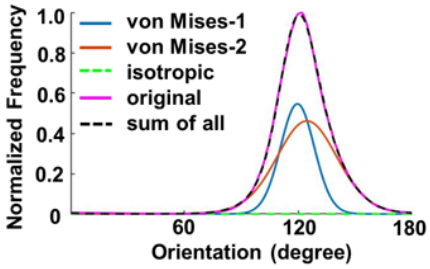

Appendix Figure 35. Curve fitting results of Section #3 nasal side posterior equator region.

	a	*k*	μ(rad)	*c*
von Mises-1	0.395	5.237	0.823	-
von Mises-2	0.832	0.458	0.059	-
isotropic	-	-	-	0

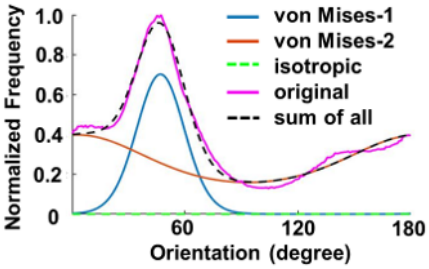

Appendix Figure 36. Curve fitting results of Section #3 temporal side posterior equator region.

	a	*k*	μ(rad)	*c*
von Mises-1	0.362	10.819	1.572	-
von Mises-2	0.075	6.204	1.959	-
isotropic	-	-	-	0.012

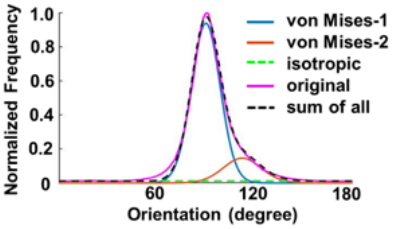

Appendix Figure 37. Curve fitting results of Section #3 nasal side equator region.

	a	*k*	μ(rad)	*c*
von Mises-1	0.299	1.008	1.581	-
von Mises-2	0.356	8.413	1.301	-
isotropic	-	-	-	0

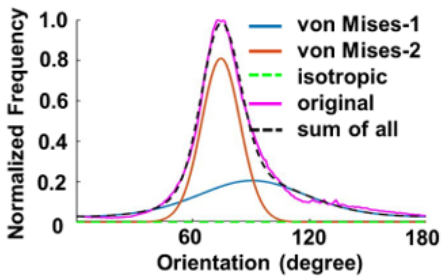

Appendix Figure 38. Curve fitting results of Section #3 temporal side equator region.

	a	*k*	μ(rad)	*c*
von Mises-1	0.340	8.781	1.073	-
von Mises-2	0.275	0.730	1.130	-
isotropic	-	-	-	0

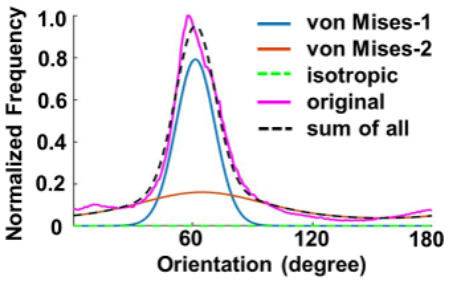

Appendix Figure 39. Curve fitting results of Section #3 nasal side anterior equator region.

	a	*k*	μ(rad)	*c*
von Mises-1	0.211	13.548	1.834	-
von Mises-2	0.416	1.541	1.931	-
isotropic	-	-	-	0.002

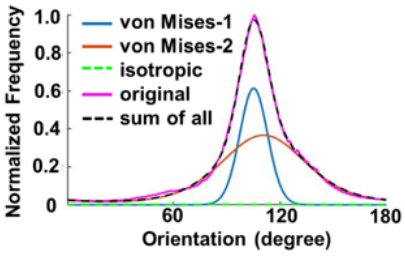

Appendix Figure 40. Curve fitting results of Section #3 temporal side anterior equator region.

	a	*k*	μ(rad)	*c*
von Mises-1	0.803	2.514	0.775	-
von Mises-2	0.185	12.064	0.168	-
isotropic	-	-	-	0.005

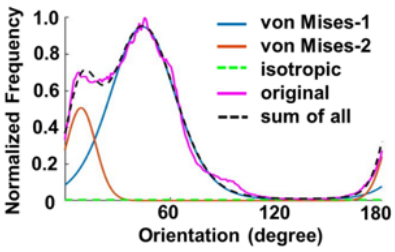

Appendix Figure 41. Curve fitting results of Section #3 nasal side limbus region.

	a	*k*	μ(rad)	*c*
von Mises	0.347	12.525	2.314	-
isotropic	-	-	-	0.013

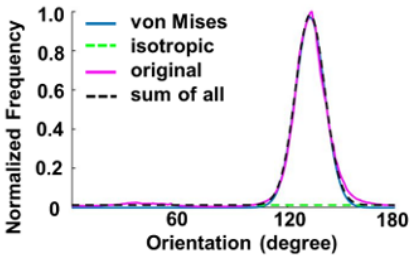

Appendix Figure 42. Curve fitting results of Section #3 temporal side limbus region.

	a	*k*	μ(rad)	*c*
von Mises-1	0.297	9.376	0.104	-
von Mises-2	0.562	1.137	0.492	-
von Mises-3	0.078	6.478	1.705	-
isotropic	-	-	-	0.001

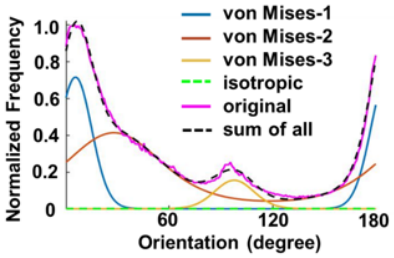

Appendix Figure 43. Curve fitting results of Section #3 nasal side peripheral cornea region.

	a	*k*	μ(rad)	*c*
von Mises-1	0.321	8.093	2.539	-
von Mises-2	0.340	1.415	2.587	-
isotropic	-	-	-	0.001

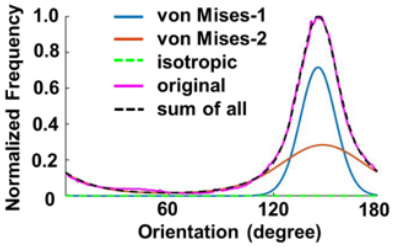

Appendix Figure 44. Curve fitting results of Section #3 temporal side peripheral cornea region.

	a	*k*	μ(rad)	*c*
von Mises-1	0.516	3.727	2.945	-
von Mises-2	0.414	0.672	2.757	-
isotropic	-	-	-	0

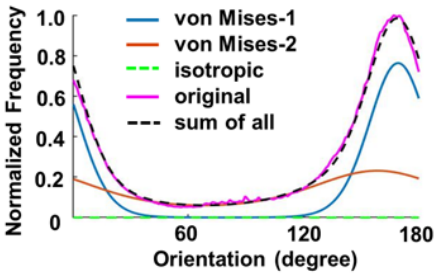

Appendix Figure 45. Curve fitting results of Section #3 central cornea region.

Appendix A.4 In-Depth Orientation Distribution Curve Fitting Results Of Section #4

	a	*k*	μ(rad)	*c*
von Mises-1	0.288	1.169	1.601	-
von Mises-2	0.978	1.646	2.983	-
isotropic	-	-	-	0

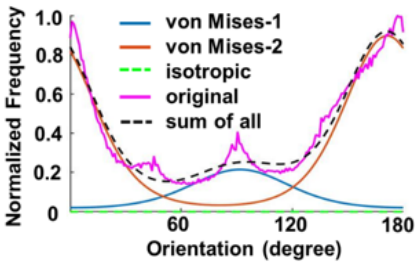

Appendix Figure 46. Curve fitting results of Section #4 nasal side PPS region.

	a	*k*	μ(rad)	*c*
von Mises-1	0.085	23.181	0.799	-
von Mises-2	1.447	0.467	0.434	-
isotropic	-	-	-	0

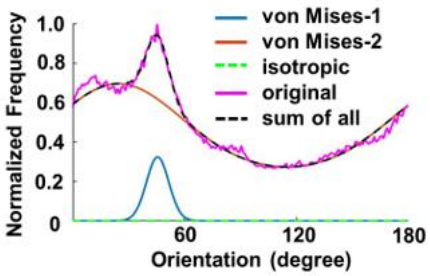

Appendix Figure 47. Curve fitting results of Section #4 temporal side PPS region.

	a	*k*	μ(rad)	*c*
von Mises-1	0.414	6.172	3.104	-
von Mises-2	0.310	0.613	0.079	-
isotropic	-	-	-	0

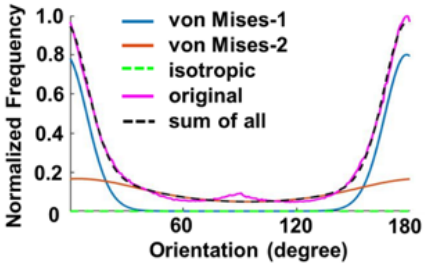

Appendix Figure 48. Curve fitting results of Section #4 nasal side posterior sclera region.

	a	*k*	μ(rad)	*c*
von Mises-1	0.375	4.188	0.667	-
von Mises-2	0.930	0.418	0.297	-
isotropic	-	-	-	0

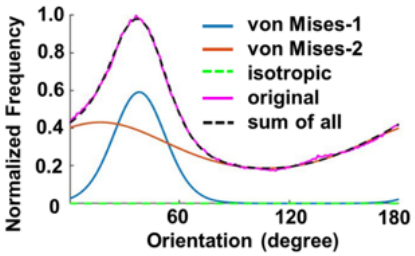

Appendix Figure 49. Curve fitting results of Section #4 temporal side posterior sclera region.

	a	*k*	μ(rad)	*c*
von Mises-1	0.520	4.800	2.775	-
von Mises-2	0.390	2.500	2.112	-
isotropic	-	-	-	0.03

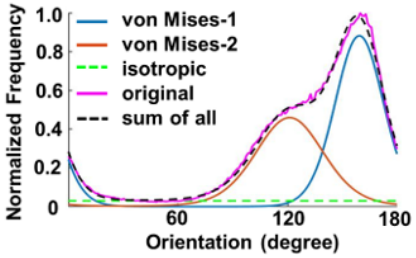

Appendix Figure 50. Curve fitting results of Section #4 nasal side posterior equator region.

	a	*k*	μ(rad)	*c*
von Mises-1	0.796	1.883	1.318	-
von Mises-2	0.672	0.743	2.029	-
isotropic	-	-	-	0

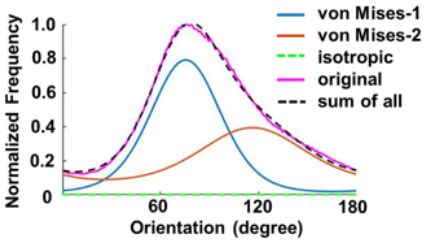

Appendix Figure 51. Curve fitting results of Section #4 temporal side posterior equator region.

	a	*k*	μ(rad)	*c*
von Mises	0.529	5.549	2.005	-
isotropic	-	-	-	0.010

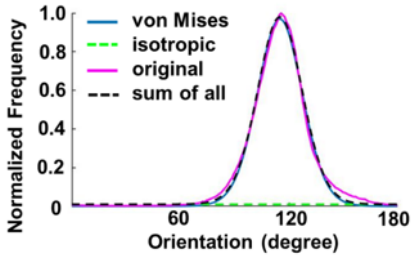

Appendix Figure 52. Curve fitting results of Section #4 nasal side equator region.

	a	*k*	μ(rad)	*c*
von Mises-1	0.657	2.737	2.107	-
von Mises-2	0.390	0.730	1.442	-
isotropic	-	-	-	0

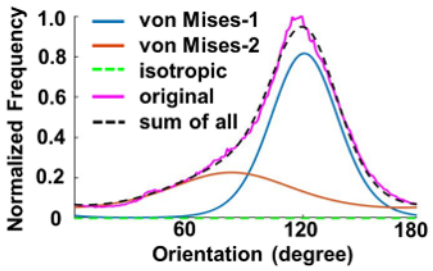

Appendix Figure 53. Curve fitting results of Section #4 temporal side equator region.

	a	*k*	μ(rad)	*c*
von Mises	0.334	13.967	1.712	-
isotropic	-	-	-	0.008

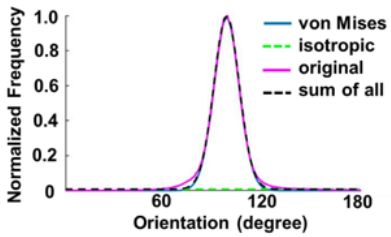

Appendix Figure 54. Curve fitting results of Section #4 nasal side anterior equator region.

	a	*k*	μ(rad)	*c*
von Mises-1	0.894	1.905	2.640	-
von Mises-2	0.419	0.870	0.704	-
isotropic	-	-	-	0

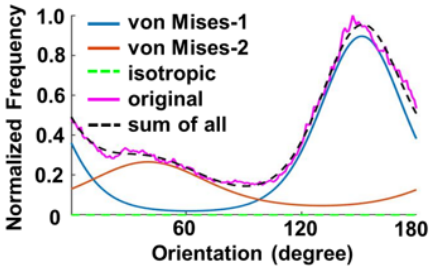

Appendix Figure 55. Curve fitting results of Section #4 temporal side anterior equator region.

	a	*k*	μ(rad)	*c*
von Mises	0.461	7.316	1.278	-
isotropic	-	-	-	0.005

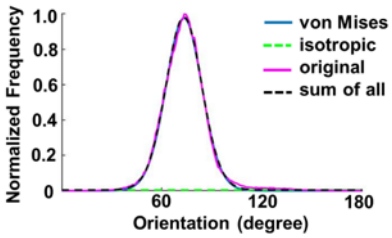

Appendix Figure 56. Curve fitting results of Section #4 nasal side limbus region.

	a	*k*	μ(rad)	*c*
von Mises-1	0.988	1.602	2.832	-
von Mises-2	0.591	1.558	0.530	-
isotropic	-	-	-	0

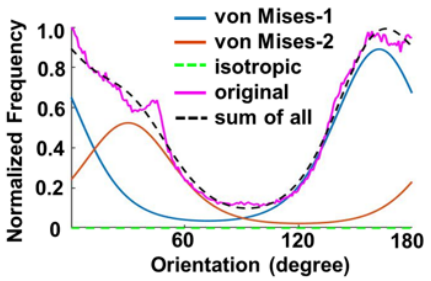

Appendix Figure 57. Curve fitting results of Section #4 temporal side limbus region.

	a	*k*	μ(rad)	*c*
von Mises	0.452	7.286	1.062	-
isotropic	-	-	-	0.014

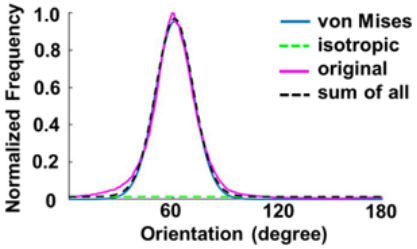

Appendix Figure 58. Curve fitting results of Section #4 nasal side peripheral cornea region.

	a	*k*	μ(rad)	*c*
von Mises-1	0.304	13.729	3.107	-
von Mises-2	0.130	1.045	3.090	-
isotropic	-	-	-	0.002

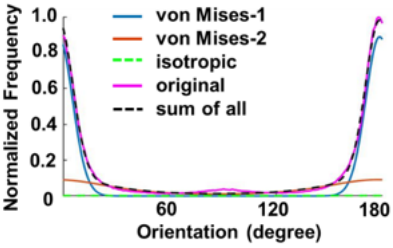

Appendix Figure 59. Curve fitting results of Section #4 temporal side peripheral cornea region.

	a	*k*	μ(rad)	*c*
von Mises-1	0.401	9.395	0.394	-
isotropic	-	-	-	0.012

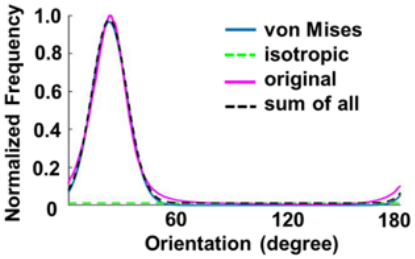

Appendix Figure 60. Curve fitting results of Section #4 central cornea region.

Appendix A.5 In-Depth Orientation Distribution Curve Fitting Results Of Section #5

	a	*k*	μ(rad)	*c*
von Mises-1	0.724	1.008	2.078	-
von Mises-2	0.547	3.788	3.128	-
von Mises-3	0.274	4.124	0.633	-
isotropic	-	-	-	0

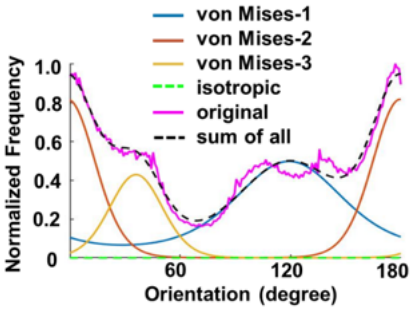

Appendix Figure 61. Curve fitting results of Section #5 nasal side PPS region.

	a	*k*	μ(rad)	*c*
von Mises-1	0.231	15.271	0.048	-
von Mises-2	0.546	0.880	0.452	-
isotropic	-	-	-	0.007

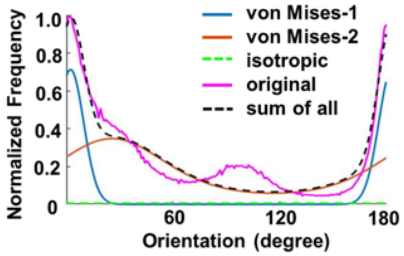

Appendix Figure 62. Curve fitting results of Section #5 temporal side PPS region.

	a	*k*	μ(rad)	*c*
von Mises-1	0.731	1.438	0.249	-
von Mises-2	0.154	9.109	3.085	-
von Mises-3	0.489	2.493	2.521	-
isotropic	-	-	-	0.001

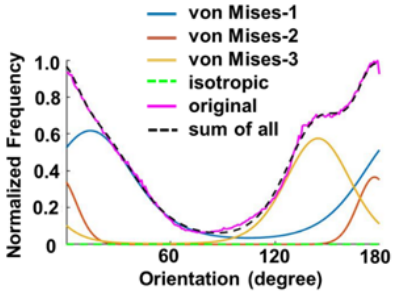

Appendix Figure 63. Curve fitting results of Section #5 nasal side posterior sclera region.

	a	*k*	μ(rad)	*c*
von Mises-1	0.665	2.944	0.244	-
von Mises-2	0.319	0.236	0.730	-
isotropic	-	-	-	0

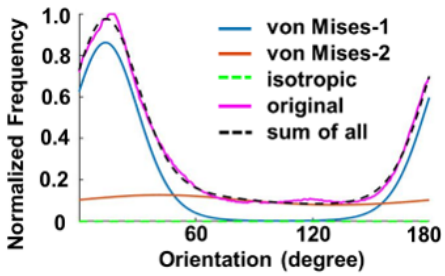

Appendix Figure 64. Curve fitting results of Section #5 temporal side posterior sclera region.

	a	*k*	μ(rad)	*c*
von Mises-1	0.114	22.165	2.269	-
von Mises-2	0.245	0.140	3.094	-
von Mises-3	0.328	4.127	2.200	-
isotropic	-	-	-	0

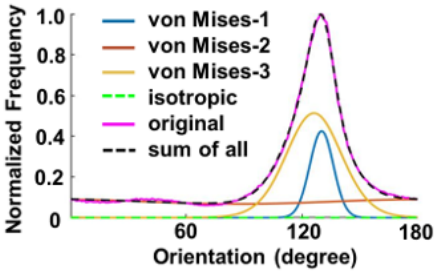

Appendix Figure 65. Curve fitting results of Section #5 nasal side posterior equator region.

	a	*k*	μ(rad)	*c*
von Mises-1	1.131	1.372	1.021	-
von Mises-2	0.177	6.713	1.682	-
isotropic	-	-	-	0.007

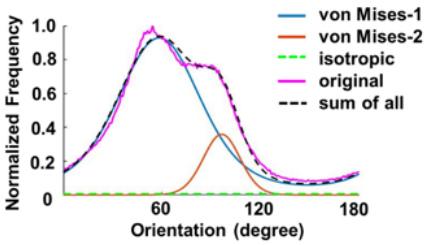

Appendix Figure 66. Curve fitting results of Section #5 temporal side posterior equator region.

	a	*k*	μ(rad)	*c*
von Mises	0.393	10.105	1.834	-
isotropic	-	-	-	0.014

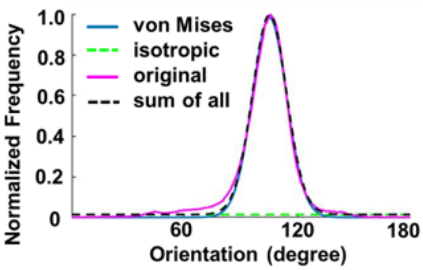

Appendix Figure 67. Curve fitting results of Section #5 nasal side equator region.

	a	*k*	μ(rad)	*c*
von Mises-1	0.231	13.605	1.784	-
von Mises-2	0.263	2.496	1.734	-
isotropic	-	-	-	0.003

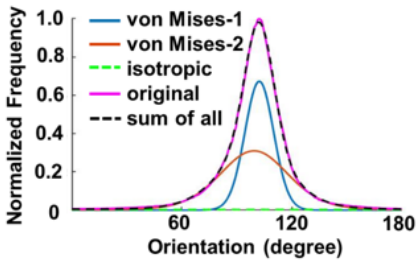

Appendix Figure 68. Curve fitting results of Section #5 temporal side equator region.

	a	*k*	μ(rad)	*c*
von Mises-1	0.564	2.769	1.420	-
von Mises-2	0.079	31.212	1.563	-
isotropic	-	-	-	0.009

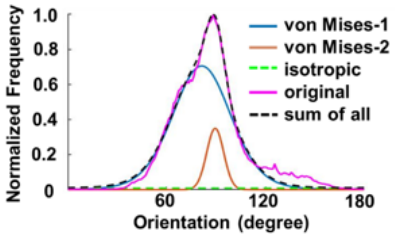

Appendix Figure 69. Curve fitting results of Section #5 nasal side anterior equator region.

	a	*k*	μ(rad)	*c*
von Mises-1	0.322	12.044	2.101	-
von Mises-2	0.172	0.835	2.231	-
isotropic	-	-	-	0

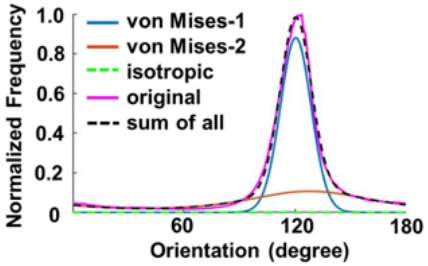

Appendix Figure 70. Curve fitting results of Section #5 temporal side anterior equator region.

	a	*k*	μ(rad)	*c*
von Mises-1	0.372	8.904	0.918	-
von Mises-2	0.221	0.192	0.961	-
isotropic	-	-	-	0

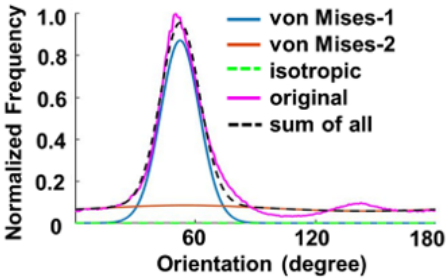

Appendix Figure 71. Curve fitting results of Section #5 nasal side limbus region.

	a	*k*	μ(rad)	*c*
von Mises	0.963	1.472	2.587	-
isotropic	-	-	-	0.013

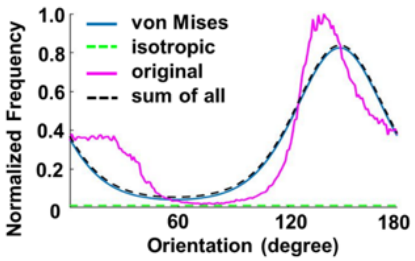

Appendix Figure 72. Curve fitting results of Section #5 temporal side limbus region.

	a	*k*	μ(rad)	*c*
von Mises-1	0.258	11.498	0.750	-
von Mises-2	0.418	1.899	0.441	-
isotropic	-	-	-	0.002

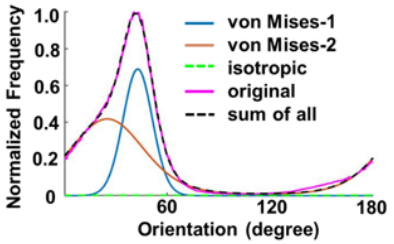

Appendix Figure 73. Curve fitting results of Section #5 nasal side peripheral cornea region.

	a	*k*	μ(rad)	*c*
von Mises-1	0.532	4.376	2.688	-
von Mises-2	0.738	2.473	0.209	-
isotropic	-	-	-	0

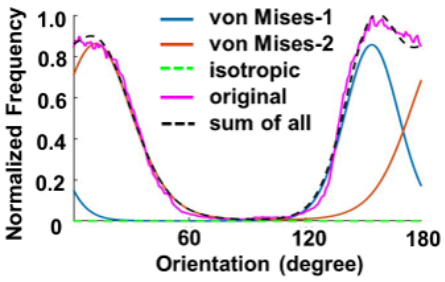

Appendix Figure 74. Curve fitting results of Section #5 temporal side peripheral cornea region.

	a	*k*	μ(rad)	*c*
von Mises	0.935	2.143	0.161	-
isotropic	-	-	-	0

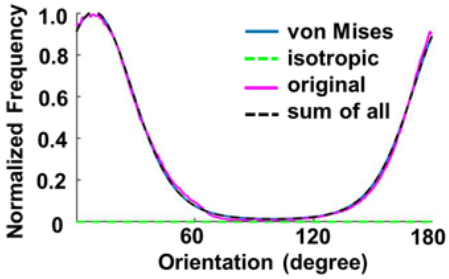

Appendix Figure 75. Curve fitting results of Section #5 central cornea region.

Appendix A.6 In-Depth Orientation Distribution Curve Fitting Results Of Section #6

	a	*k*	μ(rad)	*c*
von Mises-1	0.246	10.361	0.018	-
von Mises-2	0.749	1.069	0.501	-
isotropic	-	-	-	0.001

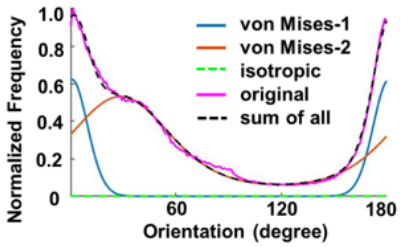

Appendix Figure 76. Curve fitting results of Section #6 nasal side PPS region.

	a	*k*	μ(rad)	*c*
von Mises-1	0.198	17.603	0.111	-
von Mises-2	0.151	0.840	1.782	-
von Mises-3	0.353	2.870	0.360	-
isotropic	-	-	-	0

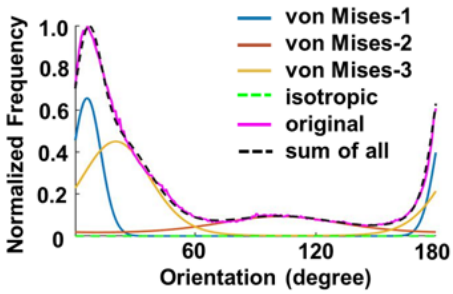

Appendix Figure 77. Curve fitting results of Section #6 temporal side PPS region.

	a	*k*	μ(rad)	*c*
von Mises-1	0.181	6.984	0.871	-
von Mises-2	1.041	0.984	0.565	-
von Mises-3	0.102	9.026	0.081	-
isotropic	-	-	-	0

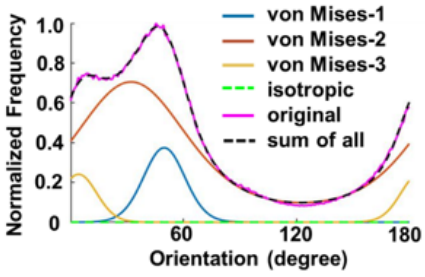

Appendix Figure 78. Curve fitting results of Section #6 nasal side posterior sclera region.

	a	*k*	μ(rad)	*c*
von Mises-1	0.319	6.448	3.058	-
von Mises-2	0.271	1.906	2.626	-
von Mises-3	0.336	1.814	0.280	-
isotropic	-	-	-	0

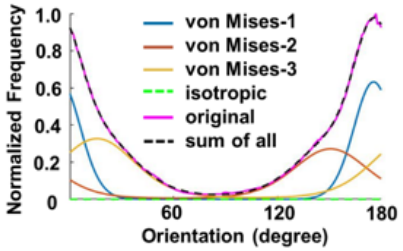

Appendix Figure 79. Curve fitting results of Section #6 temporal side posterior sclera region.

	a	*k*	μ(rad)	*c*
von Mises-1	0.472	4.582	1.193	-
von Mises-2	0.343	0.839	1.372	-
isotropic	-	-	-	0.001

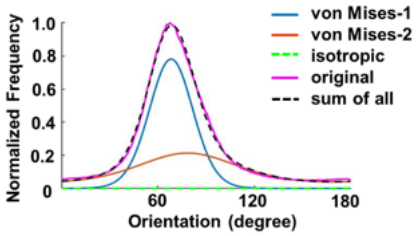

Appendix Figure 79. Curve fitting results of Section #6 nasal side posterior equator region.

	a	*k*	μ(rad)	*c*
von Mises-1	0.522	5.054	2.263	-
von Mises-2	0.158	0.598	2.655	-
isotropic	-	-	-	0

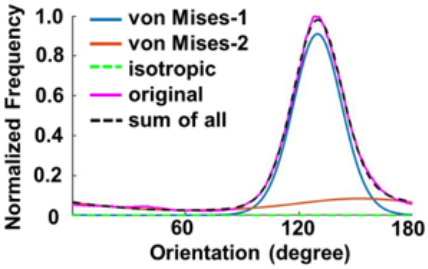

Appendix Figure 80. Curve fitting results of Section #6 temporal side posterior equator region.

	a	*k*	μ(rad)	*c*
von Mises-1	0.209	15.346	1.779	-
von Mises-2	0.239	3.586	1.760	-
isotropic	-	-	-	0.002

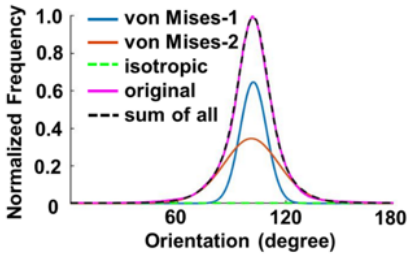

Appendix Figure 81. Curve fitting results of Section #6 nasal side equator region.

	a	*k*	μ(rad)	*c*
von Mises	0.236	26.013	1.842	-
isotropic	-	-	-	0.011

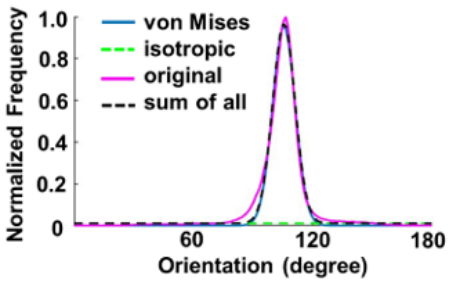

Appendix Figure 82. Curve fitting results of Section #6 temporal side equator region.

	a	*k*	μ(rad)	*c*
von Mises-1	0.112	17.839	2.330	-
von Mises-2	0.399	4.033	2.311	-
isotropic	-	-	-	0.012

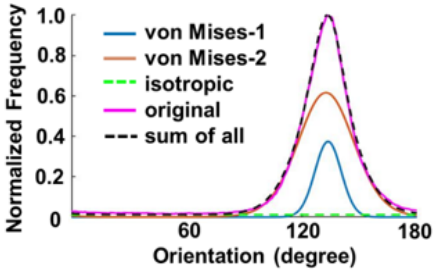

Appendix Figure 83. Curve fitting results of Section #6 nasal side anterior equator region.

	a	*k*	μ(rad)	*c*
von Mises-1	0.348	12.223	1.269	-
von Mises-2	0.113	0.812	2.197	-
isotropic	-	-	-	0

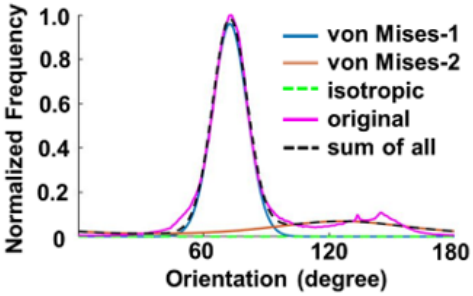

Appendix Figure 84. Curve fitting results of Section #6 temporal side anterior equator region.

Appendix A.7 In-Depth Orientation Distribution Curve Fitting Results Of Section #7

	a	*k*	μ(rad)	*c*
von Mises	0.806	2.464	0.457	-
isotropic	-	-	-	0.042

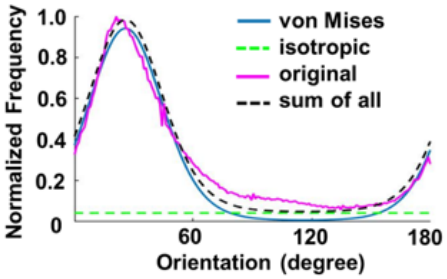

Appendix Figure 85. Curve fitting results of Section #7 nasal side PPS region.

	a	*k*	μ(rad)	*c*
von Mises-1	0.534	1.017	0.432	-
von Mises-2	0.274	7.616	0.414	-
von Mises-3	0.109	3.178	2.462	-
isotropic	-	-	-	0.001

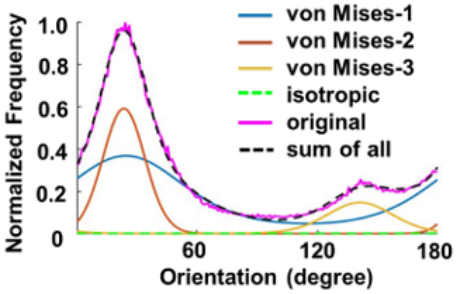

Appendix Figure 86. Curve fitting results of Section #7 temporal side PPS region.

	a	*k*	μ(rad)	*c*
von Mises	1.103	1.545	0.579	-
isotropic	-	-	-	0.012

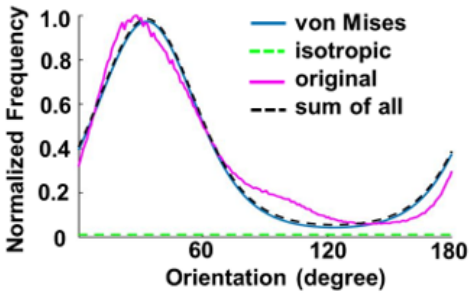

Appendix Figure 87. Curve fitting results of Section #7 nasal side posterior sclera region.

	a	*k*	μ(rad)	*c*
von Mises-1	0.326	5.484	0.155	-
von Mises-2	0.673	1.053	2.976	-
isotropic	-	-	-	0

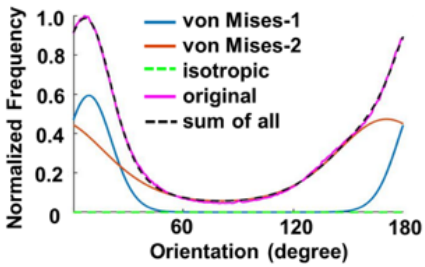

Appendix Figure 88. Curve fitting results of Section #7 temporal side posterior sclera region.

	a	*k*	μ(rad)	*c*
von Mises-1	0.917	1.986	1.298	-
von Mises-2	0.052	5.738	0.286	-
isotropic	-	-	-	0.008

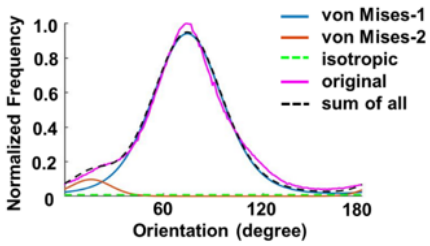

Appendix Figure 89. Curve fitting results of Section #7 nasal side posterior equator region.

	a	*k*	μ(rad)	*c*
von Mises-1	0.895	1.958	2.472	-
von Mises-2	0.258	0.846	1.840	-
isotropic	-	-	-	0

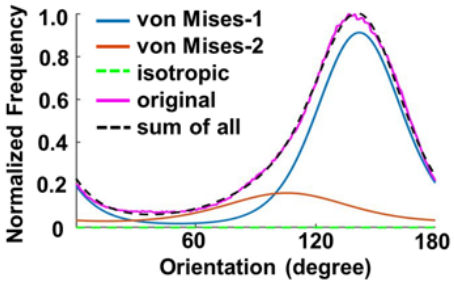

Appendix Figure 90. Curve fitting results of Section #7 temporal side posterior equator region.

	a	*k*	μ(rad)	*c*
von Mises-1	0.477	6.116	1.870	-
von Mises-2	0.119	1.030	1.725	-
isotropic	-	-	-	0

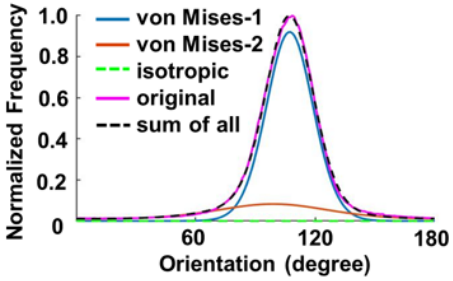

Appendix Figure 91. Curve fitting results of Section #7 nasal side equator region.

	a	*k*	μ(rad)	*c*
von Mises-1	0.137	26.481	1.893	-
von Mises-2	0.251	5.328	1.845	-
isotropic	-	-	-	0.01

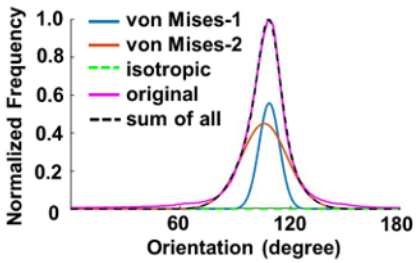

Appendix Figure 92. Curve fitting results of Section #7 temporal side equator region.

	a	*k*	μ(rad)	*c*
von Mises-1	0.454	4.815	2.368	-
von Mises-2	0.371	0.807	2.338	-
isotropic	-	-	-	0

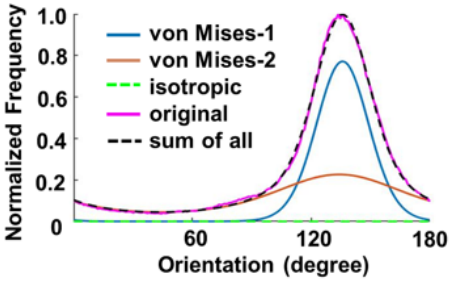

Appendix Figure 93. Curve fitting results of Section #7 nasal side anterior equator region.

	a	*k*	μ(rad)	*c*
von Mises-1	0.397	6.354	1.214	-
von Mises-2	0.292	1.082	1.397	-
isotropic	-	-	-	0

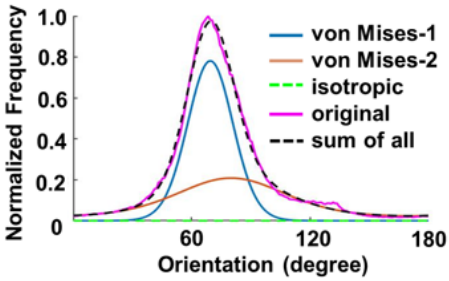

Appendix Figure 94. Curve fitting results of Section #7 temporal side anterior equator region.

Bibliography

Abahussin, M., S. Hayes, N. E. K. Cartwright, C. S. Kamma-Lorger, Y. Khan, J. Marshall and K. M. Meek (2009). "3D collagen orientation study of the human cornea using X-ray diffraction and femtosecond laser technology." Investigative ophthalmology & visual science **50**(11): 5159-5164.

Abass, A., S. Hayes, N. White, T. Sorensen and K. M. Meek (2015). "Transverse depth-dependent changes in corneal collagen lamellar orientation and distribution." Journal of The Royal Society Interface **12**(104): 20140717.

Akima, H. (1970). "A new method of interpolation and smooth curve fitting based on local procedures." Journal of the ACM (JACM) **17**(4): 589-602.

Akima, H. (1974). "A method of bivariate interpolation and smooth surface fitting based on local procedures." Communications of the ACM **17**(1): 18-20.

Arciniegas, A. and L. E. Amaya (1986). "Mechanical behavior of the sclera." Ophthalmologica **193**(1-2): 45-55.

Baillargeon, B., N. Rebelo, D. Fox, R. Taylor and E. Kuhl (2014). "The Living Heart Project: A robust and integrative simulator for human heart function." European Journal of Mechanics - A/Solids **48**.

Behkam, R., H. G. Kollech, A. Jana, A. Hill, F. Danford, S. Howerton, S. Ram, J. J. Rodríguez, U. Utzinger, C. A. Girkin and J. P. Vande Geest (2019). "Racioethnic differences in the biomechanical response of the lamina cribrosa." Acta Biomater **88**: 131-140.

Bell, J. S., S. Hayes, C. Whitford, J. Sanchez-Weatherby, O. Shebanova, C. Vergari, C. P. Winlove, N. Terrill, T. Sorensen, A. Elsheikh and K. M. Meek (2018). "The hierarchical response of human corneal collagen to load." Acta Biomater **65**: 216-225.

Boote, C., S. Dennis, R. H. Newton, H. Puri and K. M. Meek (2003). "Collagen Fibrils Appear More Closely Packed in the Prepupillary Cornea: Optical and Biomechanical Implications." Investigative Ophthalmology & Visual Science **44**(7): 2941-2948.

Boote, C., S. Hayes, M. Abahussin and K. M. Meek (2006). "Mapping Collagen Organization in the Human Cornea: Left and Right Eyes Are Structurally Distinct." Investigative Ophthalmology & Visual Science **47**(3): 901-908.

Boote, C., I. A. Sigal, R. Grytz, Y. Hua, T. D. Nguyen and M. J. Girard (2020). "Scleral structure and biomechanics." Progress in retinal and eye research **74**: 100773.

Brown, D. J., N. Morishige, A. Neekhra, D. S. Minckler and J. V. Jester (2007). "Application of second harmonic imaging microscopy to assess structural changes in optic nerve head structure ex vivo." Journal of biomedical optics **12**(2): 024029.

Burgoyne, C. (2015). "The morphological difference between glaucoma and other optic neuropathies." J Neuroophthalmol **35 Suppl 1**(0 1): S8-s21.

Burgoyne, C. F. (2015). "The non-human primate experimental glaucoma model." Exp Eye Res **141**: 57-73.

Burgoyne, C. F., J. C. Downs, A. J. Bellezza, J. K. Suh and R. T. Hart (2005). "The optic nerve head as a biomechanical structure: a new paradigm for understanding the role of IOP-related stress and strain in the pathophysiology of glaucomatous optic nerve head damage." Prog Retin Eye Res **24**(1): 39-73.

Campbell, I. C., B. Coudrillier, J. Mensah, R. L. Abel and C. R. Ethier (2015). "Automated segmentation of the lamina cribrosa using Frangi's filter: A novel approach for rapid identification of tissue volume fraction and beam orientation in a trabeculated structure in the eye." Journal of The Royal Society Interface **12**(104): 20141009.

Campbell, I. C., B. Coudrillier and C. Ross Ethier (2014). "Biomechanics of the posterior eye: a critical role in health and disease." Journal of biomechanical engineering **136**(2): 021005.

Candia, O. A., R. M. Gerometta and J. Danias (2014). "Tissue plasminogen activator reduces the elevated intraocular pressure induced by prednisolone in sheep." Experimental eye research **128**: 114-116.

Chang, Y., H. Li, S. Huang, J. He, S. Yang and Q. Wang (2015). The Application of FFT Analysis on the Feeder Current Based on the Smooth Function in MATLAB. 2015 Asia-Pacific Energy Equipment Engineering Research Conference, Atlantis Press.

Coudrillier, B., C. Boote, H. A. Quigley and T. D. Nguyen (2013). "Scleral anisotropy and its effects on the mechanical response of the optic nerve head." Biomechanics and Modeling in Mechanobiology **12**(5): 941-963.

Coudrillier, B., I. C. Campbell, A. T. Read, D. M. Geraldes, N. T. Vo, A. Feola, J. Mulvihill, J. Albon, R. L. Abel and C. R. Ethier (2016). "Effects of Peripapillary Scleral Stiffening on the Deformation of the Lamina Cribrosa." Invest Ophthalmol Vis Sci **57**(6): 2666-2677.

Coudrillier, B., D. M. Geraldes, N. T. Vo, R. Atwood, C. Reinhard, I. C. Campbell, Y. Raji, J. Albon, R. L. Abel and C. R. Ethier (2016). "Phase-Contrast Micro-Computed Tomography Measurements of the Intraocular Pressure-Induced Deformation of the Porcine Lamina Cribrosa." IEEE transactions on medical imaging **35**(4): 988-999.

Coudrillier, B., J. K. Pijanka, J. L. Jefferys, A. Goel, H. A. Quigley, C. Boote and T. D. Nguyen (2015). "Glaucoma-related changes in the mechanical properties and collagen micro-architecture of the human sclera." PloS one **10**(7): e0131396.

Coudrillier, B., J. K. Pijanka, J. L. Jefferys, T. Sorensen, H. A. Quigley, C. Boote and T. D. Nguyen (2015). "Collagen structure and mechanical properties of the human sclera: analysis for the effects of age." Journal of biomechanical engineering **137**(4): 041006.

Coudrillier, B., J. Tian, S. Alexander, K. M. Myers, H. A. Quigley and T. D. Nguyen (2012). "Biomechanics of the human posterior sclera: age-and glaucoma-related changes measured using inflation testing." Investigative Ophthalmology & Visual Science **53**(4): 1714-1728.

Danford, F. L., D. Yan, R. A. Dreier, T. M. Cahir, C. A. Girkin and J. P. Vande Geest (2013). "Differences in the region- and depth-dependent microstructural organization in normal versus glaucomatous human posterior sclerae." Investigative ophthalmology & visual science **54**(13): 7922-7932.

Downs, J. C. (2015). "Optic nerve head biomechanics in aging and disease." Experimental eye research **133**: 19-29.

Downs, J. C. and C. A. Girkin (2017). "Lamina cribrosa in glaucoma." Current opinion in ophthalmology **28**(2): 113.

Downs, J. C., M. D. Roberts and C. F. Burgoyne (2008). "The mechanical environment of the optic nerve head in glaucoma." Optometry and vision science: official publication of the American Academy of Optometry **85**(6): 425.

Downs, J. C., M. D. Roberts and I. A. Sigal (2011). "Glaucomatous cupping of the lamina cribrosa: a review of the evidence for active progressive remodeling as a mechanism." Experimental eye research **93**(2): 133-140.

Eilaghi, A., J. G. Flanagan, I. Tertinegg, C. A. Simmons, G. W. Brodland and C. R. Ethier (2010). "Biaxial mechanical testing of human sclera." Journal of Biomechanics **43**(9): 1696-1701.

El‐Maghraby, H. M., T. G. Nyland and R. W. Bellhorn (1995). "Ultrasonographic and biometric evaluation of sheep and cattle eyes." Veterinary Radiology & Ultrasound **36**(2): 148-151.

Elliott, D. M. and L. A. Setton (2001). "Anisotropic and inhomogeneous tensile behavior of the human anulus fibrosus: experimental measurement and material model predictions." Journal of biomechanical engineering **123**(3): 256-263.

Ethier, C. R., M. Johnson and J. Ruberti (2004). "Ocular biomechanics and biotransport." Annu. Rev. Biomed. Eng. **6**: 249-273.

Feola, A. J., J. G. Myers, J. Raykin, L. Mulugeta, E. S. Nelson, B. C. Samuels and C. R. Ethier (2016). "Finite Element Modeling of Factors Influencing Optic Nerve Head Deformation Due to Intracranial Pressure." Investigative Ophthalmology & Visual Science **57**(4): 1901-1911.

Flammer, J., S. Orgül, V. P. Costa, N. Orzalesi, G. K. Krieglstein, L. M. Serra, J.-P. Renard and E. Stefánsson (2002). "The impact of ocular blood flow in glaucoma." Progress in retinal and eye research **21**(4): 359-393.

Fung, Y.-c. (2013). Biomechanics: mechanical properties of living tissues, Springer Science & Business Media.

Gałecki, A. and T. Burzykowski (2013). Linear mixed-effects model. Linear mixed-effects models using R, Springer**:** 245-273.

Gerometta, R., M.-G. Spiga, T. Borrás and O. A. Candia (2010). "Treatment of sheep steroid–induced ocular hypertension with a glucocorticoid-inducible MMP1 gene therapy virus." Investigative ophthalmology & visual science **51**(6): 3042-3048.

Girard, M. J., J.-K. F. Suh, M. Bottlang, C. F. Burgoyne and J. C. Downs (2011). "Biomechanical changes in the sclera of monkey eyes exposed to chronic IOP elevations." Investigative ophthalmology & visual science **52**(8): 5656-5669.

Girard, M. J., T. A. Tun, R. Husain, S. Acharyya, B. A. Haaland, X. Wei, J. M. Mari, S. A. Perera, M. Baskaran and T. Aung (2015). "Lamina cribrosa visibility using optical coherence tomography: comparison of devices and effects of image enhancement techniques." Investigative ophthalmology & visual science **56**(2): 865-874.

Girard, M. J. A., A. Dahlmann-Noor, S. Rayapureddi, J. A. Bechara, B. M. E. Bertin, H. Jones, J. Albon, P. T. Khaw and C. R. Ethier (2011). "Quantitative mapping of scleral fiber orientation in normal rat eyes." Investigative ophthalmology & visual science **52**(13): 9684-9693.

Girard, M. J. A., J. C. Downs, M. Bottlang, C. F. Burgoyne and J.-K. F. Suh (2009). "Peripapillary and Posterior Scleral Mechanics—Part II: Experimental and Inverse Finite Element Characterization." Journal of Biomechanical Engineering **131**(5).

Girard, M. J. A., J. C. Downs, C. F. Burgoyne and J.-K. F. Suh (2009). "Peripapillary and posterior scleral mechanics—part I: development of an anisotropic hyperelastic constitutive model." Journal of biomechanical engineering **131**(5).

Girard, M. J. A., J.-K. F. Suh, M. Bottlang, C. F. Burgoyne and J. C. Downs (2009). "Scleral Biomechanics in the Aging Monkey Eye." Investigative Ophthalmology & Visual Science **50**(11): 5226-5237.

Gogola, A., N.-J. Jan, B. L. Brazile, P. Lam, K. L. Lathrop, K. C. Chan and I. A. Sigal (2018). "Spatial patterns and age-related changes of the collagen crimp in the human cornea and sclera." Investigative Ophthalmology & Visual Science **59**(7): 2987-2998.

Gogola, A., N.-J. Jan, K. L. Lathrop and I. A. Sigal (2018). "Radial and circumferential collagen fibers are a feature of the peripapillary sclera of human, monkey, pig, cow, goat, and sheep." Investigative ophthalmology & visual science **59**(12): 4763-4774.

Gouget, C. L., M. J. Girard and C. R. Ethier (2012). "A constrained von Mises distribution to describe fiber organization in thin soft tissues." Biomechanics and modeling in mechanobiology **11**(3): 475-482.

Grytz, R., M. A. Fazio, M. J. A. Girard, V. Libertiaux, L. Bruno, S. Gardiner, C. A. Girkin and J. C. Downs (2014). "Material properties of the posterior human sclera." Journal of the mechanical behavior of biomedical materials **29**: 602-617.

Grytz, R., M. A. Fazio, V. Libertiaux, L. Bruno, S. Gardiner, C. A. Girkin and J. C. Downs (2014). "Age-and race-related differences in human scleral material properties." Investigative Ophthalmology & Visual Science **55**(12): 8163-8172.

Grytz, R., C. A. Girkin, V. Libertiaux and J. C. Downs (2012). "Perspectives on biomechanical growth and remodeling mechanisms in glaucoma()." Mech Res Commun **42**: 92-106.

Grytz, R., K. Krishnan, R. Whitley, V. Libertiaux, I. A. Sigal, C. A. Girkin and J. C. Downs (2020). "A Mesh-Free Approach to Incorporate Complex Anisotropic and Heterogeneous Material Properties into Eye-Specific Finite Element Models." Comput Methods Appl Mech Eng **358**.

Grytz, R. and G. Meschke (2009). "Constitutive modeling of crimped collagen fibrils in soft tissues." Journal of the Mechanical Behavior of Biomedical Materials **2**(5): 522-533.

Grytz, R. and G. Meschke (2010). "A computational remodeling approach to predict the physiological architecture of the collagen fibril network in corneo-scleral shells." Biomech Model Mechanobiol **9**(2): 225-235.

Grytz, R., G. Meschke and J. B. Jonas (2011). "The collagen fibril architecture in the lamina cribrosa and peripapillary sclera predicted by a computational remodeling approach." Biomechanics and modeling in mechanobiology **10**(3): 371-382.

Grytz, R., I. A. Sigal, J. W. Ruberti, G. Meschke and J. Crawford Downs (2012). "Lamina cribrosa thickening in early glaucoma predicted by a microstructure motivated growth and remodeling approach." Mechanics of Materials **44**: 99-109.

Grytz, R., H. Yang, Y. Hua, B. C. Samuels and I. A. Sigal (2020). "Connective tissue remodeling in myopia and its potential role in increasing risk of glaucoma." Current Opinion in Biomedical Engineering **15**: 40-50.

Guerin, H. L. and D. M. Elliott (2007). "Quantifying the contributions of structure to annulus fibrosus mechanical function using a nonlinear, anisotropic, hyperelastic model." Journal of Orthopaedic Research **25**(4): 508-516.

Hadi, M. F. and V. H. Barocas (2013). "Microscale Fiber Network Alignment Affects Macroscale Failure Behavior in Simulated Collagen Tissue Analogs." Journal of Biomechanical Engineering **135**(2).

Hatami-Marbini, H. and M. Pachenari (2020). "The contribution of sGAGs to stress-controlled tensile response of posterior porcine sclera." PLoS One **15**(2): e0227856.

Hayes, S., S. Khan, C. Boote, C. S. Kamma-Lorger, E. Dooley, J. Lewis, N. Hawksworth, T. Sorensen, S. Daya and K. M. Meek (2012). "Depth profile study of abnormal collagen orientation in keratoconus corneas." Archives of Ophthalmology **130**(2): 251-252.

Hernandez, M. R. (2000). "The optic nerve head in glaucoma: role of astrocytes in tissue remodeling." Prog Retin Eye Res **19**(3): 297-321.

Hoerig, C., S. McFadden, Q. V. Hoang and J. Mamou (2022). "Biomechanical changes in myopic sclera correlate with underlying changes in microstructure." Experimental Eye Research: 109165.

Holzapfel, G. A. (2001). "Biomechanics of soft tissue." The handbook of materials behavior models **3**: 1049-1063.

Hua, Y., M. Quinn, F. Ji, S. Salinas, R. Amini and I. A. Sigal (2022). "Mechanical anisotropy of the equatorial sclera does not concur with its preferred fiber orientation." Investigative Ophthalmology & Visual Science **63**(7): 2731 – A0095-2731 – A0095.

Hua, Y., A. P. Voorhees, N.-J. Jan, B. Wang, S. Waxman, J. S. Schuman and I. A. Sigal (2020). "Role of radially aligned scleral collagen fibers in optic nerve head biomechanics." Experimental Eye Research **199**: 108188.

Huang, W., Q. Fan, W. Wang, M. Zhou, A. M. Laties and X. Zhang (2013). "Collagen: a potential factor involved in the pathogenesis of glaucoma." Med Sci Monit Basic Res **19**: 237-240.

Huang, X., Q. Zhou, J. Liu, Y. Zhao, W. Zhou and D. Deng (2017). "3D stochastic modeling, simulation and analysis of effective thermal conductivity in fibrous media." Powder technology **320**: 397-404.

Islam, M. R., F. Ji, M. Bansal, Y. Hua and I. A. Sigal (2023). "Fibrous Finite Element Modeling of the Optic Nerve Head Region." bioRxiv: 2023.2005. 2026.542465.

Islam, M. R. and R. C. Picu (2018). "Effect of Network Architecture on the Mechanical Behavior of Random Fiber Networks." Journal of Applied Mechanics **85**(8).

Jan, N.-J., B. L. Brazile, D. Hu, G. Grube, J. Wallace, A. Gogola and I. A. Sigal (2018). "Crimp around the globe; patterns of collagen crimp across the corneoscleral shell." Experimental Eye Research **172**: 159-170.

Jan, N.-J., C. Gomez, S. Moed, A. P. Voorhees, J. S. Schuman, R. A. Bilonick and I. A. Sigal (2017). "Microstructural crimp of the lamina cribrosa and peripapillary sclera collagen fibers." Investigative ophthalmology & visual science **58**(9): 3378-3388.

Jan, N.-J., J. L. Grimm, H. Tran, K. L. Lathrop, G. Wollstein, R. A. Bilonick, H. Ishikawa, L. Kagemann, J. S. Schuman and I. A. Sigal (2015). "Polarization microscopy for characterizing fiber orientation of ocular tissues." Biomedical Optics Express **6**(12): 4705-4718.

Jan, N.-J., K. Lathrop and I. A. Sigal (2017). "Collagen architecture of the posterior pole: high-resolution wide field of view visualization and analysis using polarized light microscopy." Investigative ophthalmology & visual science **58**(2): 735-744.

Jan, N.-J., P.-Y. Lee, J. Wallace, M. Iasella, A. Gogola and I. A. Sigal (2022). "Stretch-Induced Uncrimping of Equatorial Sclera Collagen Bundles." bioRxiv: 2022.2009.2013.507860.

Jan, N.-J. and I. A. Sigal (2018). "Collagen fiber recruitment: a microstructural basis for the nonlinear response of the posterior pole of the eye to increases in intraocular pressure." Acta biomaterialia **72**: 295-305.

Ji, F., M. Bansal, B. Wang, Y. Hua, M. R. Islam, F. Matuschke, M. Axer and I. A. Sigal (2023). "A direct fiber approach to model sclera collagen architecture and biomechanics." Experimental Eye Research **232**: 109510.

Ji, F., M. Quinn, Y. Hua, P.-Y. Lee and I. A. Sigal (2023). "2D or not 2D? Mapping the in-depth inclination of the collagen fibers of the corneoscleral shell." Experimental Eye Research: 109701.

Ji, F., B. Yang, Y. Hua, P.-Y. Lee, Z. Zhu and I. A. Sigal (2020). "Characterization of lamina cribrosa beam insertion into the sclera canal in sheep, pig, monkey, and human." Investigative Ophthalmology & Visual Science **61**(7): 4782-4782.

Jonas, J. B., E. Berenshtein and L. Holbach (2004). "Lamina cribrosa thickness and spatial relationships between intraocular space and cerebrospinal fluid space in highly myopic eyes." Investigative ophthalmology & visual science **45**(8): 2660-2665.

Jonas, J. B. and W. M. Budde (2000). "Diagnosis and pathogenesis of glaucomatous optic neuropathy: morphological aspects1." Progress in retinal and eye research **19**(1): 1-40.

Jonas, J. B., S. B. Jonas, R. A. Jonas, L. Holbach and S. Panda-Jonas (2011). "Histology of the parapapillary region in high myopia." Am J Ophthalmol **152**(6): 1021-1029.

Kang, M. H. and D.-Y. Yu (2015). "Distribution pattern of axonal cytoskeleton proteins in the human optic nerve head." Neural regeneration research **10**(8): 1198.

Karimi, A., S. M. Rahmati, R. Razaghi, C. A. Girkin and J. C. Downs (2022). "Finite element modeling of the complex anisotropic mechanical behavior of the human sclera and pia mater." Computer Methods and Programs in Biomedicine **215**: 106618.

Kim, D. W., J. W. Jeoung, Y. W. Kim, M. J. A. Girard, J. M. Mari, Y. K. Kim, K. H. Park and D. M. Kim (2016). "Prelamina and Lamina Cribrosa in Glaucoma Patients With Unilateral Visual Field Loss." Investigative Ophthalmology & Visual Science **57**(4): 1662-1670.

Kim, Y., D. Kim, J. Jeoung, D. Kim and K. Park (2015). "Peripheral lamina cribrosa depth in primary open-angle glaucoma: a swept-source optical coherence tomography study of lamina cribrosa." Eye **29**(10): 1368-1374.

Kim, Y. W., J. W. Jeoung, M. J. Girard, J. M. Mari and K. H. Park (2016). "Positional and curvature difference of lamina cribrosa according to the baseline intraocular pressure in primary open-angle glaucoma: a swept-source optical coherence tomography (SS-OCT) study." PLoS One **11**(9): e0162182.

Kim, Y. W., J. W. Jeoung, D. W. Kim, M. J. Girard, J. M. Mari, K. H. Park and D. M. Kim (2016). "Clinical assessment of lamina cribrosa curvature in eyes with primary open-angle glaucoma." PloS one **11**(3): e0150260.

Kimpton, L. S., B. J. Walker, C. L. Hall, B. Bintu, D. Crosby, H. M. Byrne and A. Goriely (2021). "A morphoelastic shell model of the eye." Journal of Elasticity **145**(1): 5-29.

Kiumehr, S., S. C. Park, S. Dorairaj, C. C. Teng, C. Tello, J. M. Liebmann and R. Ritch (2012). "In vivo evaluation of focal lamina cribrosa defects in glaucoma." Archives of ophthalmology **130**(5): 552-559.

Kollech, H. G., A. Ayyalasomayajula, R. Behkam, E. Tamimi, K. Furdella, M. Drewry and J. P. Vande Geest (2019). "A Subdomain Method for Mapping the Heterogeneous Mechanical Properties of the Human Posterior Sclera." Front Bioeng Biotechnol **7**: 129.

Komai, Y. and T. Ushiki (1991). "The three-dimensional organization of collagen fibrils in the human cornea and sclera." Investigative Ophthalmology & Visual Science **32**(8): 2244-2258.

Koudouna, E., M. Winkler, E. Mikula, T. Juhasz, D. J. Brown and J. V. Jester (2018). "Evolution of the vertebrate corneal stroma." Progress in Retinal and Eye Research **64**: 65-76.

Lagarias, J. C., J. A. Reeds, M. H. Wright and P. E. Wright (1998). "Convergence properties of the Nelder--Mead simplex method in low dimensions." SIAM Journal on optimization **9**(1): 112-147.

Lanir, Y. (2017). "Multi-scale Structural Modeling of Soft Tissues Mechanics and Mechanobiology." Journal of Elasticity **129**(1): 7-48.

Latour, G., I. Gusachenko, L. Kowalczuk, I. Lamarre and M. C. Schanne-Klein (2012). "In vivo structural imaging of the cornea by polarization-resolved second harmonic microscopy." Biomed Opt Express **3**(1): 1-15.

Lee, K. M., T.-W. Kim, R. N. Weinreb, E. J. Lee, M. J. Girard and J. M. Mari (2014). "Anterior lamina cribrosa insertion in primary open-angle glaucoma patients and healthy subjects." PLoS One **9**(12): e114935.

Lee, P.-Y., B. Yang, Y. Hua, S. Waxman, Z. Zhu, F. Ji and I. A. Sigal (2022). "Real-time imaging of optic nerve head collagen microstructure and biomechanics using instant polarized light microscopy." Experimental eye research **217**: 108967.

Lee, P.-Y., B. Yang and I. A. Sigal (2022). Quantitative stretch-induced collagen fiber recruitment and microarchitecture changes using instant polarized light microscopy. 15th World Congress on Computational Mechanics, Hybrid conference, presentation delivered remotely, in-person held in Yokohama Japan, July 31-August 5, 2022.

Licup, A. J., S. Münster, A. Sharma, M. Sheinman, L. M. Jawerth, B. Fabry, D. A. Weitz and F. C. MacKintosh (2015). "Stress controls the mechanics of collagen networks." Proceedings of the National Academy of Sciences **112**(31): 9573-9578.

Ling, Y. T. T., R. Shi, D. E. Midgett, J. L. Jefferys, H. A. Quigley and T. D. Nguyen (2019). "Characterizing the Collagen Network Structure and Pressure-Induced Strains of the Human Lamina Cribrosa." Invest Ophthalmol Vis Sci **60**(7): 2406-2422.

Lisboa, R., M. T. Leite, L. M. Zangwill, A. Tafreshi, R. N. Weinreb and F. A. Medeiros (2012). "Diagnosing preperimetric glaucoma with spectral domain optical coherence tomography." Ophthalmology **119**(11): 2261-2269.

Liu, B., S. McNally, J. I. Kilpatrick, S. P. Jarvis and C. J. O'Brien (2018). "Aging and ocular tissue stiffness in glaucoma." Survey of ophthalmology **63**(1): 56-74.

Masters, B. R. (1998). "Three-dimensional confocal microscopy of the human optic nerve in vivo." Optics express **3**(10): 356-359.

Matuschke, F., K. Amunts and M. Axer (2021). "fastPLI: A Fiber Architecture Simulation Toolbox for 3D-PLI." Journal of Open Source Software **6**(61): 3042.

Matuschke, F., K. Ginsburger, C. Poupon, K. Amunts and M. Axer (2019). "Dense fiber modeling for 3D-Polarized Light Imaging simulations." Advances in parallel computing **34**: 240 - 253.

Meek, K. M. and C. Knupp (2015). "Corneal structure and transparency." Prog Retin Eye Res **49**: 1-16.

Mikula, E., M. Winkler, T. Juhasz, D. J. Brown, G. Shoa, S. Tran, M. C. Kenney and J. V. Jester (2018). "Axial mechanical and structural characterization of keratoconus corneas." Experimental Eye Research **175**: 14-19.

Miles, J. (2005). "R ‐ squared, adjusted R ‐ squared." Encyclopedia of statistics in behavioral science.

Moerman, K. M. (2018). "GIBBON: the geometry and image-based bioengineering add-on." Journal of Open Source Software **3**(22): 506.

Morishige, N., A. J. Wahlert, M. C. Kenney, D. J. Brown, K. Kawamoto, T.-i. Chikama, T. Nishida and J. V. Jester (2007). "Second-harmonic imaging microscopy of normal human and keratoconus cornea." Investigative ophthalmology & visual science **48**(3): 1087-1094.

Murienne, B. J., M. L. Chen, H. A. Quigley and T. D. Nguyen (2016). "The contribution of glycosaminoglycans to the mechanical behaviour of the posterior human sclera." Journal of The Royal Society Interface **13**(119).

Nerurkar, N. L., R. L. Mauck and D. M. Elliott (2011). "Modeling interlamellar interactions in angle-ply biologic laminates for annulus fibrosus tissue engineering." Biomechanics and modeling in mechanobiology **10**(6): 973-984.

Newton, R. H. and K. M. Meek (1998). "Circumcorneal annulus of collagen fibrils in the human limbus." Invest Ophthalmol Vis Sci **39**(7): 1125-1134.

Norman, R. E., J. G. Flanagan, I. A. Sigal, S. M. K. Rausch, I. Tertinegg and C. R. Ethier (2011). "Finite element modeling of the human sclera: Influence on optic nerve head biomechanics and connections with glaucoma." Experimental Eye Research **93**(1): 4-12.

Oikawa, K., J. N. Ver Hoeve, L. B. Teixeira, K. C. Snyder, J. A. Kiland, N. M. Ellinwood and G. J. McLellan (2020). "Sub-region-specific optic nerve head glial activation in glaucoma." Molecular neurobiology **57**: 2620-2638.

Pellicer-Valero, O. J., M. J. Rupérez, S. Martínez-Sanchis and J. D. Martín-Guerrero (2020). "Real-time biomechanical modeling of the liver using Machine Learning models trained on Finite Element Method simulations." Expert Systems with Applications **143**: 113083.

Petsche, S. J., D. Chernyak, J. Martiz, M. E. Levenston and P. M. Pinsky (2012). "Depth-Dependent Transverse Shear Properties of the Human Corneal Stroma." Investigative Ophthalmology & Visual Science **53**(2): 873-880.

Petsche, S. J. and P. M. Pinsky (2013). "The role of 3-D collagen organization in stromal elasticity: a model based on X-ray diffraction data and second harmonic-generated images." Biomechanics and modeling in mechanobiology **12**(6): 1101-1113.

Picu, R. C., S. Deogekar and M. R. Islam (2018). "Poisson's Contraction and Fiber Kinematics in Tissue: Insight From Collagen Network Simulations." Journal of Biomechanical Engineering **140**(2).

Pijanka, J. K., A. Abass, T. Sorensen, A. Elsheikh and C. Boote (2013). "A wide-angle X-ray fibre diffraction method for quantifying collagen orientation across large tissue areas: application to the human eyeball coat." Journal of Applied Crystallography **46**(5): 1481-1489.

Pijanka, J. K., B. Coudrillier, K. Ziegler, T. Sorensen, K. M. Meek, T. D. Nguyen, H. A. Quigley and C. Boote (2012). "Quantitative Mapping of Collagen Fiber Orientation in Non-glaucoma and Glaucoma Posterior Human Sclerae." Investigative Ophthalmology & Visual Science **53**(9): 5258-5270.

Pijanka, J. K., P. P. Markov, D. Midgett, N. G. Paterson, N. White, E. J. Blain, T. D. Nguyen, H. A. Quigley and C. Boote (2019). "Quantification of collagen fiber structure using second harmonic generation imaging and two-dimensional discrete Fourier transform analysis: Application to the human optic nerve head." Journal of biophotonics **12**(5): e201800376.

Pijanka, J. K., M. T. Spang, T. Sorensen, J. Liu, T. D. Nguyen, H. A. Quigley and C. Boote (2015). "Depth-dependent changes in collagen organization in the human peripapillary sclera." PloS one **10**(2): e0118648.

Preibisch, S., S. Saalfeld and P. Tomancak (2009). "Globally optimal stitching of tiled 3D microscopic image acquisitions." Bioinformatics **25**(11): 1463-1465.

Quigley, H. A. (2005). "Glaucoma: macrocosm to microcosm the Friedenwald lecture." Invest Ophthalmol Vis Sci **46**(8): 2662-2670.

Quigley, H. A. and A. T. Broman (2006). "The number of people with glaucoma worldwide in 2010 and 2020." British journal of ophthalmology **90**(3): 262-267.

Quigley, H. A., R. W. Flower, E. M. Addicks and D. S. McLeod (1980). "The mechanism of optic nerve damage in experimental acute intraocular pressure elevation." Invest Ophthalmol Vis Sci **19**(5): 505-517.

Rasmussen, C. A. and P. L. Kaufman (2005). "Primate glaucoma models." J Glaucoma **14**(4): 311-314.

Roberts, M. D., Y. Liang, I. A. Sigal, J. L. Grimm, J. Reynaud, A. Bellezza, C. F. Burgoyne and J. C. Downs (2010). "Correlation between local stress and strain and lamina cribrosa connective tissue volume fraction in normal monkey eyes." Investigative ophthalmology & visual science **51**(1): 295-307.

Roberts, M. D., I. A. Sigal, Y. Liang, C. F. Burgoyne and J. C. Downs (2010). "Changes in the Biomechanical Response of the Optic Nerve Head in Early Experimental Glaucoma." Investigative Ophthalmology & Visual Science **51**(11): 5675-5684.

Saiman, M., M. Wahab and M. Wahit (2014). The effect of fabric weave on the tensile strength of woven kenaf reinforced unsaturated polyester composite. Proceedings of the International Colloquium in Textile Engineering, Fashion, Apparel and Design 2014 (ICTEFAD 2014), Springer.

Salinas, S. D., M. M. Clark and R. Amini (2020). "The effects of −80 °C short-term storage on the mechanical response of tricuspid valve leaflets." Journal of Biomechanics **98**: 109462.

Schindelin, J., I. Arganda-Carreras, E. Frise, V. Kaynig, M. Longair, T. Pietzsch, S. Preibisch, C. Rueden, S. Saalfeld and B. Schmid (2012). "Fiji: an open-source platform for biological-image analysis." Nature methods **9**(7): 676-682.

Schwaner, S. A., B. G. Hannon, A. J. Feola and C. R. Ethier (2020). "Biomechanical properties of the rat sclera obtained with inverse finite element modeling." Biomechanics and Modeling in Mechanobiology **19**(6): 2195-2212.

Schwaner, S. A., R. N. Perry, A. M. Kight, E. Winder, H. Yang, J. C. Morrison, C. F. Burgoyne and C. Ross Ethier (2020). "Individual-Specific Modeling of Rat Optic Nerve Head Biomechanics in Glaucoma." Journal of Biomechanical Engineering **143**(4).

Sigal, I. A. (2009). "Interactions between geometry and mechanical properties on the optic nerve head." Invest Ophthalmol Vis Sci **50**(6): 2785-2795.

Sigal, I. A. and C. R. Ethier (2009). "Biomechanics of the optic nerve head." Experimental eye research **88**(4): 799-807.

Sigal, I. A., J. G. Flanagan and C. R. Ethier (2005). "Factors influencing optic nerve head biomechanics." Investigative ophthalmology & visual science **46**(11): 4189-4199.

Sigal, I. A., J. G. Flanagan, K. L. Lathrop, I. Tertinegg and R. Bilonick (2012). "Human Lamina Cribrosa Insertion and Age." Investigative Ophthalmology & Visual Science **53**(11): 6870-6879.

Sigal, I. A., J. G. Flanagan, I. Tertinegg and C. R. Ethier (2004). "Finite element modeling of optic nerve head biomechanics." Investigative ophthalmology & visual science **45**(12): 4378-4387.

Sigal, I. A., J. G. Flanagan, I. Tertinegg and C. R. Ethier (2009). "Modeling individual-specific human optic nerve head biomechanics. Part I: IOP-induced deformations and influence of geometry." Biomechanics and modeling in mechanobiology **8**(2): 85-98.

Sigal, I. A., J. G. Flanagan, I. Tertinegg and C. R. Ethier (2010). "3D morphometry of the human optic nerve head." Experimental eye research **90**(1): 70-80.

Sigal, I. A., J. L. Grimm, N.-J. Jan, K. Reid, D. S. Minckler and D. J. Brown (2014). "Eye-specific IOP-induced displacements and deformations of human lamina cribrosa." Investigative Ophthalmology & Visual Science **55**(1): 1-15.

Sigal, I. A., B. Wang, N. G. Strouthidis, T. Akagi and M. J. Girard (2014). "Recent advances in OCT imaging of the lamina cribrosa." Br J Ophthalmol **98 Suppl 2**(Suppl 2): ii34-39.

Spoerl, E., A. G. Boehm and L. E. Pillunat (2005). "The influence of various substances on the biomechanical behavior of lamina cribrosa and peripapillary sclera." Investigative ophthalmology & visual science **46**(4): 1286-1290.

Stig, F. and S. Hallström (2019). "Effects of crimp and textile architecture on the stiffness and strength of composites with 3D reinforcement." Advances in Materials Science and Engineering **2019**.

Stowell, C., C. F. Burgoyne, E. R. Tamm and C. R. Ethier (2017). "Biomechanical aspects of axonal damage in glaucoma: A brief review." Exp Eye Res **157**: 13-19.

Strouthidis, N. G. and M. J. Girard (2013). "Altering the way the optic nerve head responds to intraocular pressure—a potential approach to glaucoma therapy." Current opinion in pharmacology **13**(1): 83-89.

Summers Rada, J. A., S. Shelton and T. T. Norton (2006). "The sclera and myopia." Experimental Eye Research **82**(2): 185-200.

Tamm, E. R. and C. R. Ethier (2017). "Biological aspects of axonal damage in glaucoma: A brief review." Exp Eye Res **157**: 5-12.

Tan, N. Y., V. Koh, M. J. Girard and C. Y. Cheng (2018). "Imaging of the lamina cribrosa and its role in glaucoma: a review." Clinical & experimental ophthalmology **46**(2): 177-188.

Thomas, V. S., V. Lai and R. Amini (2019). "A computational multi-scale approach to investigate mechanically-induced changes in tricuspid valve anterior leaflet microstructure." Acta Biomaterialia **94**: 524-535.

Tran, H., N.-J. Jan, D. Hu, A. Voorhees, J. S. Schuman, M. A. Smith, G. Wollstein and I. A. Sigal (2017). "Formalin fixation and cryosectioning cause only minimal changes in shape or size of ocular tissues." Scientific reports **7**(1): 1-11.

Tran, H., J. Wallace, A. P. Voorhees, Z. Zhu, B. Wang, K. A. Lucy, J. S. Schuman, M. Smith, G. Wollstein and I. A. Sigal (2017). "Lamina cribrosa shape is different between humans and monkeys at baseline IOP and is changed differently with IOP elevations." Investigative Ophthalmology & Visual Science **58**(8): 3157-3157.

Van Der Rijt, J. A., K. O. Van Der Werf, M. L. Bennink, P. J. Dijkstra and J. Feijen (2006). "Micromechanical testing of individual collagen fibrils." Macromolecular bioscience **6**(9): 697-702.

van Tonder, J. D., M. Venter and G. Venter (2023). "A Novel Method for Resolving Non-Unique Solutions Observed in Fitting Parameters to the Mooney Rivlin Material Model." Available at SSRN 4364489.

Vohnsen, B. and P. Artal (2008). "Second-harmonic microscopy of ex vivo porcine corneas." J Microsc **232**(1): 158-163.

Voorhees, A. P., L. C. Ho, N.-J. Jan, H. Tran, Y. van der Merwe, K. Chan and I. A. Sigal (2017). "Whole-globe biomechanics using high-field MRI." Experimental eye research **160**: 85-95.

Voorhees, A. P., N.-J. Jan, Y. Hua, B. Yang and I. A. Sigal (2018). "Peripapillary sclera architecture revisited: a tangential fiber model and its biomechanical implications." Acta Biomaterialia **79**: 113-122.

Voorhees, A. P., N.-J. Jan and I. A. Sigal (2017). "Effects of collagen microstructure and material properties on the deformation of the neural tissues of the lamina cribrosa." Acta biomaterialia **58**: 278-290.

Voorhees, A. P., N. J. Jan, M. E. Austin, J. G. Flanagan, J. M. Sivak, R. A. Bilonick and I. A. Sigal (2017). "Lamina Cribrosa Pore Shape and Size as Predictors of Neural Tissue Mechanical Insult." Investigative ophthalmology & visual science **58**(12): 5336-5346.

Wagner, D. R. and J. C. Lotz (2004). "Theoretical model and experimental results for the nonlinear elastic behavior of human annulus fibrosus." Journal of orthopaedic research **22**(4): 901-909.

Wang, B., Y. Hua, B. L. Brazile, B. Yang and I. A. Sigal (2020). "Collagen fiber interweaving is central to sclera stiffness." Acta Biomaterialia **113**: 429-437.

Wang, X., H. Rumpel, W. E. H. Lim, M. Baskaran, S. A. Perera, M. E. Nongpiur, T. Aung, D. Milea and M. J. A. Girard (2016). "Finite Element Analysis Predicts Large Optic Nerve Head Strains During Horizontal Eye Movements." Investigative Ophthalmology & Visual Science **57**(6): 2452-2462.

Watson, P. G. and R. D. Young (2004). "Scleral structure, organisation and disease. A review." Experimental eye research **78**(3): 609-623.

Weinreb, R. N., T. Aung and F. A. Medeiros (2014). "The pathophysiology and treatment of glaucoma: a review." Jama **311**(18): 1901-1911.

Wenger, M. P. E., L. Bozec, M. A. Horton and P. Mesquida (2007). "Mechanical properties of collagen fibrils." Biophysical Journal **93**(4): 1255-1263.

Whitford, C., A. Joda, S. Jones, F. Bao, P. Rama and A. Elsheikh (2016). "Ex vivo testing of intact eye globes under inflation conditions to determine regional variation of mechanical stiffness." Eye and vision **3**(1): 1-12.

Winkler, M., D. Chai, S. Kriling, C. J. Nien, D. J. Brown, B. Jester, T. Juhasz and J. V. Jester (2011). "Nonlinear optical macroscopic assessment of 3-D corneal collagen organization and axial biomechanics." Investigative ophthalmology & visual science **52**(12): 8818-8827.

Winkler, M., B. Jester, C. Nien-Shy, S. Massei, D. S. Minckler, J. V. Jester and D. J. Brown (2010). "High resolution three-dimensional reconstruction of the collagenous matrix of the human optic nerve head." Brain research bulletin **81**(2-3): 339-348.

Winkler, M., G. Shoa, Y. Xie, S. J. Petsche, P. M. Pinsky, T. Juhasz, D. J. Brown and J. V. Jester (2013). "Three-Dimensional Distribution of Transverse Collagen Fibers in the Anterior Human Corneal Stroma." Investigative Ophthalmology & Visual Science **54**(12): 7293-7301.

Yan, D., S. McPheeters, G. Johnson, U. Utzinger and J. P. V. Geest (2011). "Microstructural differences in the human posterior sclera as a function of age and race." Investigative ophthalmology & visual science **52**(2): 821-829.

Yang, B., B. Brazile, N.-J. Jan, Y. Hua, J. Wei and I. A. Sigal (2018). "Structured polarized light microscopy for collagen fiber structure and orientation quantification in thick ocular tissues." Journal of biomedical optics **23**(10): 106001.

Yang, B., N. J. Jan, B. Brazile, A. Voorhees, K. L. Lathrop and I. A. Sigal (2018). "Polarized light microscopy for 3-dimensional mapping of collagen fiber architecture in ocular tissues." Journal of biophotonics **11**(8): e201700356.

Yang, B., P. Y. Lee, Y. Hua, B. Brazile, S. Waxman, F. Ji, Z. Zhu and I. A. Sigal (2021). "Instant polarized light microscopy for imaging collagen microarchitecture and dynamics." Journal of biophotonics **14**(2): e202000326.

Yang, H., G. Williams, J. Downs, I. Sigal, M. Roberts, J. Grimm, H. Thompson and C. Burgoyne (2010). "Optic Nerve Head (ONH) Lamina Cribrosa Insertion Migration and Pialization in Early Non-Human Primate (NHP) Experimental Glaucoma." Investigative Ophthalmology & Visual Science **51**(13): 1631-1631.

Yang, H., G. Williams, J. C. Downs, I. A. Sigal, M. D. Roberts, H. Thompson and C. F. Burgoyne (2011). "Posterior (outward) migration of the lamina cribrosa and early cupping in monkey experimental glaucoma." Invest Ophthalmol Vis Sci **52**(10): 7109-7121.

Yang, L., K. O. Van Der Werf, B. F. Koopman, V. Subramaniam, M. L. Bennink, P. J. Dijkstra and J. Feijen (2007). "Micromechanical bending of single collagen fibrils using atomic force microscopy." Journal of Biomedical Materials Research Part A **82**(1): 160-168.

Zhang, L., J. Albon, H. Jones, C. L. Gouget, C. R. Ethier, J. C. Goh and M. J. Girard (2015). "Collagen microstructural factors influencing optic nerve head biomechanics." Investigative Ophthalmology & Visual Science **56**(3): 2031-2042.

Zhang, L., S. P. Lake, V. K. Lai, C. R. Picu, V. H. Barocas and M. S. Shephard (2013). "A coupled fiber-matrix model demonstrates highly inhomogeneous microstructural interactions in soft tissues under tensile load." Journal of biomechanical engineering **135**(1): 011008.

Zhou, D., A. Abass, A. Eliasy, H. P. Studer, A. Movchan, N. Movchan and A. Elsheikh (2019). "Microstructure-based numerical simulation of the mechanical behaviour of ocular tissue." Journal of the Royal Society Interface **16**(154): 20180685.